NIST-GCR-90-570

STRUCTURE AND RADIATION PROPERTIES OF TURBULENT DIFFUSION FLAMES

Y. R. Sivathanu
M. E. Kounalakis
G. M. Faeth

University of Michigan
Department of Aerospace Engineering
Ann Arbor, MI

Prepared for
U.S. DEPARTMENT OF COMMERCE
National Institute of Standards and Technology
National Engineering Laboratory
Center for Fire Research
Gaithersburg, MD 20899

U.S. DEPARTMENT OF COMMERCE
Robert A. Mosbacher, Secretary

Lee Mercer, Deputy Under Secretary for Technology

NATIONAL INSTITUTE OF STANDARDS AND TECHNOLOGY
Raymond G. Kammer, Acting Director

NIST

NIST-GCR-90-570

STRUCTURE AND RADIATION PROPERTIES OF TURBULENT DIFFUSION FLAMES

Y. R. Sivathanu
M. E. Kounalakis
G. M. Faeth

University of Michigan
Department of Aerospace Engineering
Ann Arbor, MI

Prepared for
U.S. DEPARTMENT OF COMMERCE
National Institute of Standards and Technology
National Engineering Laboratory
Center for Fire Research
Gaithersburg, MD 20899

February 1990

NIST Grant No. 60NANB8D0833

U.S. DEPARTMENT OF COMMERCE
Robert A. Mosbacher, Secretary

Lee Mercer, Deputy Under Secretary for Technology

NATIONAL INSTITUTE OF STANDARDS AND TECHNOLOGY
Raymond G. Kammer, Acting Director

Notice

This report was prepared for the Center for Fire Research of the National Institute of Standards and Technology under Grant Number 60NANB8D0833. The statements and conclusions contained in this report are those of the authors and do not necessarily reflect the views of the National Institute of Standards and Technology or the Center for Fire Research.

STRUCTURE AND RADIATION PROPERTIES OF TURBULENT DIFFUSION FLAMES

Y. R. Sivathanu, M. E. Kounalakis and G. M. Faeth

The University of Michigan
Department of Aerospace Engineering
Ann Arbor, MI 48109-2140

Annual Report: Grant No. 60NANB8D0833

October 1989

Sponsored by:

U.S. Department of Commerce
National Institute of Standards and Technology
(formerly National Bureau of Standards)
Center for Fire Research
Washington, DC 20234

Notice:

This report was prepared for the Center for Fire Research of the National Engineering Laboratory, National Institute of Standards and Technology (formerly National Bureau of Standards), under Grant Number 60NANB8D0833. The statements and conclusions contained in this report are those of the authors and do not necessarily reflect the views of the National Institute of Standards and Technology or the Center for Fire Research.

STRUCTURE AND RADIATION PROPERTIES OF TURBULENT DIFFUSION FLAMES

October 1989

Sponsored by:

U.S. Department of Commerce
National Institute of Standards and Technology
(formerly National Bureau of Standards)
Center for Fire Research
Washington, DC 20234

Abstract

A theoretical and experimental study of the structure and radiation properties of turbulent diffusion flames is described. The results have application to modeling fires within structures, materials test methods, fire detection systems, and effects of materials on fire properties. The investigation has four phases, as follows: state relationships for major gas species in hydrocarbon/air diffusion flames, soot properties of luminous turbulent diffusion flames, mixture fraction properties of nonluminous turbulent diffusion flames, and mean and fluctuating radiation properties of luminous turbulent diffusion flames.

Generalized state-relationship correlations, giving the mass fractions of major gas species (N_2, O_2, fuel, CO_2, H_2O, CO and H_2) as functions of local fuel-equivalence ratios, were developed for hydrocarbon/air diffusion flames. The data base included measurements in laminar methane, propane, n-heptane, acetylene and ethylene flames burning in air with burner configurations involving porous cylinders in crossflow as well as coflowing jet flames. Reasonably good generalized state-relationship correlations were found for major gas species over the available data base, which included molar fuel H/C ratios in the range 1-4 and fuel-equivalence ratios in the range 10^{-2} - 10^{2}. Typical of state relationships for particular fuels, the generalized state relationships approximated thermodynamic equilibrium for fuel-lean conditions and departed from equilibrium in a relatively universal manner for fuel-rich conditions. The results should be useful for estimating the scalar properties and the infrared gas-band radiation properties of laminar and turbulent hydrocarbon/air diffusion flames — the latter in conjunction with the laminar flamelet concept.

Instantaneous soot volume fractions and temperatures were measured in the fuel-rich (underfire) region of turbulent nonpremixed acetylene, propylene, ethylene and propane flames burning in still air. Large-scale, highly-buoyant, pool-like flames were considered, having characteristic residence times greater than 250 ms and burner exit Richardson numbers greater than 18. Measurements were made using an optical probe that involved laser extinction for soot volume fractions and two-wavelength pyrometry for temperatures. Strong correlations were found between soot volume fractions and temperatures for each fuel — relatively independent of burner operating conditions and position in the underfire region. This behavior is supportive of the existence of nearly universal relationships between soot volume and mixture fractions in the underfire region of turbulent nonpremixed flames having large characteristic residence times. Underfire soot is largely confined to a narrow range of mixture fractions (yielding a soot spike) and temperatures. The latter observation supports approximations of constant-temperature soot layers that have been proposed in the past for estimates of continuum radiation from soot-containing diffusion flames.

Mixture fraction properties in turbulent carbon monoxide/air diffusion flames were measured in order to provide information needed to exploit the laminar flamelet concept for radiation predictions. A two-point Mie scattering system was developed to yield Favre- and time-averaged mean and fluctuating values, probability density functions, temporal spectra and correlations, and spatial correlations of mixture fractions. Measurements showed significant differences (up to 50% near the flame tip) between Favre- and time-averaged mean mixture fractions and intensities of mixture fraction fluctuations. Probability density functions of mixture fractions correlated reasonably well as clipped-Gaussian functions having the same moments, except for the mixture fraction superlayer near the intermittency spike. Temporal correlations and spectra show remarkable similarity for various streamwise and radial positions in the flames when time is normalized by the integral time scale. Additionally, spatial correlations for radial paths are nearly invariant

when distance is normalized by the spatial integral scale. Finally, normalized correlations have been found for temporal and spatial integral scales — the latter being proportional to height above the burner and independent of radial position in spite of effects of intermittency near the edge of the flow. These general correlations are fortuitously simple which will be very helpful for predicting flame radiation properties pending development of theories to describe these properties. Current work involves additional measurements of mixture fraction fluctuations at higher Reynolds numbers as well as consideration of the velocity field of the test flames.

The continuum radiation properties of the underfire region of luminous acetylene and propylene flames burning in still air were studied. Instantaneous radiation intensities at 1000 and 2300 nm, where gas-band radiation is absent, were measured for paths passing through the axis of the flames; and reduced to yield mean and fluctuating values, probability density functions and power spectral densities of spectral radiation intensities. The probability density functions showed a surprising intermittency peak at low radiation levels which appears to be due to puffs of overfire soot passing through the radiation path. The test flames were highly buoyant; therefore, spikes were present in the temporal power spectrum for positions near the burner exit due to pulsations of the luminous portion of the flames. Current work involves measurements of soot volume fraction statistics along the radiation paths so that predictions of continuum radiation properties can be made in order to gain more insight concerning these observations.

ACKNOWLEDGEMENT

This research was supported by the United States Department of Commerce, National Institute of Standards and Technology (formerly National Bureau of Standards), Grant Number 60NANB8D0833, with H. R. Baum of the Center for Fire Research serving as Scientific Officer.

Table of Contents

	Page
Abstract	iv
Acknowledgement	vi
List of Tables	viii
List of Figures	ix
Nomenclature	xii
1. Introduction	1
2. State Relationships for Major Gas Species	3
2.1 Introduction	3
2.2 Measurements	4
2.3 Theoretical Basis for Correlations	9
2.4 Results and Discussion	11
2.5 Conclusions	23
3. Temperature/Soot Volume Fraction Correlations in Turbulent Luminous Flames	24
3.1 Introduction	24
3.2 Experimental Methods	26
3.2.1 Apparatus	26
3.2.2 Instrumentation	28
3.2.3 Test Conditions	32
3.3 Results and Discussion	34
3.3.1 Flame Position and Operating Conditions	34
3.3.2 Conditional PDF's of Temperature	34
3.3.3 Temperature/Soot Volume Fraction Correlations	41
3.4 Conclusions	46
4. Mixture Fractions in Turbulent Flames	47
4.1 Introduction	47
4.2 Experimental Methods	49
4.2.1 Apparatus	49
4.2.2 Instrumentation	49
4.2.3 Test Conditions	55
4.3 Results and Discussion	55
4.3.1 Mixture Fraction Structure	55
4.3.2 PDF's of Mixture Fraction	60
4.3.3 Correlations and Spectra of Mixture Fractions	64
4.4 Conclusions	70
5. Radiation from Luminous Turbulent Flames	71
5.1 Introduction	71
5.2 Experimental Methods	73
5.2.1 Apparatus	73
5.2.2 Instrumentation	73
5.2.3 Test Conditions	74
5.3 Results and Discussion	74
5.3.1 Mean and Fluctuating Spectral Radiation Intensities	74
5.3.2 PDF's of Spectral Radiation Intensities	76
5.3.3 Power Spectral Densities of Spectral Radiation Intensities	80
5.4 Conclusions	84
References	85

List of Tables

Table	Title	Page
1	Summary of Measurements	5
2	Summary of State Relationship Functions for $C_n H_m$/Air Diffusion Flames	12
3	Summary of Stoichiometric Properties	13
4	Test Conditions for Luminous Turbulent Flames	33
5	Properties of Conditional PDF's of Temperature	40
6	Test Conditions for Nonluminous Turbulent Diffusion Flames	56
7	Mean and Fluctuating Spectral Radiation Intensities in the Continuum	75

List of Figures

Figure	Caption	Page
1	State relationship for nitrogen concentrations in hydrocarbon/air diffusion flames.	14
2	State relationship for oxygen concentrations in hydrocarbon/air diffusion flames.	15
3	State relationship for fuel concentrations in hydrocarbon/air diffusion flames.	16
4	State relationship for carbon dioxide concentrations in hydrocarbon/air diffusion flames	17
5	State relationship for water vapor concentrations in hydrocarbon/air diffusion flames.	18
6	State relationship for carbon monoxide concentrations in hydrocarbon/air diffusion flames	19
7	State relationship for hydrogen concentrations in hydrocarbon/air diffusion flames.	20
8	Soot volume fraction state relationships for acetylene/air and ethylene/air diffusion flames. Data and correlations from Sivathanu et al. (1988), Sivathanu and Faeth (1989a) and Gore and Faeth (1986, 1987).	25
9	Sketch of the luminous flame apparatus.	27
10	Sketch of the 50 mm diameter burner.	29
11	Sketch of the underfire optical probe.	30
12	Conditional PDF's of temperature for turbulent acetylene/air diffusion flames.	35
13	Conditional PDF's of temperature for turbulent propylene/air diffusion flames.	36
14	Conditional PDF's of temperature for turbulent ethylene/air diffusion flames.	37
15	Conditional PDF's of temperature for turbulent propane/air diffusion flames.	38
16	Correlation between soot volume fraction and temperature for turbulent acetylene/air diffusion flames.	42
17	Correlation between soot volume fraction and temperature for turbulent propylene/air diffusion flames.	43

Figure	Caption	Page
18	Correlation between soot volume fraction and temperature for turbulent ethylene/air diffusion flames.	44
19	Correlation between soot volume fraction and temperature for turbulent propane/air diffusion flames	45
20	Sketch of nonluminous flame apparatus.	50
21	Sketch of two-point Mie-scattering system.	51
22	State relationships for carbon monoxide/air diffusion flames.	54
23	Favre- and time-averaged mean and fluctuating mixture fractions along the axis of a turbulent carbon monoxide/air diffusion flame: Re = 7400	57
24	Radial profiles of Favre- and time-averaged mean and fluctuating mixture fractions for a turbulent carbon monoxide/air flame: Re = 7400	59
25	Favre- and time-averaged PDF's of mixture fraction in a turbulent carbon monoxide/air diffusion flame: Re = 7400, x/d = 30.	61
26	Favre- and time-averaged PDF's of mixture fraction in a turbulent carbon monoxide/air diffusion flame: Re = 7400, x/d = 40.	62
27	Favre- and time-averaged PDF's of mixture fraction in a turbulent carbon monoxide/air diffusion flame: Re = 7400, x/d = 50.	63
28	Time-averaged temporal correlations of mixture fraction fluctuations in a turbulent carbon monoxide/air diffusion flame: Re = 7400	65
29	Time-averaged power spectral densities of mixture fraction fluctuations along the axis of a turbulent carbon monoxide diffusion flame: Re = 7400.	66
30	Time-averaged spatial correlations of mixture fraction fluctuations in a turbulent carbon monoxide/air diffusion flame: Re = 7400	68
31	Temporal and spatial integral scales in a turbulent carbon monoxide/air diffusion flame: Re = 7400.	69
32	Effect of optical path diameter on PDF's of spectral radiation intensities for turbulent acetylene/air flames.	77
33	PDF's of spectral radiation intensities at 1000 nm for a turbulent acetylene/air diffusion flame: Re 470.	78
34	PDF's of spectral radiation intensities at 2300 nm for a turbulent propylene/air diffusion flame: Re = 1370.	79

Figure	Caption	Page
35	Effect of optical path diameter on power spectral densities of spectral radiation intensities for turbulent acetylene/air diffusion flames.	81
36	Power spectral densities of spectral radiation intensities at 1000 nm for a turbulent acetylene/air diffusion flame: Re = 470.....	82
37	Power spectral densities of spectral radiation intensities at 2300 nm for a turbulent propylene/air diffusion flame: Re = 1370.	83

Nomenclature

Symbol	Description
a	number of moles of O_2 per mole of fuel, acceleration of gravity
A	proportionality constant
b_λ	instrument sensitivity at λ
c	speed of light
d	burner exit diameter
d_p	soot particle diameter
d_{opt}	diameter of radiation path
E(n)	power spectral density of mixture fraction fluctuations
$E_\lambda(n)$	power spectral density of spectral radiation intensity
f	fuel-air mass ratio, mixture fraction
$f_i(\phi)$	universal function of ϕ for species i
f_v	soot volume fraction
$-f_w$	dimensionless fuel ejection rate
f_λ	refractive index parameter
h	Planck's constant
i	$(-1)^{1/2}$
i_λ	spectral radiation intensity
k	Boltzman constant
L	length of optical path
m	number of atoms of H in fuel molecule
M_i	molecular weight of species i
N	number of samples
n	number of atoms of C in fuel molecule
n_j	number of samples in group j
$P(\phi)$	probability density function of ϕ
r	radial distance
R	radius of porous cylinder
Re	Reynolds number
Ri	Richardson number
T	temperature
T_L,T_H	low- and high-temperature peaks of conditional PDF of temperature
T_M	mean value of conditional PDF of temperature
u	streamwise velocity

v_w	fuel velocity at surface of porous cylinder
V	ambient air stream velocity
V_λ	output voltage of instrument at λ
x	height above burner
Y_i	mass fraction of species i

Greek

Δr	crosstream distance increment
ε_λ	spectral emissivity
κ	imaginary part of soot refractive index
λ	wavelength
Λ_r	crosstream integral scale
μ	absolute viscosity
ν	kinematic viscosity
ν_i	number of moles of species i per mole of fuel
ρ	density
σ	standard deviation of conditional PDF of temperature
τ	time difference
τ_I	temporal integral scale
ϕ	fuel-equivalence ratio, generic property
$\psi(Y_i)$	generalized state-relationship function of Y_i

Subscripts

c	centerline value
f	fuel
m	mass-averaged quantity at burner exit
s	stoichiometric condition
o	burner exit, incident laser beam
∞	ambient air condition

1. INTRODUCTION

Radiation from turbulent diffusion flames is an important heat transfer mechanism in fires. Radiant transport influences the rate of burning of objects already on fire, the rate of spread of the fire, and the rate of heating of surrounding structural elements. In spite of significant progress, substantial gaps exist in current understanding of the structure and radiation properties of turbulent diffusion flames. The objective of the present study was to investigate these properties for both nonluminous and luminous (nonsooting and sooting) buoyant turbulent diffusion flames. The results of the research have application to modeling fires within structures, materials test methods, fire detection, and effects of materials on fire properties.

The present investigation of the structure and radiation properties of buoyant turbulent diffusion was divided into four phases. The first phase concerns generalized state relationships for the concentrations of major gas species in hydrocarbon (C_nH_m)/air diffusion flames. State relationships are correlations between particular properties (the mass fractions of major gas species in this case) and a conserved scalar of the flow (often mixture fraction, which is the elemental fraction of mass in a sample that originated from the fuel). The existence of state relationships in turbulent diffusion flames vastly simplifies analysis of scalar properties needed for radiation predictions since models and computations need only find the conserved scalar while all other properties follow from the state relationships (this approach is often called the laminar flamelet concept). Recent work has shown the existence of state relationships for major gas species in hydrocarbon/air diffusion flames except near points of flame attachment and extinction, even in flames having appreciable concentrations of soot (Bilger, 1977; Gore and Faeth, 1986, 1987; Jeng and Faeth, 1984a,b; Liew et al., 1981, 1984; Mitchell et al., 1980a,b; Moore and Moore, 1976; Saito et al., 1986; Sivathanu et al., 1988; Smyth et al., 1985). However, state relationships differ for each fuel/air combination and their determination requires tedious and difficult measurements within laminar diffusion flames. The objective of this phase of the investigation was to seek generalized state relationships for the concentrations of major gas species within C_nH_m/air flames in order to avoid the need to develop specific state relationships for each fuel. The present study only considered existing measurements during development of these correlations since state relationships for a relatively wide range of hydrocarbon fuels are currently available, e.g., past studies have considered molar H/C ratios (m/n) in the range 1-4.

The second aspect of the investigation relates to the existence of state relationships for soot volume fractions in luminous turbulent diffusion flames so that the laminar flamelet concept can be applied to this property as well. Since soot particles are relatively small, continuum radiation from soot in luminous flames can be found using the Rayleigh approximation for small particles and scattering can be ignored (Tien and Lee, 1982). Then, the main soot property that is needed for continuum radiation predictions is the soot volume fraction rather than soot particle sizes, shapes or number densities. Motivated by results in the literature that suggested the potential for existence of soot volume fraction state relationships in turbulent diffusion flames (Becker and Liang, 1982; Kent, 1987; Kent and Bastin, 1984; Kent and Honnery, 1987) earlier work in this laboratory studied soot volume fraction state relationships as a means of avoiding the complexity of estimates of soot chemistry in turbulent environments (Faeth, 1988; Faeth et al., 1988a,b; Gore and Faeth, 1986, 1987; Sivathanu and Faeth, 1989a; Sivathanu et al., 1987, 1988). It was found that soot volume fraction state relationships existed for the fuel-rich region of laminar ethylene and acetylene/air flames; and within the overfire region of turbulent ethylene, acetylene, propylene and propane/air flames at sufficiently long flame residence times (residence times longer than roughly ten times the laminar smoke-point residence time). The objective of the present investigation was to examine whether soot volume fraction

state relationships existed in the fuel-rich (underfire) region of turbulent diffusion flames as well. The complexity of measurements of mixture fractions in soot-containing turbulent diffusion flames required that the assessment be made indirectly; thus, instantaneous soot volume fractions and temperatures were measured to see if they were consistent with the existence of soot volume fraction state relationships. The flames considered included acetylene, propylene, ethylene and propane flames burning in still air.

The third aspect of the investigation relates to the mixture fraction properties of turbulent diffusion flames since evidence continues to mount that mixture fractions are the key to predicting scalar properties through the use of the laminar flamelet concept and state relationships for each scalar property of interest. Mixture fraction properties needed for numerical simulation of flame radiation properties, using statistical time series simulation methods described by Box and Jenkins (1976), were studied, as follows: probability density functions, spatial correlations, and temporal correlations and spectra. Past studies of mixture fractions have concentrated on mean and fluctuating values for nearly constant density nonreacting conditions (Becker et al., 1967; Birch et al., 1978; Corrsin and Uberoi, 1951; Pitts and Kashiwagi, 1984) while comparable measurements in flames are very limited (Stårner and Bilger, 1980). Thus, the objective of the present investigation was to help fill this gap in the literature by measuring moments, probability density functions, spatial correlations, and temporal correlations and spectra in turbulent carbon monoxide jet flames burning in still air. The measurements were carried out using a two-point Mie scattering system with the data reduced to yield both mass-weighted (Favre) and time-averaged mixture fraction properties.

The fourth aspect of the investigation relates to turbulence/radiation interactions in luminous diffusion flames. Past work has shown that turbulence/radiation interactions cause mean radiation levels of flames to be biased upward (often by factors as high as 2-3) from estimates based on the distribution of mean scalar properties in the flames (Cox, 1977; Faeth, 1988; Faeth et al., 1988a,b; Fisher et al., 1987; Gore and Faeth, 1986, 1987; Gore et al., 1987a,b,c; Kabashnikov and Kmit, 1979; Portscht, 1974). A stochastic method for treating these interactions was developed in this laboratory by Jeng et al. (1984); furthermore, subsequent work showed that the approach was promising (see Faeth (1988) and Faeth et al. (1988a,b) and references cited therein). However, aspects of the method were *ad hoc* and its evaluation was only indirect, based on differences between mean property and stochastic predictions and their comparison with measurements of mean radiation levels from turbulent diffusion flames. More recent work has studied turbulence/radiation interactions more directly by measuring the mean and fluctuating radiation properties of nonluminous turbulent diffusion flames (Kounalakis et al., 1988, 1989). These results showed that the properties of radiation fluctuations provided reasonably definitive information for evaluating stochastic analysis of turbulence/radiation interactions. Thus, the objective of the present investigation was to extend these results to the mean and fluctuating properties of continuum radiation from turbulent luminous flames. This involved measurements of the moments, probability density functions, and temporal correlations and spectra of spectral radiation intensities for horizontal radial paths through highly buoyant (pool-like) flames. The measurements were limited to continuum regions of the infrared portion of the spectrum, with no gas bands present, for turbulent acetylene and propylene flames burning in still air.

Progress on each aspect of the study is described in the following. The investigations of generalized state relationships in diffusion flames and soot volume fraction/temperature correlations in the underfire region of turbulent luminous flames have been completed and are also described in recent publications (Sivathanu et al., 1989b,c). The investigations of the mixture fraction properties and mean and fluctuating continuum radiation properties in turbulent diffusion flames have not been completed and the

following represents only reports of progress in these areas. The following report considers each phase of the investigation in turn: state relationships for major gas species, temperature/soot volume fraction correlations, mixture fractions, and radiation from luminous turbulent flames. Each aspect is taken up independently so that topics can be skipped if desired with no loss of continuity.

2. STATE RELATIONSHIPS FOR MAJOR GAS SPECIES

2.1 Introduction

The conserved-scalar formalism is widely used to analyze laminar and turbulent diffusion flames since it simplifies the formulation considerably. The approach is based on the assumption that the scalar properties of interest are only functions of a scalar property that is conserved in the presence of chemical reactions—like the mixture fraction (the fraction of elemental mass in a mixture that originated from the burner). These functions are called state relationships. The objective of this portion of the investigation was to study whether generalized state relationships for major gas species could be found for hydrocarbon (C_nH_m)/air diffusion flames.

The formal existence of state relationships requires that a number of conditions be satisfied, namely: equal exchange coefficients of all species and heat, fast rates of chemical reaction so that local thermodynamic equilibrium is maintained, and negligible kinetic energy and radiative heat losses. These conditions are rarely satisfied in practice for hydrocarbons; nevertheless, Bilger (1977) discovered that state relationships still existed for major gas species—at least within uncertainties representative of measurements and the needs of most practical mixing and heat transport calculations. Bilger's (1977) observation was based on measurements in laminar methane/air and propane/air flames by Tsuji and Yamaoka (1968, 1970) and n-heptane/air flames by Abdel-Khalik et al. (1974). It was found that the concentrations of major gas species approximated local thermodynamic equilibrium for fuel-lean conditions. Processes of fuel decomposition and soot chemistry caused substantial departures from equilibrium for fuel-rich conditions; nevertheless, the departures from equilibrium proved to be relatively universal over the range of the data so that reasonably good state relationships were found for each fuel at these conditions as well. Furthermore, the correlations were relatively insensitive to mass diffusion rates (or Damkohler numbers) in laminar flames, even for conditions nearing extinction for propane/air flames. This suggested that state relationships found in laminar flames might also be applied to turbulent flames, assuming that turbulent flames consisted of wrinkled laminar flamelets: this extension is commonly called the laminar-flamelet approximation (concept) of turbulent diffusion flames.

Subsequently, other measurements of species concentrations in laminar diffusion flames were used to study the laminar-flamelet concept for a variety of hydrocarbon diffusion flames burning in air, as follows: iso-octane (Moore and Moore, 1976), methane (Mitchell et al., 1980a,b; Smyth et al., 1985; Saito et al., 1986), natural gas (Gore et al., 1987), ethylene (Gore, 1986; Gore and Faeth, 1986) and acetylene (Gore, 1986; Gore and Faeth, 1987). Similar to the findings of Bilger (1977), state relationships for major gas species approximated thermodynamic equilibrium for fuel-lean conditions with relatively universal departures from equilibrium for fuel-rich conditions. Findings for ethylene and acetylene were particularly encouraging since they imply that the laminar flamelet concept remains viable even in the presence of large concentrations of soot for fuel-equivalence ratios greater than unity.

The connection between state relationships measured in laminar flames and the scalar properties of turbulent flames has also been studied. Liew et al. (1981, 1984) analyzed laminar methane/air flames for different levels of flame stretch showing that state relationships remained nearly universal until extinction conditions were approached. Furthermore, measurements of species concentrations in turbulent jet diffusion flames in this laboratory showed that compositions of turbulent flames were consistent with state relationships measured in laminar flames, except near points of flame attachment. These results included a variety of hydrocarbon fuels burning in still air, as follows: methane (natural gas) (Jeng and Faeth, 1984a), propane (Jeng and Faeth, 1984b), ethylene (Gore, 1986; Gore and Faeth, 1986; Sivathanu et al., 1988) and acetylene (Gore, 1986; Gore and Faeth, 1987; Sivathanu et al., 1988).

Thus, past studies suggest that the laminar-flamelet concept for major gas species is useful for both laminar and turbulent diffusion flames. A difficulty in applying the concept, however, is that the state relationships differ for each hydrocarbon; therefore, measurements in laminar flames are generally required to develop state relationships for each fuel of interest. This is not a very attractive prospect: measurements in laminar flames to find state relationships are difficult and tedious—particularly in soot-containing flames where sampling probes encounter problems of clogging. Thus, the present investigation was undertaken to see if these difficulties could be circumvented to some extent by finding generalized state relationship correlations for the concentrations of major gas species for hydrocarbons (C_nH_m) burning in air. The study only considered existing measurements since a relatively wide variety of hydrocarbon fuels has been considered, e.g., they include molar H/C ratios (m/n) in the range 1-4.

In the following, the measurements used to develop the generalized state relationship correlations are discussed first. The theoretical basis for the correlations is then described. This section concludes with a discussion of the correlations themselves, considering the major gas species in turn, i.e., N_2, O_2, fuel, CO_2, H_2O, CO and H_2.

2.2 Measurements

General. Numerous measurements of species concentrations within laminar diffusion flames have been reported in the literature, however, only a few are sufficiently complete to allow correlations of the results in terms of mixture fractions. Thus, it was necessary to limit development of the correlations to the following measurements: Tsuji and Yamaoka (1968, 1970), and Mitchell et al. (1980a,b); Smyth et al. (1985) and Saito et al. (1986) for methane; Tsuji and Yamaoka (1968) for propane; Abdel-Khalik et al. (1978) for n-heptane; and Gore (1986) and Gore and Faeth (1986, 1987) for acetylene and ethylene. These experiments will be described briefly in the following: their major features are summarized in Table 1.

Tsuji and Yamaoka (1968, 1970). The measurements of species concentrations in laminar methane/air and propane/air flames by Tsuji and Yamaoka (1968, 1970) involved fuel flowing from a porous cylinder with an air stream flowing across the cylinder. The flame was stabilized around the periphery of the cylinder while the measurements were made along the forward stagnation line of the flow. Flame operating conditions were characterized by two parameters: (1) the stagnation velocity gradient, 2 V/R, where V is the ambient air stream velocity and R is the cylinder radius; and (2) the dimensionless fuel ejection rate, $-f_w = (v_w/V)(Re/2)^{1/2}$, where v_w is the fuel velocity at the cylinder surface, $Re = VR/\nu$ and ν is the mean kinematic viscosity of the flow. High values of the stagnation velocity gradient and low values of the dimensionless fuel ejection rate caused the flames to extinguish, which defined a blow-off limit. In contrast, low values of the stagnation velocity gradient and high values of the dimensionless fuel ejection rate resulted in flames

Table 1 Summary of Measurements[a]

Fuel	Source	Burner Configuration	Dimensions	Cold-Flow Velocities (cm/s)	
				Air	Fuel[b]
CH_4	Tsuji and Yamaoka (1968, 1970)	Forward stagnation point of a porous cylinder flowing fuel burning in an air crossflow	60 mm cylinder diameter	150 225	29 36
CH_4	Mitchell et al. (1980a,b)	Coflowing round jet flame	Fuel and air port diameters of 12.7 and 50.8	9.9	4.5
CH_4	Saito et al. (1986)	Coflowing round jet flame	Fuel and air port diameters of 16 and 70 mm	9.3	0.54-2.2
CH_4	Smyth et al. (1985)	Wolfhard-Parker slot burner	Fuel and air ports 8 and 16 × 41 mm, air ports on both sides of fuel port	19.4	9.7
C_3H_8	Tsuji and Yamaoka (1968)	Forward stagnation point of a porous cylinder flowing fuel burning in an air crossflow	60 mm cylinder diameter	225 225 525	19 5 29
C_7H_{16}	Abdel-Khalik et al. (1974)	Periphery of a fuel-wetted porous cylinder burning in an air crossflow	12.8 mm cylinder diameter	40	0.02-0.62
C_2H_2	Gore (1986), Gore and Faeth (1987)	Coflowing round jet flame	Fuel and air port diameters of 14.3 and 102 mm	5.6 10.7	3.5 6.1
C_2H_4	Gore (1986), Gore and Faeth (1986)	Coflowing round jet flame	Fuel and air port diameters of 14.3 and 102 mm	10.5 10.5 11.9	3.1 3.4 4.3

[a]Nonpremixed combustion of fuel and air with reactants initially at normal temperature and pressure.

[b]Computed for Tsuji and Yamaoka (1968, 1970) assuming an average kinematic viscosity of 75×10^{-6} m^2/s.

having a luminous yellow zone indicative of the presence of soot at the forward stagnation point. Structure measurements were made between these limits, where stable blue flames were observed.

Structure measurements for methane/air flames are reported for 2V/R = 100 and 150 s^{-1} and $-f_w$ = 0.8 and 1.5, respectively. The corresponding luminous flame and blow-off limits for this range of $-f_w$ are 2V/R = 70 and 300 s^{-1}, respectively. Structure measurements for propane/air flames are reported for three conditions, as follows: 2V/R = 150, 150 and 350 s^{-1} and $-f_w$ = 0.8, 0.2 and 0.8. The corresponding blue-flame and blow-off limits for this range of $-f_w$ are 2V/R = ca. 70 and 350 s^{-1}. The second condition represents the lower limit of the range where concentrations remain independent of $-f_w$ within the luminous region; however, these concentrations only change about 20% as $-f_w$ is reduced to the blow-off limit. The third condition is near the blow-off limit with respect to 2V/R for $-f_w$ = 0.8; however, results for the first and third conditions (which have the same value of $-f_w$) are nearly the same. Furthermore, specific plots of the mole fractions of CO_2 and C_2H_4 for 2V/R = 150-350 s^{-1} and $-f_w$ = 0.8 show changes of maximum concentrations of only 15-20%. These findings suggest that effects of approaching the blow-off limit within the range of these tests is not large, in agreement with the theoretical findings of Liew et al. (1981, 1984) for methane/air diffusion flames.

Composition measurements were made with a gas chromatograph using a quartz microprobe for sampling. Species concentrations reported in all cases include N_2, O_2, CO_2, CO, H_2, CH_4, C_2H_2, C_2H_4, C_2H_6, C_3H_6 and C_3H_8. Results are reported on a dry basis except for one methane/air flame (2V/R = 150 s^{-1} and $-f_w$ = 1.5). When not reported, the concentration of water vapor was estimated by assuming that the molal H/C ratio of the mixture was the same as the original fuel and that all the missing hydrogen was present as water vapor. Given this estimate of water vapor concentration, the molecular weight of the mixture could be computed, allowing calculation of the mass fractions of all the species. In view of the additional uncertainties concerning water vapor, mixture fractions (or equivalently, the fuel-equivalence ratios) were found from the measured concentrations of carbon and nitrogen while assuming that the H/C ratio of the original fuel was preserved throughout the flow field. Experimental uncertainties of the concentration measurements of Tsuji and Yamaoka (1968, 1970) are not reported; however, in view of the consistency of the results for various test conditions it is felt that the uncertainties of these measurements are no larger than those of Gore (1986) and Gore and Faeth (1986, 1987) to be discussed later.

Abdel-Khalik et al. (1974). The measurements of Abdel-Khalik et al. (1974) for laminar n-heptane/air flames were also carried out using a porous cylinder in an air stream flowing across the cylinder. In this case, the cylinder was fed with the liquid fuel at a rate which kept the surface wetted but not dripping. The flame was stabilized around the periphery of the cylinder. Measurements are reported along radial lines at various angles from the forward stagnation point (0, 90 and 180°). Results are limited to a single value of 2V/R = 125 s^{-1}, which is stated to be well below blow-off conditions; for comparison, Tsuji and Yamaoka (1968, 1970) observed blow-off conditions for methane and propane/air diffusion flames of 2V/R ca. 300-350 s^{-1} for the same burner configuration. Relative rates of diffusion at various points within the flame, for fuel-equivalence ratios in the range 1-3, were evaluated by Bilger (1977): they varied over three orders of magnitude over the region where measurements were made, implying a wide range of Damkohler numbers for the flow. Fuel velocities at the liquid surface were estimated from gas-phase composition gradients near the surface: they varied circumferentially with the largest and smallest values, at the forward and rearward stagnation points, listed in Table 1. The flames were blue at the forward stagnation point with some degree of yellow luminousity due to the presence of soot at other locations.

Composition measurements were obtained with a gas chromatograph and quartz microprobe, similar to Tsuji and Yamaoka (1968, 1970). Species concentrations were reported on a dry basis and included N_2, O_2, CO_2, CO, CH_4, C_2H_2, C_2H_4 and C_7H_{16}. The concentration of water vapor was determined in the same manner as the data of Tsuji and Yamaoka (1968, 1970) reported on a dry basis. Unfortunately, Abdel-Khalik et al. (1974) do not report measurements of hydrogen; therefore, assigning all missing hydrogen to water vapor overestimates the concentration of water vapor for fuel-rich conditions (on the order of 20-50%). Mixture molecular weights, mass fractions, and fuel-equivalence ratios were found in the same manner as the measurements of Tsuji and Yamaoka (1968, 1970). Abdel-Khalik et al. (1974) do not provide uncertainty estimates for their measurements, however, internal consistency appears to be about the same as the measurements of Tsuji and Yamaoka (1968, 1970).

Mitchell et al. (1980a,b). The measurements of Mitchell et al. (1980b) for laminar methane/air flames were carried out using a coflowing round jet burner. The fuel was in the central jet with both jets being directed vertically upward. The flame attached naturally at the burner exit and was 58 mm high. The region where the flame was present was surrounded by a cylindrical pyrex shield to reduce effects of room disturbances. Radial profiles of species concentrations were measured at 12, 24 and 50 mm above the burner exit.

Samples were withdrawn from the flame using a quartz microprobe. Gas partitioners were used to find the concentrations of N_2, O_2, CO_2, CO, H_2 and CH_4. The concentration of argon was found by assuming that the proportions of argon and nitrogen were the same as in ambient air. The concentration of water vapor was determined by measuring the dewpoint of the sample. Mixture molecular weights, mass fractions and fuel equivalence ratios were found in the same manner as the data of Tsuji and Yamaoka (1968, 1970). The measurements also included temperatures, using a corrected fine-wire thermocouple; and velocities, using laser velocimetry. Mitchell et al. (1980b) checked the internal consistency of the data by comparing fluxes of elemental carbon and hydrogen at the measuring stations with the burner input: carbon fluxes agreed within 8%, hydrogen fluxes agreed within 9%. Based on these observations, the measurements of water vapor concentrations are more accurate than results estimated from the measurements of Tsuji and Yamaoka (1968, 1970) and Abdel-Khalik et al. (1974) made on a dry basis, while other uncertainties seem comparable to Gore (1986) and Gore and Faeth (1986, 1987)

Smyth et al. (1985). The measurements of Smyth et al. (1985) for laminar methane/air flames were carried out using a coflowing Parker-Wolfhard slot burner. Injection was vertically upward with a center fuel slot, 8×41 mm, between two air slots, 16×41 mm (each). The flame attached naturally at the burner exit and had a total flame height of roughly 300 mm, with the upper end stabilized from flapping by using curved screens. Measurements relating to state relationships for major gas species were undertaken 4, 10 and 16 mm above the burner exit.

Samples were withdrawn from the flame using a quartz microprobe with an orifice diameter of roughly 140 μm. A quadrupole mass spectrometer was used to find the concentrations of N_2, O_2, CO_2, H_2O, H_2 and CH_4. CO and N_2 were monitored simultaneously at mass 28; therefore, the concentration of CO was found assuming that the water-gas shift reaction was equilibriated. It was found that the data for the concentrations of major gas species (CH_4, O_2, H_2O, CO_2 and H_2) collapsed to single curves for each species as a function of fuel-equivalence ratio — satisfying the laminar flamelet concept. Minor species in this flame (like C_2H_2 and C_6H_6), however, exhibited variations with flame height that suggested effects of finite rate chemistry in the lower portion of the flame.

Summing mole fractions yielded values within 5% of unity; thus, experimental uncertainties appear to be comparable to the other studies listed in Table 1.

Saito et al. (1986). The measurements of Saito et al. (1986) for laminar methane/air flames were carried out using a coflowing round jet burner similar to Mitchell et al. (1980a,b). The flames attached naturally at the burner exit. Four flames were considered, as follows: a fuel velocity of 0.54 cm/s yielding a flame height of 10 mm with an entirely blue flame; a fuel velocity of 0.84 m/s yielding a flame height of 16 mm with a small region of yellow at the tip; a fuel velocity of 1.26 cm/s yielding a flame height of 20 mm with distinguishable yellow and orange regions inside the blue; and a fuel velocity of 2.2 cm/s yielding a flame height of 38 mm where the yellow and orange regions were merged. Measurements were undertaken 10, 14 and 38 mm above the burner exit.

Samples were withdrawn from the flame using a quartz microprobe with a 100 μm diameter entrance port at the tip. A gas chromatograph was used to measure N_2, O_2, CO_2, CO, H_2O, H_2, CH_4, $C_2H_2 + C_2H_4$ and C_2H_6; however, H_2O was only measured for the largest flame. Experimental uncertainties are not estimated by Saito et al. (1986) but appear to be comparable to the other studies listed in Table 1.

Saito et al. (1986) compare their state relationships for O_2, CO_2, CO, H_2O, H_2 and CH_4 with those of Tsuji and Yamaoka (1968, 1970) and Mitchell et al. (1980a,b) finding generally similar results; therefore, the earlier data will be used to represent methane/air flames in the following in order to reduce cluttering of the figures. Similar to Smyth et al. (1985), concentrations of minor species showed significant changes with increasing height above the burner.

Gore (1986), Gore and Faeth (1986, 1987). Full details of these measurements, and a complete tabulation of data, are provided by Gore (1986) while Gore and Faeth (1986, 1987) report the results and summarize methods in readily accessible references. The measurements for laminar acetylene/air and ethylene/air flames were carried out in a coflowing round jet burner, with the fuel flowing from the central jet, similar to Mitchell et al. (1980a,b). The region where the flame was present was surrounded by a round quartz shield, with a fine-mesh screen across the top, to reduce effects of drafts. Two flame conditions were considered for acetylene/air flames, both of which yielded sooting flames. Radial profiles of concentrations were measured at 16, 35 and 88 mm above the exit for the first flame; and 14, 29 and 62 mm above the exit for the second flame. Three flame conditions were considered for ethylene/air flames, involving nonsooting, incipient sooting and sooting flames. Radial profiles of concentrations were measured at the following heights above the burner exit: 31, 45 and 62 mm for the nonsooting flame; 14, 35 and 56 mm for the incipient sooting flame; and 20, 43 and 60 mm for the sooting flame.

Gas compositions were measured using a quartz microprobe and a gas chromatograph. The measurements yielded concentrations of N_2, O_2, CO_2, H_2O, CO, H_2, CH_4, C_2H_2, C_2H_4 and C_2H_6. The fuel-equivalence ratio was based on the total carbon from all gas species and nitrogen, assuming that the H/C ratio of the fuel was preserved. To reduce the uncertainties of this procedure, positions involving significant concentrations of soot (found using laser extinction measurements) were not considered (probing such regions was difficult in any event due to rapid accumulation of soot on the probe). Uncertainties of the concentration measurements were estimated to be less than 15% near the maximum concentration of á species and proportionately higher elsewhere. The measurements were repeatable within this range. Uncertainties of calculations of fuel-equivalence ratios are estimated to be less than 15% as well.

2.3 Theoretical Basis of the Correlations

Based on the studies summarized in Table 1 each fuel/air combination that was considered exhibited reasonably good state relationships for the concentrations of major gas species: methane/air, propane/air, n-heptane/air, acetylene/air, and ethylene/air. The objective of present work was to combine these results to obtain generalized correlations spanning the H/C ratios of the fuels being considered—and presumably other hydrocarbon/air flames as well.

The correlations were developed by insuring that they could handle various H/C ratios for fuel-lean conditions, noting that only saturated combustion products are observed for very low fuel-equivalence ratios while effects of dissociation are modest near stoichiometric conditions for hydrocarbon/air diffusion flames. The present hypothesis was that effects of H/C ratio would scale in the same manner for fuel-rich conditions since properties in this region either are primarily controlled by passive mixing (N_2 always and other species at large fuel-equivalence ratios where temperatures, and thus reaction rates, are low) or exhibit a type of quasi-equilibrium (or at least universal behavior) that appears to be related to concentrations at the stoichiometric condition (species other than N_2 at intermediate fuel-equivalence ratios). Thus, normalizations based on properties at the stoichiometric mixture ratio were used when convenient. All normalizing parameters were based on fuel-lean stoichiometry yielding only saturated combustion products so that they can be found with little difficulty for a particular fuel.

The analysis was based on dry ambient air with minor constituents taken to be equivalent to nitrogen. A general hydrocarbon, C_nH_m, reacting with dry air to yield saturated combustion products at lean conditions, has the following stoichiometry on a per mole of fuel basis:

$$C_nH_m + a(O_2 + 3.76\,N_2) \rightarrow n\,CO_2 + (m/2)H_2O + (a\text{-}n\text{-}(m/4))O_2 + 3.76a\,N_2 \qquad (1)$$

where a is the molal air-fuel ratio parameter. The mass fraction, Y_i, of any species appearing on the RHS of equation (1) can be found from the following expression:

$$Y_i = \nu_i M_i / (M_f + 137.28a) \qquad (2)$$

where ν_i is the number of moles of a product species, i, per mole of fuel (e.g., $\nu_{CO_2} = n$); M_i is the molecular weight of species i, and the subscript f denotes the fuel. The parameter a is related to the fuel-air mass ratio, f, as follows:

$$f = M_f / (137.28a) \qquad (3)$$

Finally, the fuel-equivalence ratio, ϕ, has the following definition:

$$\phi = f / f_s \qquad (4)$$

where the subscript s denotes a quantity at the stoichiometric condition.

Substituting equations (3) and (4) into equation (2), and using ambient and stoichiometric conditions to simplify the expression, yields the following relationship between ϕ and the mass fraction of nitrogen:

$$\phi^{-1} = \left(\frac{Y_{N_2\infty} - Y_{N_2s}}{Y_{N_2\infty} - Y_{N_2}} \right) \left(\frac{Y_{N_2}}{Y_{N_2s}} \right) \equiv \psi(Y_{N_2}) \tag{5}$$

where the subscript ∞ denotes ambient air conditions. The function $\psi(Y_{N_2})$ allows for variations of n and m through Y_{N_2s} (which can be found from equations (1) and (2) for stoichiometric conditions); therefore, this function was used to plot the generalized state relationship for the mass fraction of nitrogen.

The generalized state relationship functions for the mass fractions of oxygen, carbon dioxide and water vapor can be found in the same manner, as follows:

$$1 - \phi = \left(\frac{32n + 8m + M_f Y_{O_2\infty}}{32n + 8m + M_f Y_{O_2}} \right) \left(\frac{Y_{O_2}}{Y_{O_2\infty}} \right) \equiv \psi(Y_{O_2}) \tag{6}$$

$$\phi = \left(\frac{44n - M_f Y_{CO_2s}}{44n - M_f Y_{CO_2}} \right) \left(\frac{Y_{CO_2}}{Y_{CO_2s}} \right) \equiv \psi(Y_{CO_2}) \tag{7}$$

and

$$\phi = \left(\frac{9m - M_f Y_{H_2O_s}}{9m - M_f Y_{H_2O}} \right) \left(\frac{Y_{H_2O}}{Y_{H_2O_s}} \right) \equiv \psi(Y_{H_2O}) \tag{8}$$

In arriving at equation (6) for $\psi(Y_{O_2})$, $Y_{O_{2s}} = 0$ has been used, an approximation that follows from equation (1); furthermore, $1-\phi$ appears on the LHS of equation (6) for convenience in plotting the state relationship. The mass fractions of carbon dioxide and water vapor at stoichiometric conditions were obtained from equations (1) and (2) as noted earlier.

Development of the generalized state relationship correlations could not be guided by equation (1) for fuel-rich conditions since stoichiometry, assuming only the presence of saturated combustion products, was no longer relevant. Thus, the relationship for the fuel was obtained by simply assuming its mass fraction was a universal function of ϕ, e.g.

$$\phi_f(\phi) = Y_f \equiv \psi(Y_f) \tag{9}$$

This is plausible since the fuel mass fraction must approach unity for large ϕ and approaches zero as ϕ approaches unity. The corresponding relationships for carbon monoxide and hydrogen were obtained by assuming that Y_{CO} was analogous to Y_{CO_2} in equation (7), and that Y_{H_2} was analogous to Y_{H_2O} in equation (8), yielding functions of the mass fractions that are universal functions of ϕ, as follows:

$$f_{CO}(\phi) = \left(\frac{44n - M_f Y_{CO_2s}}{44n - M_f Y_{CO}} \right) \left(\frac{Y_{CO}}{Y_{CO_2s}} \right) \equiv \psi(Y_{CO}) \tag{10}$$

$$f_{H_2}(\phi) = \left(\frac{9m - M_f Y_{H_2O_s}}{9m - M_f Y_{H_2}} \right) \left(\frac{Y_{H_2}}{Y_{H_2O_s}} \right) \equiv \psi(Y_{H_2}) \tag{11}$$

A variety of other functions, as well as molal-based correlations of these parameters, were studied; however, none of these proved to be more effective for achieving generalized correlations than equations (9)-(11).

2.4 Results and Discussion

Correlations. The generalized state relationships for the concentrations of major gas species involve plots of the $\psi(Y_i)$ as a function of ϕ. The species considered include: N_2, O_2, fuel, CO_2, H_2O, CO and H_2. For convenience, the state relationship functions, $\psi=\psi(Y_i)$, for each of these species are summarized in Table 2. The normalizing factors ($Y_{N_{2s}}$, $Y_{CO_{2s}}$ and $Y_{H_2O_s}$) used for the fuels within the present data base are summarized in Table 3. The value of $Y_{N_{2s}}$ is nearly constant since the stoichiometric fuel-air mass ratio of hydrocarbons does not vary significantly. Due to the large range of molar H/C ratios of the fuels in the data base, however, the relative proportions of carbon dioxide and water vapor in the combustion products changes significantly: this is reflected by the relatively large variations of $Y_{CO_{2s}}$ and $Y_{H_2O_s}$ in Table 3.

Past work has shown that the concentrations of major gas species approximate thermodynamic equilibrium for fuel-lean conditions; therefore, equilibrium predictions were plotted along with the measurements. Predictions were found using the Gordon and McBride (1971) code, suppressing the formation of solid carbon (soot) for fuel-rich conditions, similar to past work (Abdel-Khalik et al., 1974; Mitchell et al., 1980a; Gore, 1986; Gore and Faeth, 1986, 1987; Gore et al., 1986).

The generalized state relationships for the mass fractions of N_2, O_2, fuel, CO_2, H_2O, CO and H_2 appear in Figs. 1-7, respectively. The fuel and the source of the measurements are identified on the plots. Measurements for methane/air flames are limited to Tsuji and Yamaoka (1968, 1970) and Mitchell et al. (1980b) in order to avoid overemphasizing results for this reactant combination; notably, the other measurements of Smyth et al. (1985) and Saito et al. (1986) generally agree with the results that are plotted. The various flame conditions within each data set are not identified in order to avoid cluttering of the figures; however, that should not be a factor to the extent that the laminar flamelet concept is correct. Equilibrium predictions are illustrated on all the plots except for the fuel (Fig. 3) which is only present for fuel-rich conditions where the equilibrium predictions are not very useful. When the equilibrium predictions were plotted in terms of the $\psi(Y_i)$ as a function of ϕ, the results for the various fuels were the same within the accuracy of plotting; therefore, only a single line appears on each plot. This suggests that the functional forms listed in Table 2, based on complete reaction to saturated combustion products, are reasonably effective for handling effects of H/C ratio at fuel-lean conditions. This result is not surprising since state relationships for the concentrations of major gas species generally satisfy equilibrium predictions for fuel-lean conditions while effects of dissociation are modest when initial fuel and air temperatures are normal for hydrocarbon/air diffusion flames.

The generalized state relationship for the mass fraction of nitrogen appears in Fig. 1. Nitrogen acts primarily like chemically inert diluent in hydrocarbon/air diffusion flames; therefore, both predictions and measurements are in good agreement with the mixing-controlled expression of equation (5). The measurements exhibit increased scatter as ϕ becomes small; however, this is largely due to experimental errors which have a greater effect on $\psi(Y_{N_2})$ as Y_{N_2} approaches $Y_{N_{2\infty}}$ since the difference between these quantities appears in the denominator of the generalized state relationship function for Y_{N_2}.

Table 2 Summary of Generalized State Relationship Functions for C_nH_m/Air Diffusion Flames

Species i	$\psi(Y_i)$
N_2	$\left(\frac{Y_{N_{2\infty}} - Y_{N_{2s}}}{Y_{N_{2\infty}} - Y_{N_2}}\right)\left(\frac{Y_{N_2}}{Y_{N_{2s}}}\right)$
O_2	$\left(\frac{32n + 8m + M_f Y_{O_{2\infty}}}{32n + 8m + M_f Y_{O_2}}\right)\left(\frac{Y_{O_2}}{Y_{O_{2\infty}}}\right)$
Fuel	Y_f
CO_2	$\left(\frac{44n - M_f Y_{CO_{2s}}}{44n - M_f Y_{CO_2}}\right)\left(\frac{Y_{CO_2}}{Y_{CO_{2s}}}\right)$
H_2O	$\left(\frac{9m - M_f Y_{H_2O_s}}{9m - M_f Y_{H_2O}}\right)\left(\frac{Y_{H_20}}{Y_{H_2O_s}}\right)$
CO	$\left(\frac{44n - M_f Y_{CO_{2s}}}{44n - M_f Y_{CO}}\right)\left(\frac{Y_{CO}}{Y_{CO_{2s}}}\right)$
H_2	$\left(\frac{9m - M_f Y_{H_2O_s}}{9m - M_f Y_{H_2}}\right)\left(\frac{Y_{H_2}}{Y_{H_2O_s}}\right)$

Table 3 Summary of Stoichiometric Properties[a]

Fuel	$Y_{N_{2s}}$	$Y_{CO_{2s}}$	$Y_{H_2O_s}$
CH_4	0.725	0.151	0.124
C_3H_8	0.721	0.181	0.098
C_7H_{16}	0.719	0.191	0.090
C_2H_2	0.713	0.238	0.049
C_2H_4	0.718	0.200	0.082

[a]Found assuming complete reaction to saturated combustion products for combustion in dry air.

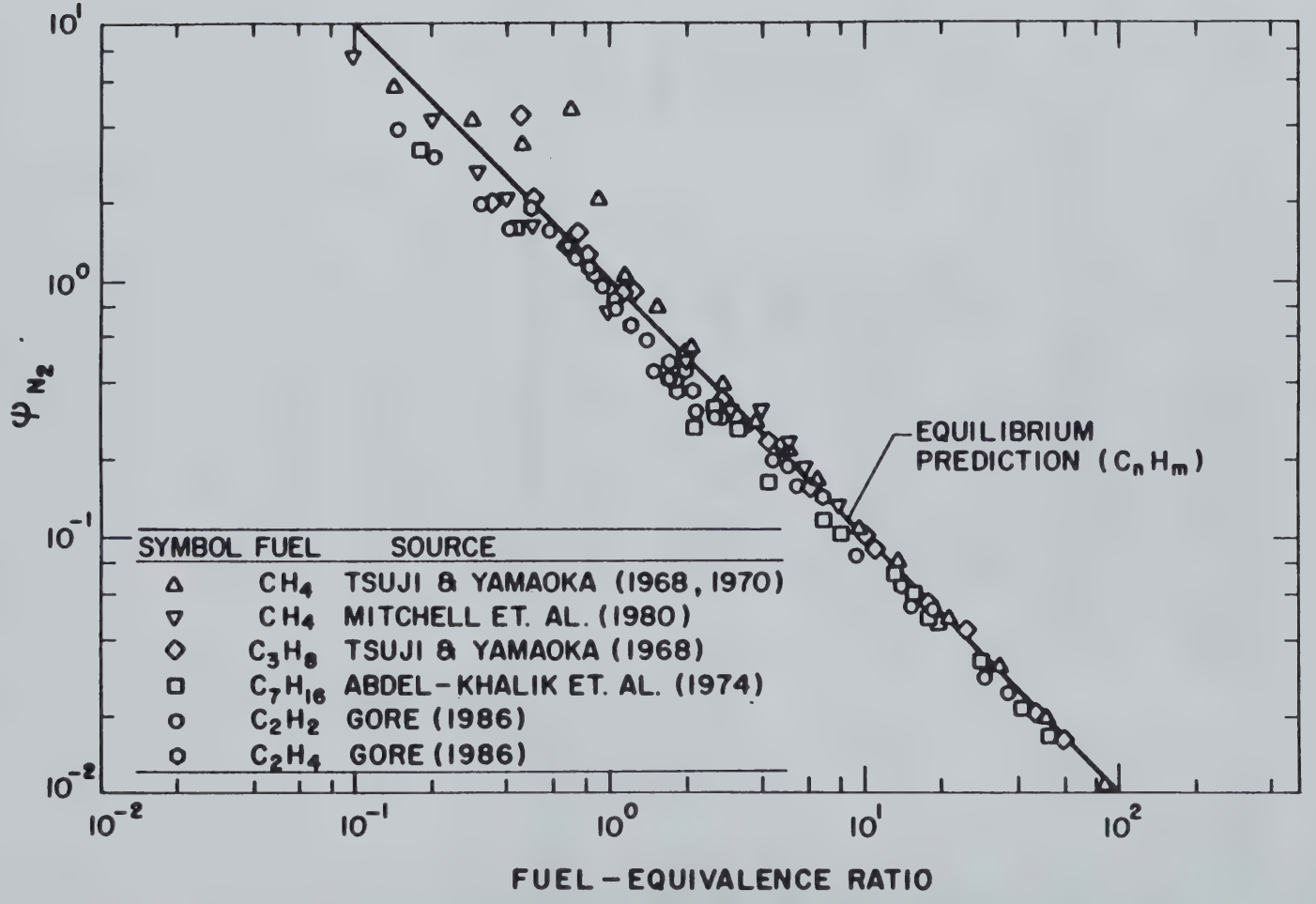

Figure 1 State relationship for nitrogen concentrations in hydrocarbon/air diffusion flames.

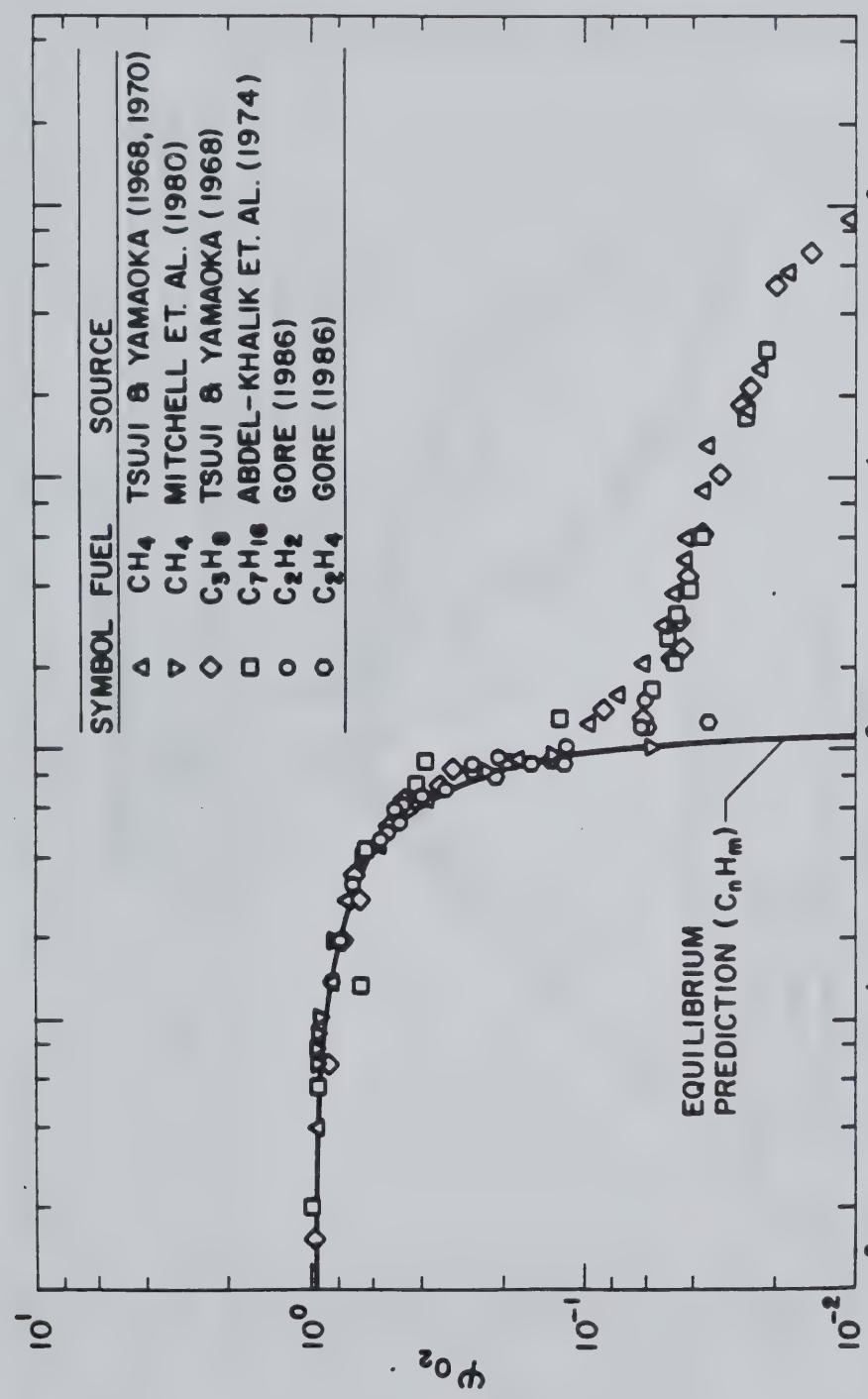

Figure 2 State relationship for oxygen concentrations in hydrocarbon/air diffusion flames.

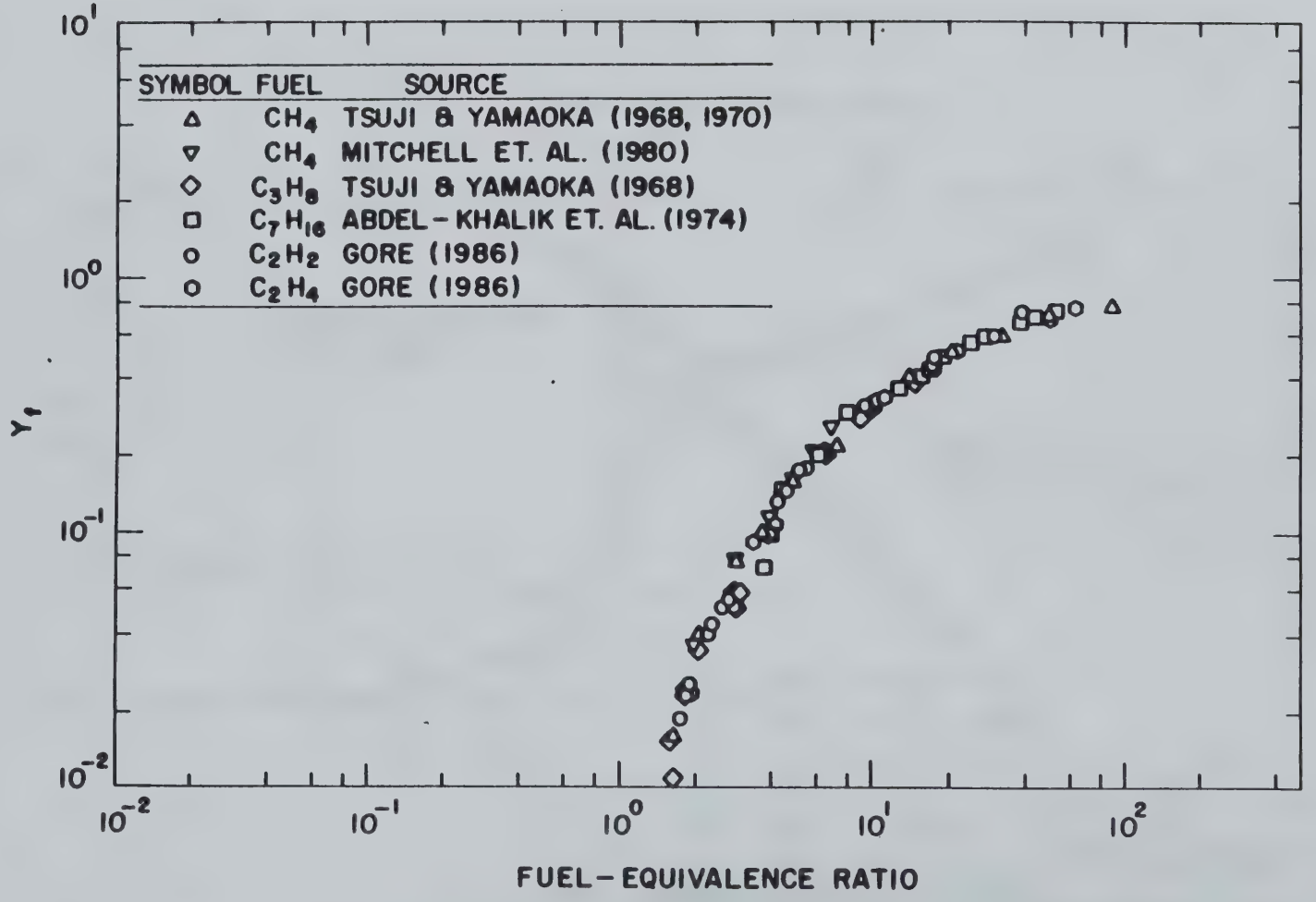

Figure 3 State relationship for fuel concentrations in hydrocarbon/air diffusion flames.

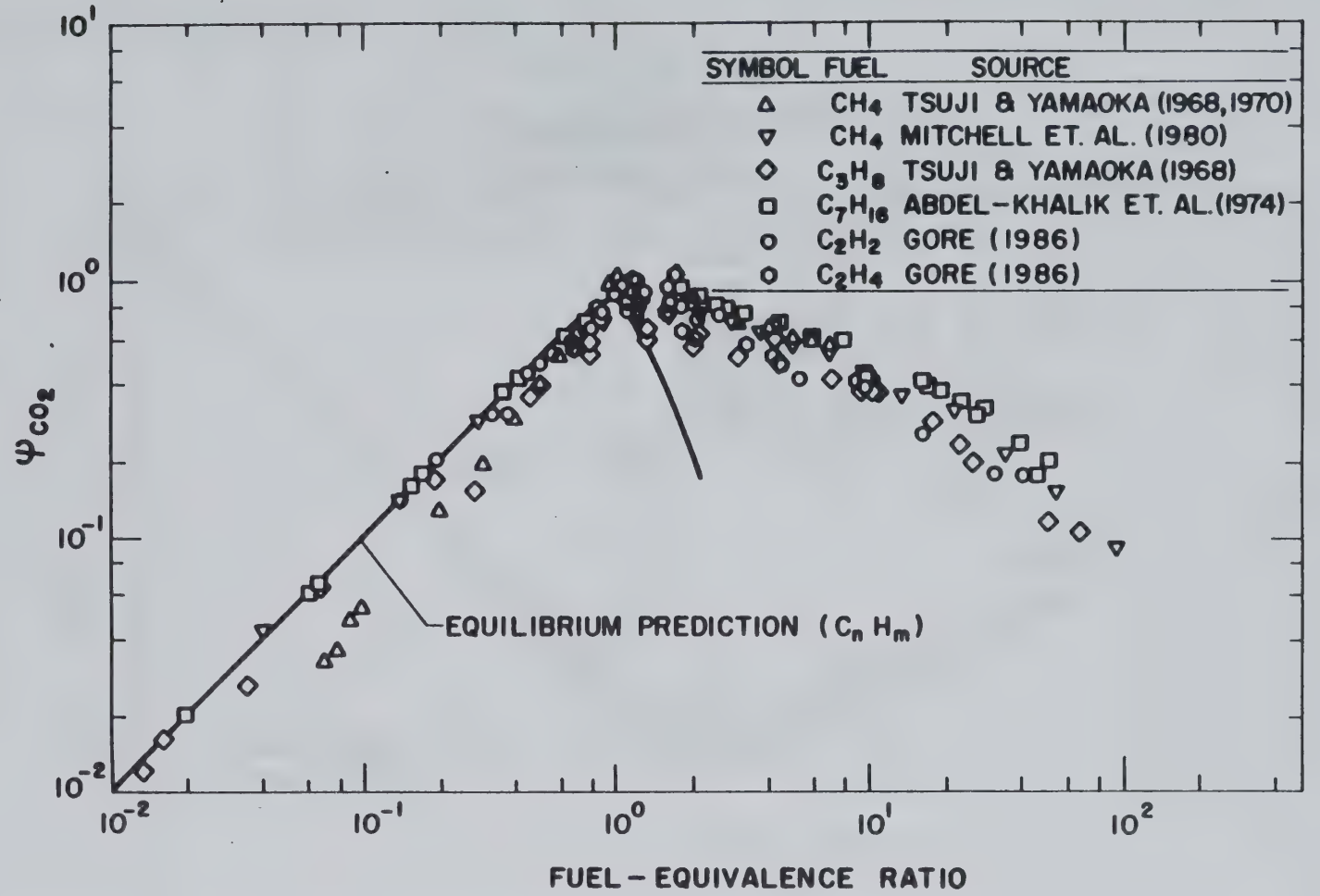

Figure 4 State relationship for carbon dioxide concentrations in hydrocarbon/air diffusion flames.

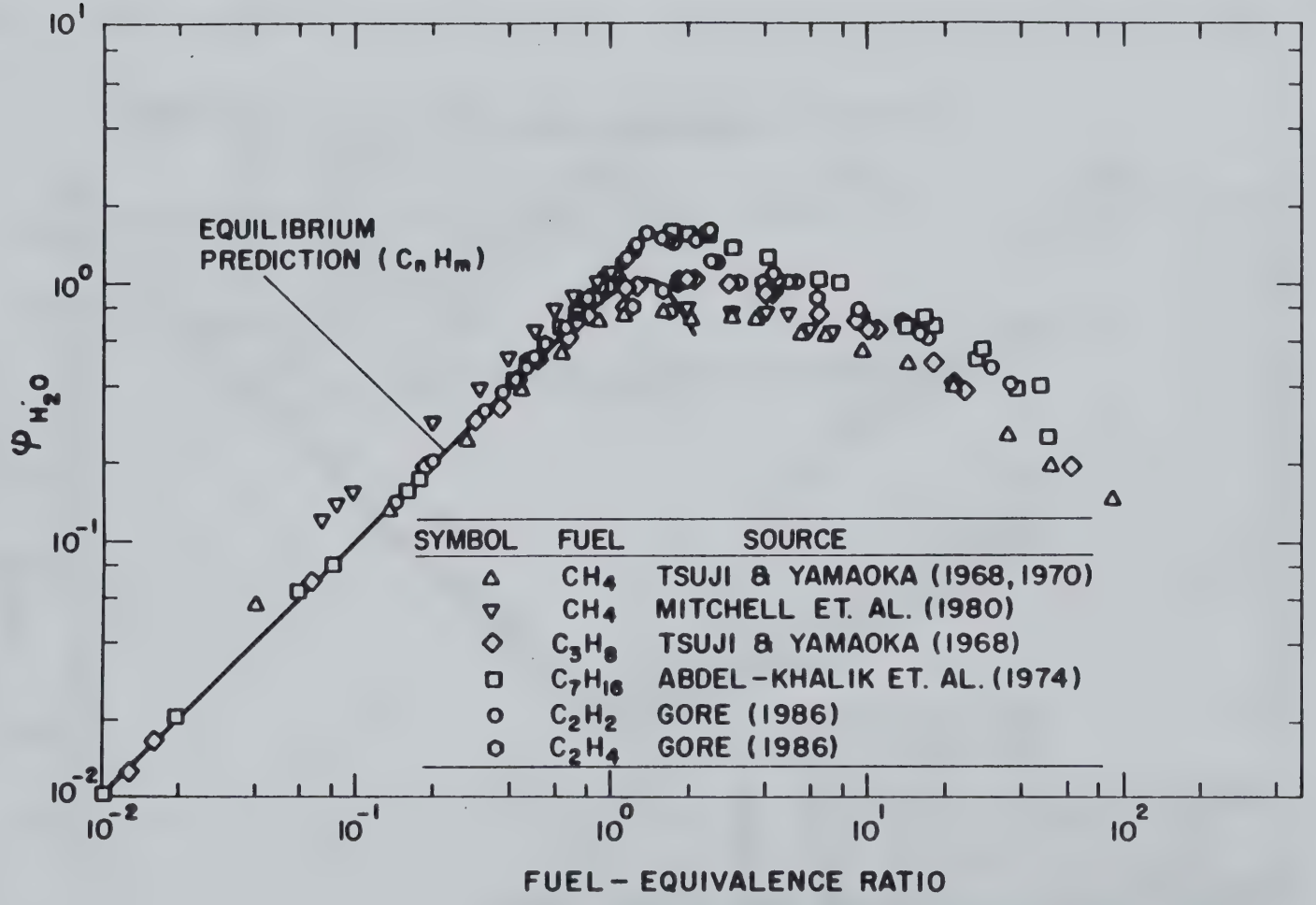

Figure 5 State relationship for water vapor concentrations in hydrocarbon/air diffusion flames.

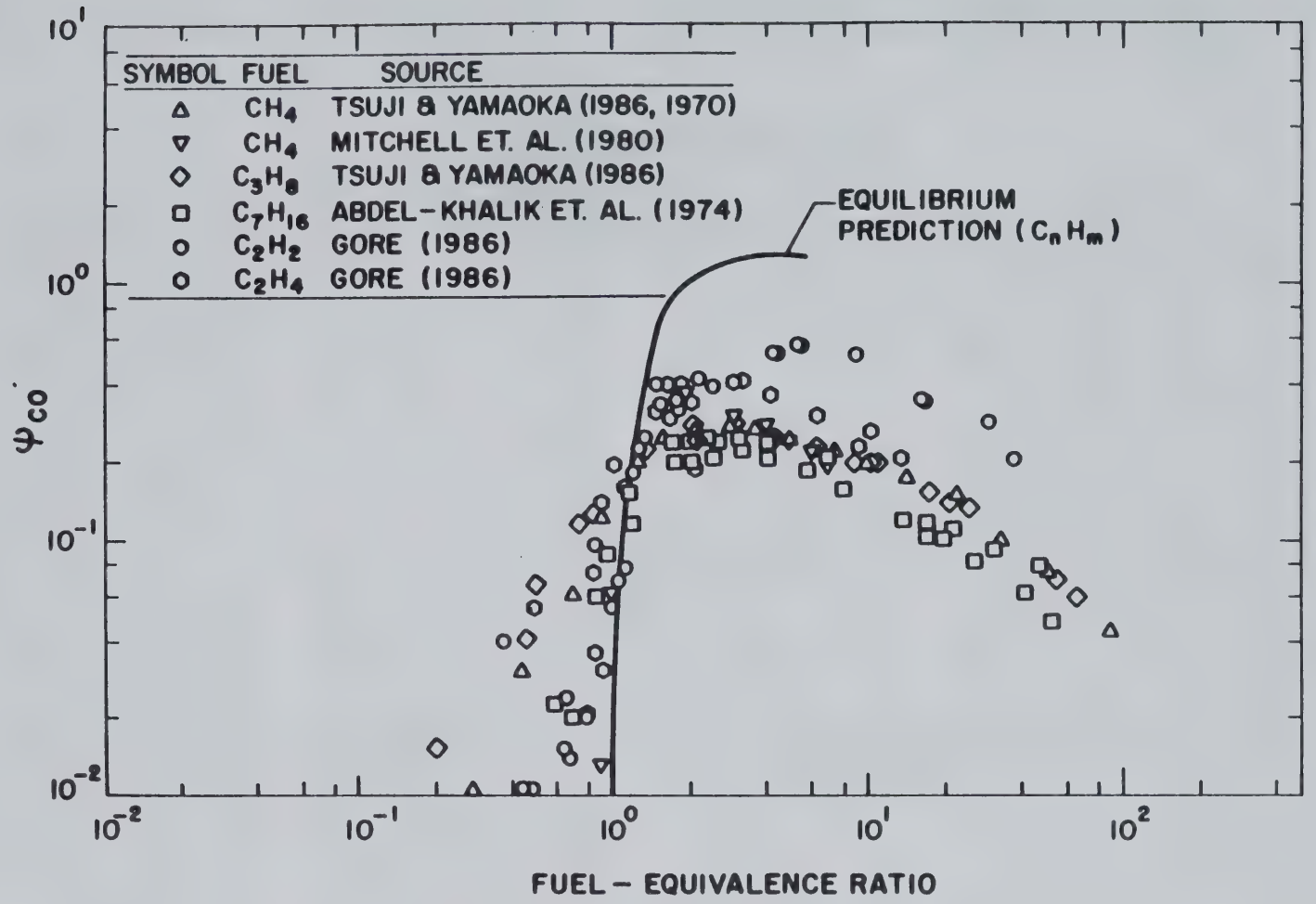

Figure 6 State relationship for carbon monoxide concentrations in hydrocarbon/air diffusion flames.

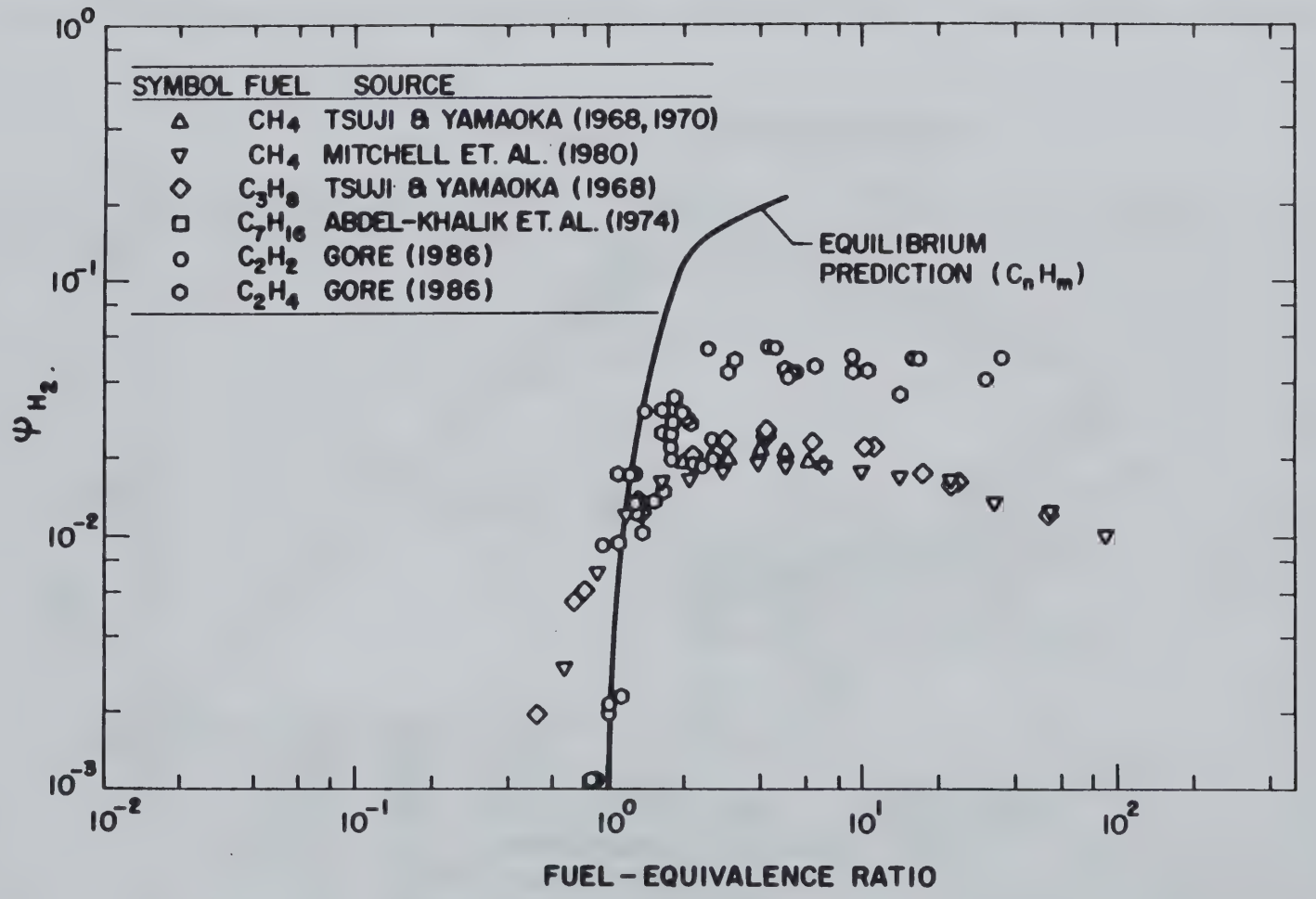

Figure 7 State relationship for hydrogen concentrations in hydrocarbon/air diffusion flames.

The generalized state relationship for the mass fraction of oxygen appears in Fig. 2. For low values of the fuel-equivalence ratio, $\phi \leq 0.8$, both the measurements and the equilibrium prediction are in reasonably good agreement with the mixing-controlled expression of equation (6). In the region $0.8 \leq \phi \leq 1$, the measurements continue to follow the equilibrium predictions reasonably well. For $\phi > 1$, the measurements depart from equilibrium, however, the departure is largely universal for the present data base. Mitchell et al. (1980a) were concerned that the oxygen that they observed for fuel-rich conditions was due to the leakage of air across the burner lip and below the point of flame attachment for their coflowing jet flames. However, the results illustrated in Fig. 2 indicate essentially no difference between measurements for coflowing jets and porous cylinders in crossflow (where air leakage cannot be a factor). A more likely explanation is that oxygen concentrations are never zero at the stoichiometric condition due to dissociation, which allows oxygen to diffuse toward fuel-rich conditions. Non-equilibrium processes in the near fuel-rich region maintain oxygen concentrations near stoichiometric conditions until ϕ reaches values of ca. 2; at higher fuel-equivalence ratios, gas temperatures drop below 1000 K so that rates of chemical reaction are small and oxygen simply diffuses (mixes) like a passive scalar in this region. Throughout the fuel-rich region, however, the concentrations of oxygen are never large, e.g., mass fractions are generally less than 1%.

The generalized state relationship for the mass fraction of fuel appears in Fig. 3. Only measurements are available in this case, however, they exhibit a remarkable degree of universality. This can be explained by noting that the fuel mass fraction must approach unity as a boundary condition for large values of ϕ, while the mixture supports little chemical reaction until ϕ reaches values of ca. 2. Even taking the point of disappearance of the fuel to be anywhere in the range ϕ = 1-2, would result in a reasonable state relationship correlation for the mass fraction of fuel, based on these considerations. The correlation is improved from this limit since the rapid increase in temperature as ϕ drops below 2 causes the fuel to disappear within a relatively narrow range of ϕ, e.g., $\phi \approx 1.5$.

The generalized state relationship for the mass fraction of carbon dioxide appears in Fig. 4. Throughout most of the fuel-lean region, $\phi \leq 0.9$, both the measurements and the equilibrium prediction are in reasonably good agreement with the mixing-controlled expression of equation (7). The mean value of the measurements continues to follow the equilibrium prediction up to ϕ = 1; however, the data departs from the equilibrium prediction for fuel-rich conditions similar to oxygen. This involves reaction processes which tend to keep Y_{CO_2} near its stoichiometric value for ϕ in the range 1-2, followed by passive mixing in the low temperature gas mixture at higher fuel-equivalence ratios. The scatter of the measurements is consistent with experimental uncertainties everywhere; in particular, the larger scatter for $\phi < 10^{-1}$ simply reflects larger experimental uncertainties as the concentration of carbon dioxide becomes small.

The generalized state relationship for the mass fraction of water vapor appears in Fig. 5. These results are generally similar to the findings for carbon dioxide. Throughout the fuel-lean region, $\phi \leq 1$, both the measurements and the equilibrium prediction are in reasonably good agreement with the mixing-controlled expression of equation (8). The scatter of the measurements in the near fuel-rich region ($1 \leq \phi \leq 4$), however, is greater for water vapor than for carbon dioxide. This is probably due to increased errors in estimating the mass fraction of water vapor from measurements made on a dry basis. In particular, the measurements of Abdel-Khalik et al. (1974) are somewhat higher than the rest: this is undoubtedly due to assigning all excess hydrogen from the fuel to water vapor since hydrogen concentrations were not measured for this data set, e.g., results plotted in Fig. 7 show that hydrogen concentrations are relatively high in this region. In contrast, the results of Mitchell et al. (1980b) and a portion of the results of Tsuji and Yamaoka (1970), where water vapor concentrations were measured directly, are in reasonably good agreement with

each other and are felt to be the most reliable. These findings follow equilibrium predictions for ϕ up to ca. 1.2 and then remain relatively constant until the passive diffusion (mixing) region is reached for $\phi > 2$.

The generalized state relationships for the mass fractions of carbon monoxide and hydrogen are illustrated in Figs. 6 and 7. The concentrations of CO and H_2 are generally smaller than CO_2 and H_2O so that experimental uncertainties are somewhat larger causing greater scatter of the data—particularly for hydrogen. Effects of finite-rate chemistry are also more significant since measurements for these species do not follow trends of equilibrium predictions anywhere—but simply cross them near stoichiometric conditions. Large concentrations of soot may also affect the correlations for fuel-rich conditions. In particular, C_2H_2 and C_2H_4/air flames have large soot concentrations in a soot spike present for fuel equivalence ratios greater than unity reaching maximum soot volume fractions of 20 and 2 ppm, respectively (Gore, 1986; Gore and Faeth 1986, 1987); notably, they also exhibit higher concentrations of CO and H_2 than the other fuels in the same region. Both species exhibit behavior consistent with passive mixing for $\phi > 4$ where temperatures become low; however, concentrations of H_2 decay slower than other species which suggests a possible effect of differential diffusion since H_2 has the highest mass diffusivity of all the species considered. For fuel-lean conditions, the concentration of both species becomes small for $\phi < 0.4$, where gas temperatures are generally less than 1000 K.

Discussion. The generalized state relationships for N_2, O_2, fuel, CO_2 and H_2O mass fractions are reasonably satisfactory; particularly in view of the large H/C variation of the fuels, the wide range of burner conditions, and the experimental uncertainties of the measurements within the data base. The generalized state relationships for the mass fractions of CO and H_2 are less satisfactory. This can be attributed partly to higher experimental uncertainties since the concentrations of these species are generally smaller than the rest. However, the presence of these species for fuel-lean conditions is not in accord with equilibrium predictions that are generally satisfactory for fuel-lean conditions for the other species. Furthermore, concentrations of these species differ somewhat for fuels having high soot concentrations for fuel-rich conditions. Thus, finite rate or differential diffusion effects are probably responsible for less universality of the state relationships for CO and H_2 than for the other major gas species.

In spite of the deficiencies for CO and H_2, however, the generalized state relationships should still be useful—particularly for turbulent flames where the alternative is a full treatment of finite-rate chemistry in a turbulent environment. In particular, N_2, O_2, fuel, CO_2 and H_2O comprise the bulk of the mixture for hydrocarbon/air diffusion flames so that mixture molecular weights can be found for density computations with reasonable accuracy; while CO_2 and H_2O are the main species contributing to gas-band radiation in the infrared that must be found to estimate flame radiation. Naturally, finding densities and radiation properties also requires the mixture temperature which has not been considered during the present investigation. A provisional approach for estimating mixture temperatures as a function of fuel equivalence ratio, based on a knowledge of the concentrations of major gas species and the radiative heat loss fraction of the flame, has been reported during earlier work in this laboratory (Jeng and Faeth, 1984a,b; Gore and Faeth, 1986, 1987; Sivathanu et al., 1988); however, generalized methods to find mixture temperatures clearly deserve further study.

The generalized state relationships of Figs. 1-7 are limited to conditions that are not too near points of flame extinction and attachment. Similarly, tests of the performance of the state relationships for particular fuel/air diffusion flames have been limited to the buoyant jet flames listed in Table 1; therefore, present results are most appropriate for natural fires where local mass transport rates are generally relatively small. Nevertheless,

the concentrations of major gas species remain relatively constant as extinction conditions are approached (Tsuji and Yamaoka 1968, 1970; Liew et al. 1981, 1984) so that the results may prove to be useful for high-intensity combustors as well. This possibility also merits study.

Compromises have been made to obtain generalized state relationships for fuels having a range of H/C ratios; therefore, state relationships for the individual fuels are generally superior to the present results and should be used whenever possible. Similarly, a number of minor species, particularly fuel decomposition products, exhibit reasonably good state relationships for particular fuel/air diffusion flames (Bilger, 1977; Mitchell et al.,1980a,b; Gore 1986; Gore and Faeth 1986, 1987; Gore et al. 1986). However, including these substances in the present generalized approach is not feasible since the fuel in one case (with behavior illustrated in Fig. 3) may be an intermediate with very different behavior in another.

Finally, the data base used to develop the generalized state relationships was limited to the alkane and alkene fuels listed in Table 1. Evaluation of the concept for a broader range of hydrocarbons, particularly including more liquid and solid fuels, would be desirable as well.

2.5 Conclusions

Generalized state relationships for the mass fractions of major gas species were studied using existing measurements for laminar C_nH_m/air diffusion flames. The correlations included molar H/C ratios in the range 1-4 and fuel-equivalence ratios in the range 10^{-2}-10^{2}. The main conclusions of the study are as follows:

1. Reasonably satisfactory generalized state relationships were found for the mass fractions of N_2, O_2, fuel, CO_2 and H_2O. These correlations approximated thermodynamic equilibrium predictions for fuel-lean conditions and departed from equilibrium in a relatively universal manner for fuel-rich conditions.

2. Generalized state relationships were also found for CO and H_2; however, these correlations exhibited greater scatter than the other species. Similarly, these species only approached equilibrium predictions near the stoichiometric condition with somewhat scattered departure from equilibrium for both fuel-lean and fuel-rich conditions.

3. The rationale for the existence of generalized state relationships for major gas species is that lean conditions approximate thermodynamic equilibrium and are largely governed by the mixing of saturated combustion products with ambient air since effects of dissociation are modest even near the stoichiometric condition for hydrocarbon/air diffusion flames; additionally, fuel-rich conditions ($\phi > 2$) largely involves passive mixing toward a pure fuel condition at large fuel-equivalence ratios. Fortuitously, species concentrations in the intermediate region ($1 < \phi < 2$) either are controlled by passive mixing (N_2) or are relatively constant so that mixing behavior is similar for various H/C ratios at both large and small fuel-equivalence ratios. The reasons for the fortuitous behavior at intermediate values of ϕ, often in the presence of large soot concentrations, are not known and certainly deserve additional study.

3. TEMPERATURE/SOOT VOLUME FRACTION CORRELATIONS IN TURBULENT LUMINOUS FLAMES

3.1 Introduction

Continuum radiation from soot is an important aspect of hydrocarbon-fueled fires since it influences their spread rates, burning rates and structure (deRis, 1978; Faeth et al., 1988a). The geometrical feature of soot that affects radiation is the soot volume fraction, rather than particle size and shape distributions, since the Rayleigh limit for small particles is generally acceptable for estimating the spectral absorption coefficients of soot and scattering can be ignored (Tien and Lee, 1982). Prompted by this observation, measurements of soot volume fractions and other scalar properties relevant to radiation were recently completed in this laboratory for the fuel-lean (overfire) region of buoyant turbulent diffusion flames (Sivathanu et al., 1988; Sivathanu and Faeth, 1989a). The objective of this portion of the investigation was to extend this work to the fuel-rich (underfire) region of similar flames. The study was limited to highly-buoyant, pool-like, turbulent fires burning in still air; therefore, the findings are primarily relevant to natural (unwanted) fires. The test fuels included acetylene, propylene, ethylene and propane—all of which yield flames having significant levels of continuum radiation from soot.

The present study also extended earlier efforts to evaluate the laminar flamelet concept for soot volume fractions in diffusion flames. This concept has been proposed for use in conjunction with the conserved-scalar formalism, as a means of avoiding the complexities of soot chemistry in turbulent environments when estimating the continuum radiation properties of turbulent flames (Gore and Faeth, 1986, 1988). The key hypothesis of the laminar flamelet concept for diffusion flames is that instantaneous scalar properties are only functions of the instantaneous mixture fraction (called state relationships). The concept was initially proposed by Bilger (1977); furthermore, a number of subsequent studies have found satisfactory state relationships for major gas species, even for flames with large concentrations of soot, except near points of flame attachment or extinction as noted in Section 2.

The existence of state relationships for major gas species prompted earlier studies in this laboratory to see whether soot volume fractions behaved in the same manner (Sivathanu et al., 1988; Sivathanu and Faeth, 1989a; Gore and Faeth, 1986, 1987). The status of this work can be conveniently summarized by the plots of soot volume fractions as a function of mixture fraction for acetylene and ethylene/air diffusion flames illustrated in Fig. 8. Measurements shown in the figure were obtained for a variety of burners, flame operating conditions, and positions within the flames—see original citations for the details. These factors are not designated on the plots to avoid cluttering; however, to the extent that the laminar flamelet concept for soot volume fractions is correct, soot volume fraction should be only a function of mixture fraction.

Past studies of soot volume fraction state relationships for fuel-rich conditions have been limited to laminar acetylene and ethylene flames burning in still air (Gore and Faeth, 1986, 1987). The results plotted in Fig. 8 show that soot volume fractions are appreciable only for relatively narrow ranges of mixture fractions (called soot spikes) for fuel-rich conditions. The state relationship correlations for the soot spikes are poorer than for major gas species; nevertheless, estimates of the radiation properties based on these correlations were still reasonably good, suggesting that some dispersion of soot volume fraction state relationships can be tolerated for radiation predictions (Gore and Faeth, 1986, 1987).

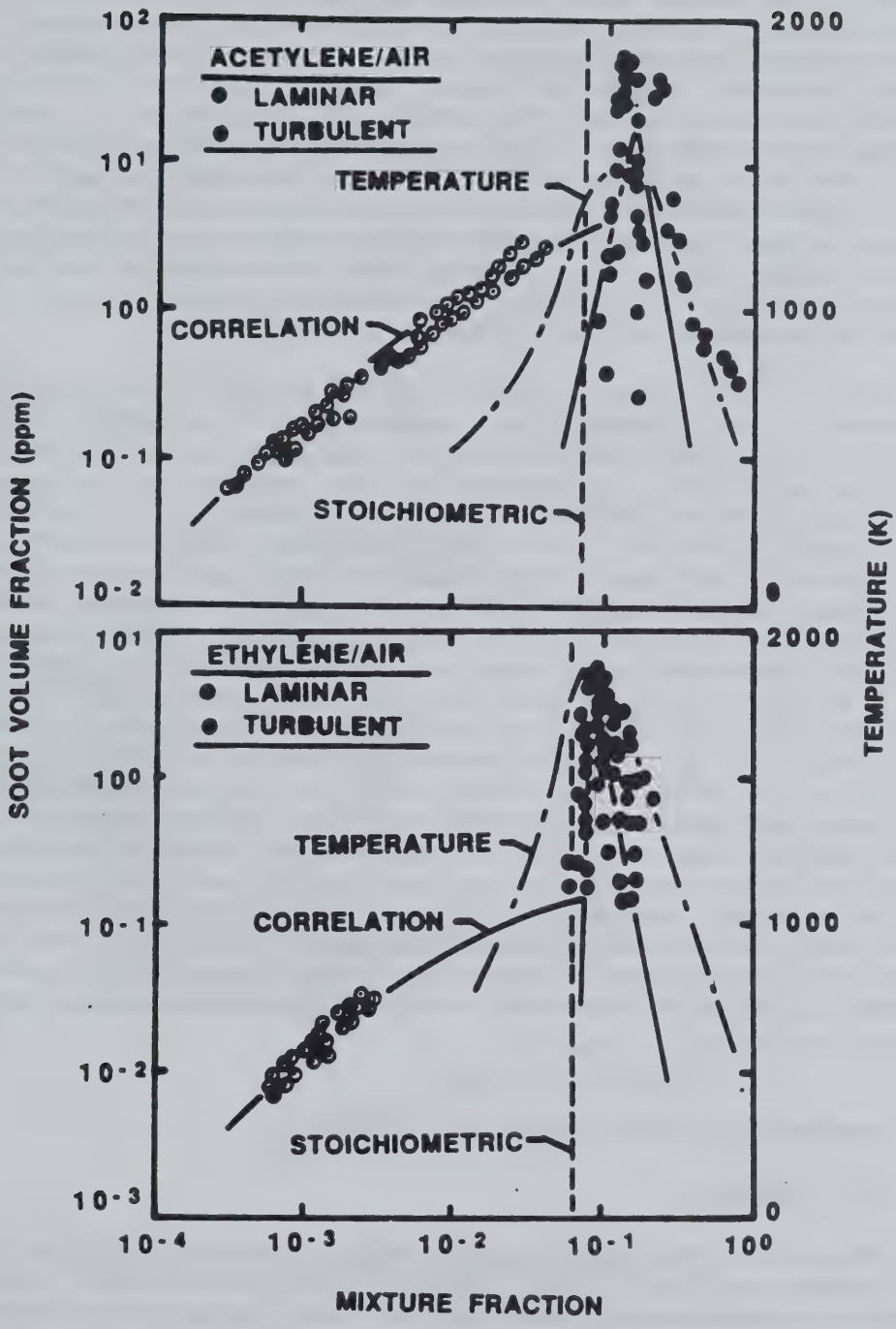

Figure 8 Soot volume fraction state relationships for acetylene/air and ethylene/air diffusion flames. Data and correlations from Sivathanu et al. (1988), Sivathanu and Faeth (1989a) and Gore and Faeth (1986, 1987).

Past studies of soot volume fraction state relationships for lean conditions involved the overfire region of sooting turbulent flames (Sivathanu et al., 1988; Sivathanu and Faeth, 1989a). It was found that soot generation efficiencies (the percentage of fuel carbon that is converted to soot and emitted from the flame) were constant throughout the overfire region for a given fuel and burner operating condition. Furthermore, soot generation efficiencies increased with flame residence time at first but then became constant for times longer than roughly ten times the residence time at the laminar smoke point. Since soot densities in the overfire region are relatively independent of fuel type and operating conditions (Newman and Steciak (1987), while carbon from the fuel is a passive scalar proportional to mixture fraction, this implies a universal state relationship for soot volume fractions in the overfire region at long residence times. The results illustrated in Fig. 8 for fuel-lean conditions were obtained within the long residence time regime: the measurements for various operating conditions and positions in the overfire region are seen to be only a function of mixture fraction and correlate quite well with expressions based on constant soot generation efficiencies and density for acetylene and ethylene. Similar results for propylene and propane can be found in Sivathanu and Faeth (1989a).

Based on these findings, the main issues are whether the properties of the soot spike observed in laminar flames are similar within turbulent flames; and when, if at all, the soot volume fraction state relationship concept is appropriate for the fuel-rich (underfire) region of turbulent flames. A formal test of these properties requires simultaneous measurements of soot volume fraction and mixture fraction at a point, with sufficient temporal resolution to control effects of gradient broadening. This is difficult to achieve in turbulent flames: the soot spike involves a relatively small range of mixture fractions (see Fig. 8), imposing stringent accuracy requirements in a difficult environment; while existing methods for rapidly measuring mixture fractions in turbulent environments either lose sensitivity in the presence of soot or might interfere with soot chemistry. Thus, an indirect approach was used instead, simultaneously measuring soot volume fractions and temperatures with an optical probe and inferring whether these findings were consistent with the existence of the soot spikes observed for fuel-rich conditions in Fig. 8. An auxiliary benefit of this approach is that it directly provides soot volume fractions and temperatures—the two main scalar properties affecting continuum radiation from soot-containing flames. Measurements were limited to relatively large flames within the long residence time regime with respect to soot generation efficiencies in the overfire region. This helped to minimize problems of spatial resolution while providing a test of whether long residence time behavior in the overfire region would extend to the fuel-rich (underfire) region as well. The measurements involved both probability density functions (PDFs) of temperature, conditioned on soot volume fraction; and the correlation between temperatures and soot volume fractions.

3.2 Experimental Results

3.2.1 Apparatus

The apparatus was similar to the arrangement used earlier for studies of the overfire region (Sivathanu and Faeth, 1989a). A sketch of the apparatus appears in Fig. 9. The arrangement involved vertically-upward injection of fuel in still air with the flames attached at the burner exit. The flames burned within a large enclosure (2.4 × 2.4 × 3.6 m high) with a metal hood and adjustable exhaust system at the top to remove the combustion products. Room disturbances were reduced by using strips of plastic film as the side walls of the enclosure, as well as a smaller screened enclosure (1 × 1 × 2 m high) directly around the flames. The optical probe was mounted rigidly; therefore, the flame was traversed to provide measurements at various points within the underfire region.

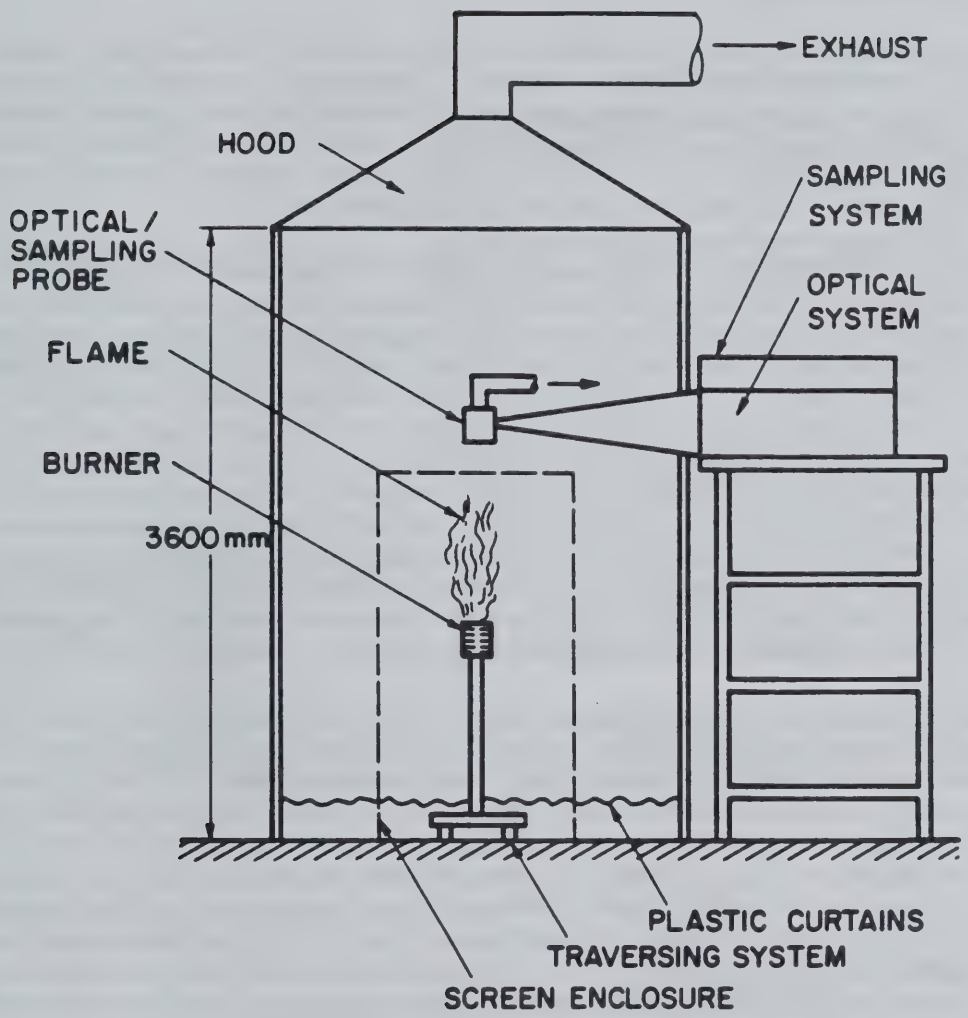

Figure 9 Sketch of the luminous flame apparatus.

A sketch of the burner appears in Fig. 10. The burner exit was 50 mm in diameter. The fuel entered the bottom of the burner and then passed through a honeycomb section (3 mm cell size × 40 mm long) to remove any residual swirl. The flow subsequently passed through two more plenum sections and two beds of steel balls (5 and 3 mm in diameter with bed heights of 25 mm) to provide a uniform flow at the burner exit. The burner was cooled by water flowing through a coil soldered to its outside surface. The flames attached naturally at the exit of the burner.

3.2.2 Instrumentation

Optical Probe. The optical probe involved laser extinction to measure soot volume fractions and two-wavelength pyrometry to measure temperatures. The probe is illustrated in Fig. 11: it consisted of two light guides, mounted opposite one another, tapered to open view ports (3 mm in diameter) at their tips. The light guides were purged with a 1 cc/s flow of nitrogen which passed out of the open viewing ports; however, increasing the nitrogen flow rate up to 3 cc/s had little effect on the measurements.

Choosing the optical path length was a compromise between reducing effects of gradient broadening by minimizing the length, and improving signal-to-noise ratios and reducing disturbances of the flow by the probe by increasing the length. Based on these considerations, the distance between viewing ports was 10 mm for the acetylene flames and 20 mm for the other flames. The larger path length for the more weakly-sooting fuels helped extend the dynamic range of the soot volume fraction measurements. Minimum integral-scale lengths were estimated to be roughly 20 mm for the range of the measurements so the longer path length was marginal; however, varying path lengths in the range 10-30 mm had little effect (less than 30 K) on the temperature measurements and observations of maximum soot volume fractions. It will also be seen that the general behavior of the soot volume fraction and temperature measurements was similar for acetylene and the other fuels, in spite of the 2:1 increase of optical path length, suggesting that gradient broadening did not influence the major conclusions of the study excessively.

Soot Volume Fractions. Soot volume fractions were measured by laser extinction across the gap between the viewing ports, using the 632.8 nm line of a HeNe laser (15 mW, Spectra Physics Model 124B, having a 1.1 mm diameter beam at the e^{-2} points). Two detectors (Newport Model 982 Laser Power Meters) were used to measure the intensity of the laser beam before and after passing through the flame, in order to compensate for variations of laser power. The detector for transmitted radiation had a large active area (100 mm^2) and a response within 99% at ± 3 mm from the axis with an angular misalignment of ± 2°; therefore, effects of beam steering due to refractive index variations in the optical path were small. Laser line filters (10 nm bandwidth), a chopper operating at 1500 Hz, a carrier amplifier system, and a 600 Hz fourth-order low-pass filter were used to reduce effects of background radiation and to improve signal-to-noise ratios.

Soot volume fractions were found assuming the Rayleigh limit for small particles since past multiline laser-extinction measurements for acetylene and ethylene flames suggested $\pi d_p/\lambda < 0.5$ at a wavelength of 632.8 nm (Gore and Faeth, 1986, 1987; Flower, 1988; Flower and Bowman, 1986). For such conditions, the differences between Rayleigh- and Mie-scattering predictions of soot volume fractions are less than 15% (Santoro et al., 1984). The relationship between the extinction ratio of the laser beam and the soot volume fraction for the Rayleigh limit is as follows (Tien and Lee, 1982):

$$f_v = - \ln (i_\lambda/i_{\lambda o})/(f_\lambda L) \qquad (12)$$

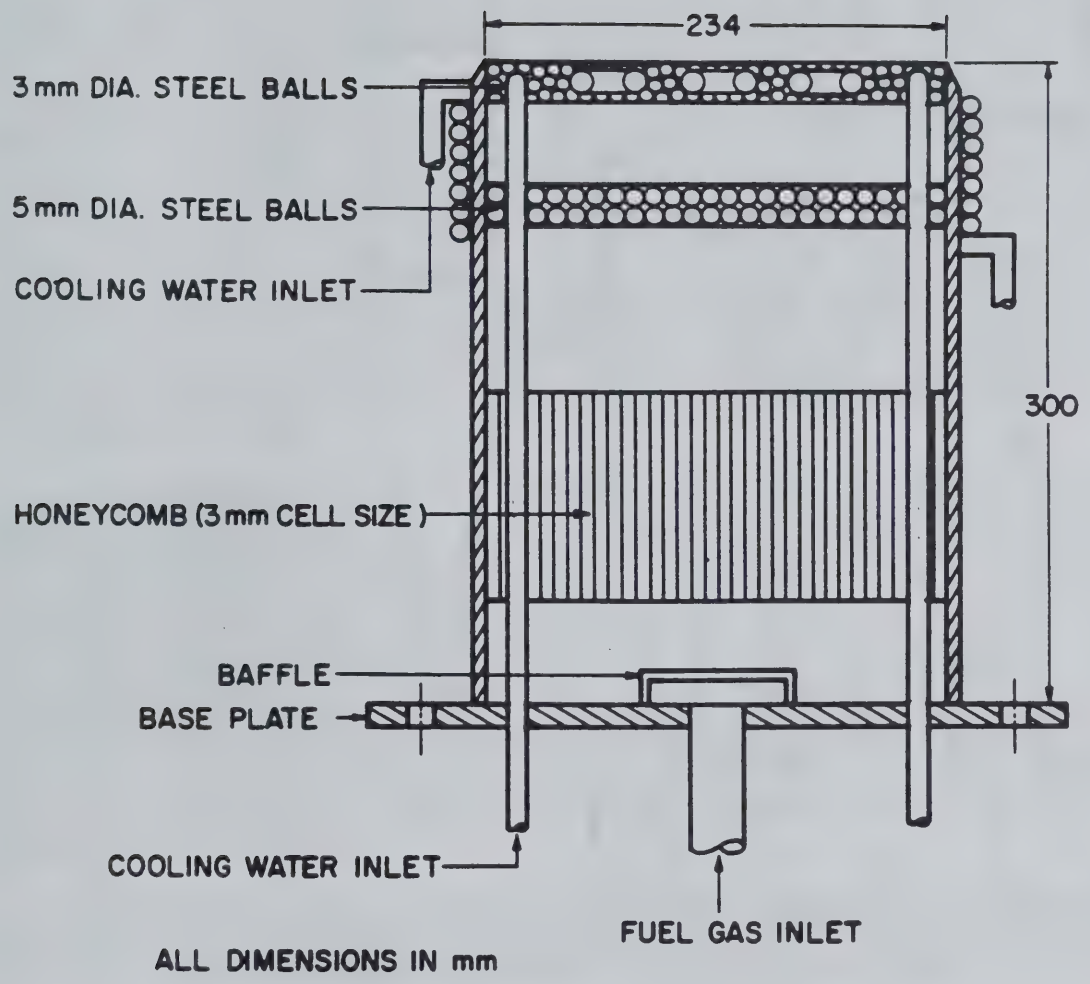

Figure 10 Sketch of the 50 mm diameter burner.

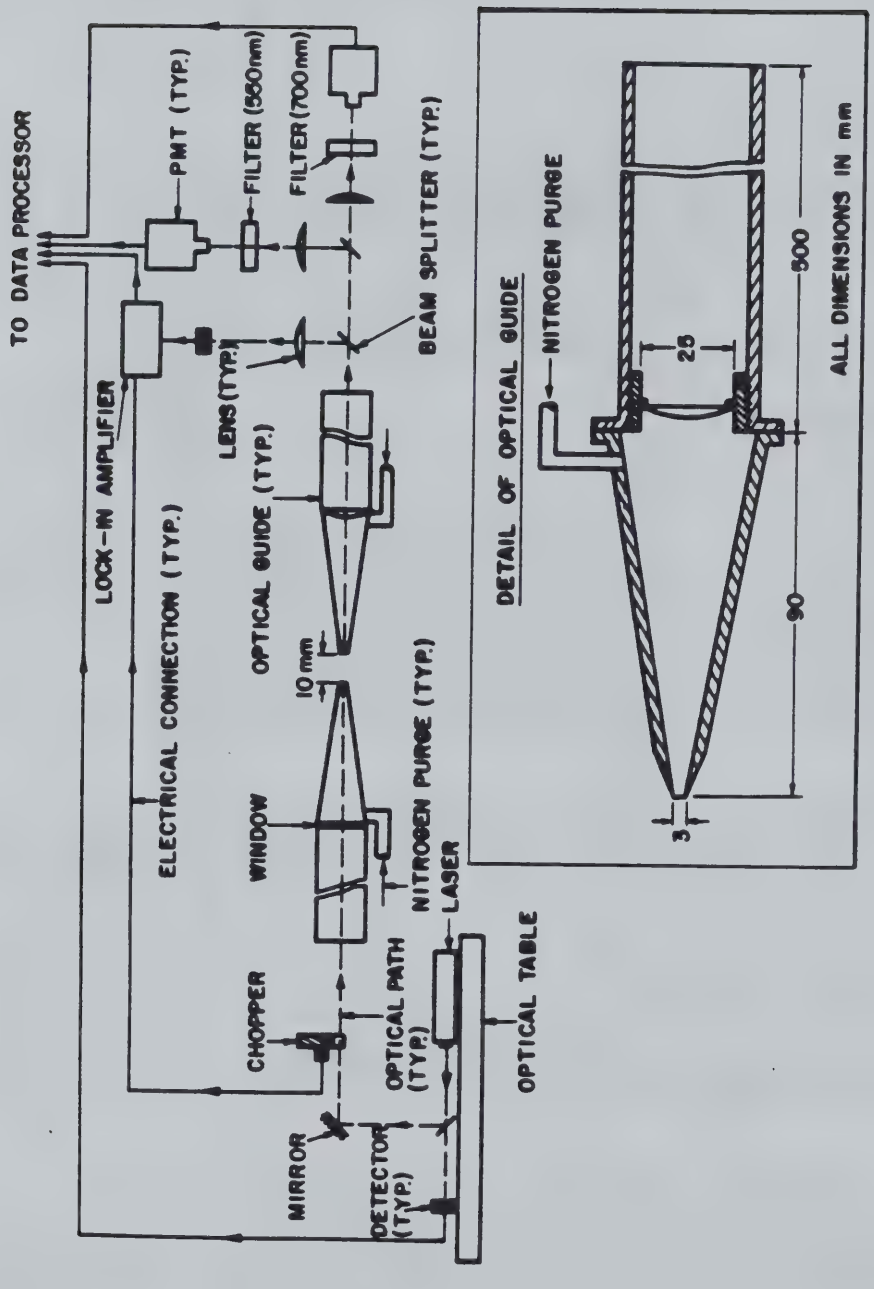

Figure 11 Sketch of the underfire optical probe.

The parameter f_λ in equation (12) is a function of wavelength and the real and imaginary parts of the refractive indices of soot, n - iκ, as follows:

$$f_\lambda = (36\pi n\kappa/\lambda) / ((n^2 - \kappa^2 + 2)^2 + (2n\kappa)^2) \qquad (13)$$

The selection of soot refractive indices introduces uncertainties in the computation of soot volume fractions for fuel-rich conditions within diffusion flames. Tien and Lee (1982) and Dalzell and Sarofim (1969) find that soot refractive indices for hydrocarbon diffusion flames are relatively independent of fuel type (for H/C ratios spanning the present fuels) and temperature. In contrast, a recent measurement for a kerosene diffusion flame by Batten (1985) is not in good agreement with these results, with effects of fuel H/C ratio cited as the potential source of the discrepancy. Furthermore, several recent measurements of soot refractive indices in premixed hydrocarbon flames have found effects of fuel type, fuel-equivalence ratio, and residence time in the post-flame region (Charalampopoulos and Felske, 1987; Charalampopoulos and Chang, 1988; Habib and Vervisch, 1988). The latter observations are problematical since conditions within the soot spike at fuel-rich conditions for diffusion flames are similar to conditions in the post-flame region of fuel-rich premixed flames, while residence times at these conditions are relatively long for the present experiments. Nevertheless, the majority of the results for the post-flame region of premixed flames are comparable to the findings of Dalzell and Sarofim (1969), 1.55-0.56 i at 632.8 nm; therefore, these values were used in order to be consistent with earlier work in this laboratory (Gore and Faeth, 1986, 1987; Sivathanu et al., 1988; Sivathanu and Faeth, 1989a) and elsewhere (Flower, 1988; Flower and Bowman, 1986; Megaridis and Dobbins, 1988; Santoro et al., 1984).

Two-Wavelength Pyrometry. Two-wavelength pyrometry was used to find temperatures along the optical path. This involved measurements of emission at 700 nm (always) and either 550 or 800 nm, using methods described by Cashdollar (1979) and Klingenberg (1985). These wavelengths only involve continuum radiation from soot and yield soot temperatures, however, gas temperatures are essentially the same since soot particles are small. The optical path was observed from one of the viewing ports while the other viewing port served as a cold boundary to limit the length of the optical path. The emission signal was focussed through two beam splitters to impinge on two detectors (Hamamatsu photomultiplier tubes, model R316) while passing through appropriate line filters (10 nm halfwidth). The output signals were split, with one portion being amplified 100:1 while the other portion went directly to the a/d converter, in order to increase the dynamic range of the instrument.

Assuming homogeneous conditions along the optical path, and negligible radiation from the cold background, Planck's Law gives the following expression for the voltage output of the detector at wavelength λ (Cashdollar, 1979; Klingenberg, 1985):

$$V_\lambda = A\, b_\lambda\, \varepsilon_\lambda\, (2\pi hc^2/\lambda^5) / (\exp(hc/\lambda\, kT) - 1) \qquad (14)$$

where A and b_λ are the wavelength-independent and wavelength-dependent proportionality factors of the instrument. For present conditions, the exponential term in equation (14) is >> 1; therefore, T can be found from measurements of V_λ at two wavelengths, as follows:

$$T = \frac{hc}{k}\left(\frac{1}{\lambda_1} - \frac{1}{\lambda_2}\right) / \ln\left\{\left(\frac{\varepsilon_{\lambda 1}}{\varepsilon_{\lambda 2}}\right)\left(\frac{b_{\lambda 1}}{b_{\lambda 2}}\right)\left(\frac{V_{\lambda 1}}{V_{\lambda 2}}\right)\left(\frac{\lambda_2}{\lambda_1}\right)^5\right\} \qquad (15)$$

The ratio of the $\varepsilon_{\lambda i}$ was obtained from the laser extinction measurements of f_v, as follows:

$$\varepsilon_{\lambda i} = 1 - \exp(- f_v L f_{\lambda i}) \tag{16}$$

There is little change in the refractive indices of soot over the wavelength range 550-800 K (Tien and Lee, 1982; Dalzell and Sarofim, 1969); therefore, $f_{\lambda i}$ in equation (16) was computed from equation (13) using the same values as the soot volume fraction measurements.

Data Acquisition. The combined laser-extinction and two-wavelength pyrometry measurements yielded six output signals that were sampled at 833 Hz. The procedure involved collecting 500 samples in clear air, as a reference, and 3500 samples within the flame. Results involving temperatures less than 900 K and soot volume fractions less than 0.01 ppm were discarded since sensitivity was not adequate in these ranges.

Aside from gradient broadening, which has already been discussed, experimental uncertainties of the soot volume fraction measurements were largely due to uncertainties in the estimates of the refractive indices of soot, the Rayleigh-scattering approximation, signal-to-noise ratios and discretization errors of the digital data acquisition system. Uncertainties due to refractive indices are relatively large in the absolute sense with values over the range reported by Tien and Lee (1982), Dalzell and Sarofim (1969) and Charalampopoulos and coworkers (1987, 1988) yielding variations of soot volume fractions up to 25%. For this range of refractive indices, experimental uncertainties of soot volume fractions are less than 40% for $f_v > 0.1$ ppm, increasing to roughly 60% for $f_v \approx 0.01$ ppm. Present results were repeatable well within these limits since a single set of refractive indices were used and effects of Mie scattering were ignored. Use of the refractive indices of Habib and Vervisch (1988) and Batten (1985) would result in increases of soot volume fractions from the values reported here by factors of roughly 2 and 4, respectively.

Aside from effects of gradient broadening, which were discussed earlier, experimental uncertainties of the two-wavelength pyrometer measurements were dominated by signal-to-noise ratios and the discretization errors of the digital data acquisition system. In particular, drift of the photomultiplier tubes was small (less than 1%) while effects of refractive index uncertainties were small since a ratio of the $\varepsilon_{\lambda i}$ was used—assuming that the refractive indices were constant over the relevant wavelength range. The resulting uncertainties of the temperature measurements are estimated to be less than 40 K for $f_v > 0.1$ ppm, increasing to 80 K for $f_v \approx 0.01$ ppm. Crosschecks of the results using the two wavelength pairs (550,700 nm and 700,800 nm), as well as repeatability checks, were well within these estimates.

3.2.3 Test Conditions

The test conditions are summarized in Table 4. Two flame operating conditions, with roughly a 2:1 change in fuel flow rate, were used for each fuel. Burner Reynolds numbers were in the range 470-1940, however, the flames were strongly buoyant and the burner Reynolds number is not a good indicator of their properties: the region where measurements were made was turbulent. The flames corresponded to pool-like fires with burner exit Richardson members greater than 18 and ratios of the flame height to the burner exit diameter less than 18. Radiative heat loss fractions for each fuel were nearly constant, typical of strongly-buoyant flames (deRis, 1978).

Table 4 Test Conditions for Luminous Turbulent Flames[a]

Fuel	Acetylene		Propylene		Ethylene		Propane	
Reynolds Number[b]	470	840	750	1370	480	900	770	1940
Richardson Number[c]	68	22	108	32	77	22	116	18
Heat Release Rate (kW)	10.1	18.0	11.5	21.1	7.8	14.4	13.0	32.7
Radiative Heat Loss Fraction (%)	62	61	40	44	36	40	25	28
Flame Height (mm)[d]	400	550	540	720	460	670	550	890
Residence Time (ms)[e]	257	295	504	600	334	360	552	660

[a]Vertical fuel injection into still air at NTP from a 50 mm diameter burner. Acetylene: Commercial Grade, Detroit Welding Co.; propylene and ethylene: chemically Pure Grade, Linde Division of Union Carbide and Air Products and Chemicals Co.; propane: chemically Pure Grade, Matheson Gas Products.

[b]$Re = u_o d/\nu_o$, based on average velocity at burner exit and burner gas properties.

[c]$Ri = ad/u_o^2$ based on average velocity at burner exit.

[d]Visible flame height from photographs.

[e]Time between termination of fuel flow and disappearance of all flame luminousity.

Flame heights and residence times were measured in the same manner as Sivathanu and Faeth (1989a). Flame heights were taken as averages from motion pictures of the flames in a darkened room. Residence times were measured from dark-field motion picture photographs as well: they were taken to be the time interval between ending the fuel flow rate with a shutter at the burner exit and the disappearance of all flame luminousity on the films.

Flame heights were in the range 400-900 mm, which provided reasonable spatial resolution for the optical probe. Flame residence times were all greater than 250 ms. Except for propane, this was sufficient for the flames to be in the long-residence-time regime where soot generation efficiencies are independent of burner operating conditions. As noted by Sivathanu and Faeth (1989a), the long-residence-time regime is only approached for present operating conditions for propane since reaching this condition would require excessively large flames for laboratory conditions. Flame residence times vary rather slowly with fuel flow rate; therefore, flame residence-time variations were not large for each fuel, ca. 20%. Instead, effective residence times were varied by considering different heights above the burner over a relatively wide range, e.g., x/d = 2.5, 3.8 and 5.7.

3.3 Results and Discussion

3.3.1 Flame Position and Operating Conditions

In order to obtain data over the full range of conditions where soot was present in the fuel-rich (underfire) region, measurements were made at various radial positions for each height above the burner, as follows: r/x = 0-0.12, 0-0.15 and 0-0.18 for x/d = 2.5, 3.8 and 5.7, respectively. However, an effect of position or fuel flow rate was not observed: such changes only served to emphasize results at different levels of mixing (or mixture fractions) of the flow. Thus, in order to avoid cluttering the plots of the results, the radial position is never indicated while the axial position and burner Reynolds number are only indicated on the plots of temperature/soot volume fraction correlations. Naturally, the absence of effects of position and flow rate on relationships between temperatures and soot volume fractions for a particular fuel is supportive of the existence of state relationships for these quantities in the underfire region.

3.3.2 Conditional PDF's of Temperature

Probability density functions (PDF's) of temperature, conditioned on soot volume fraction, provide a useful indication of the character of the measurements. These results were obtained by ordering all the data for a particular fuel by soot volume fraction and then separating the data into five groups each containing roughly 64,000 members. The mean soot volume fraction and the PDF of temperature were then determined for each group.

The resulting conditional PDF's for turbulent acetylene, propylene, ethylene and propane flames are illustrated in Figs. 12-15. This ordering corresponds to decreasing propensity to soot, based on laminar flame heights at the normal smoke point (Sivathanu and Faeth, 1989a; Schug et al., 1980). The present results indicate that the same ordering is maintained in the underfire region with respect to the maximum group-averaged soot volume fraction for each fuel. The conditional PDF's of temperature exhibit a single, relatively-sharp, peak at the highest soot volume fraction for each fuel. As soot volume fractions decrease, however, the conditional PDF's of temperature become progressively broader. At the lowest soot volume fractions considered, the conditional PDF's of

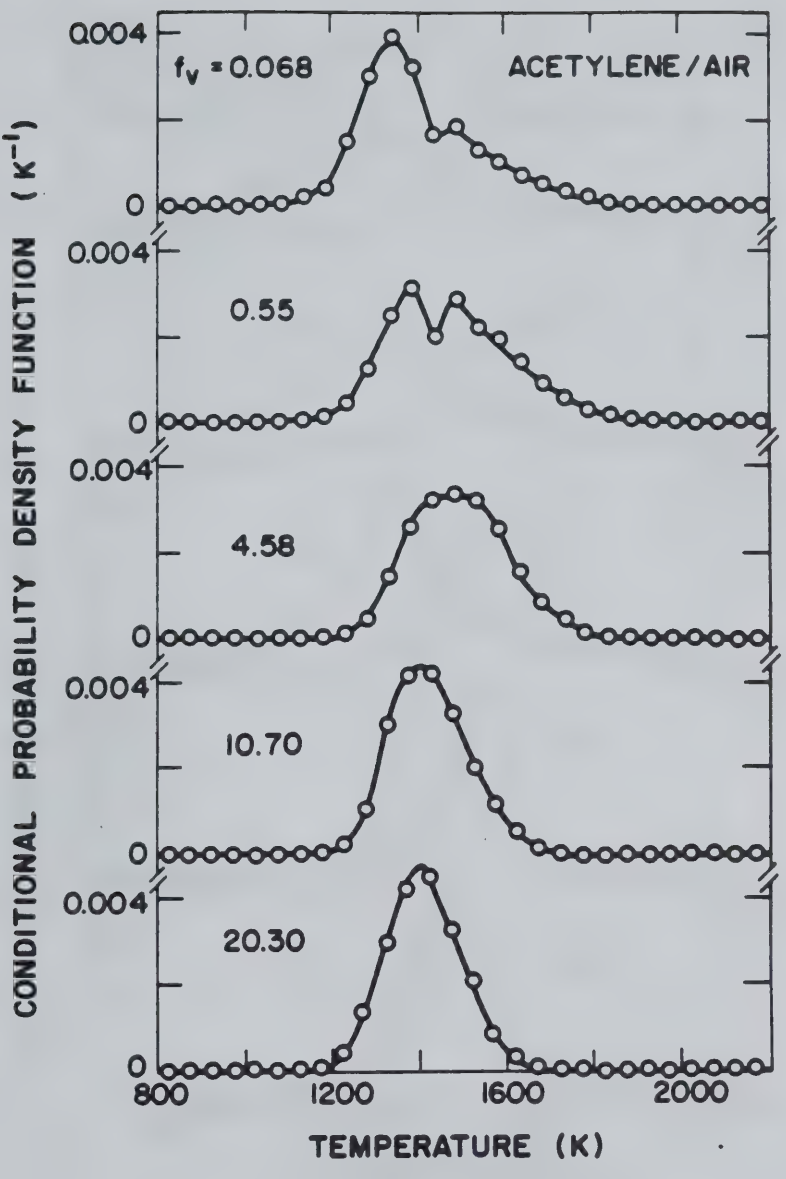

Figure 12 Conditional PDF's of temperature for turbulent acetylene/air diffusion flames.

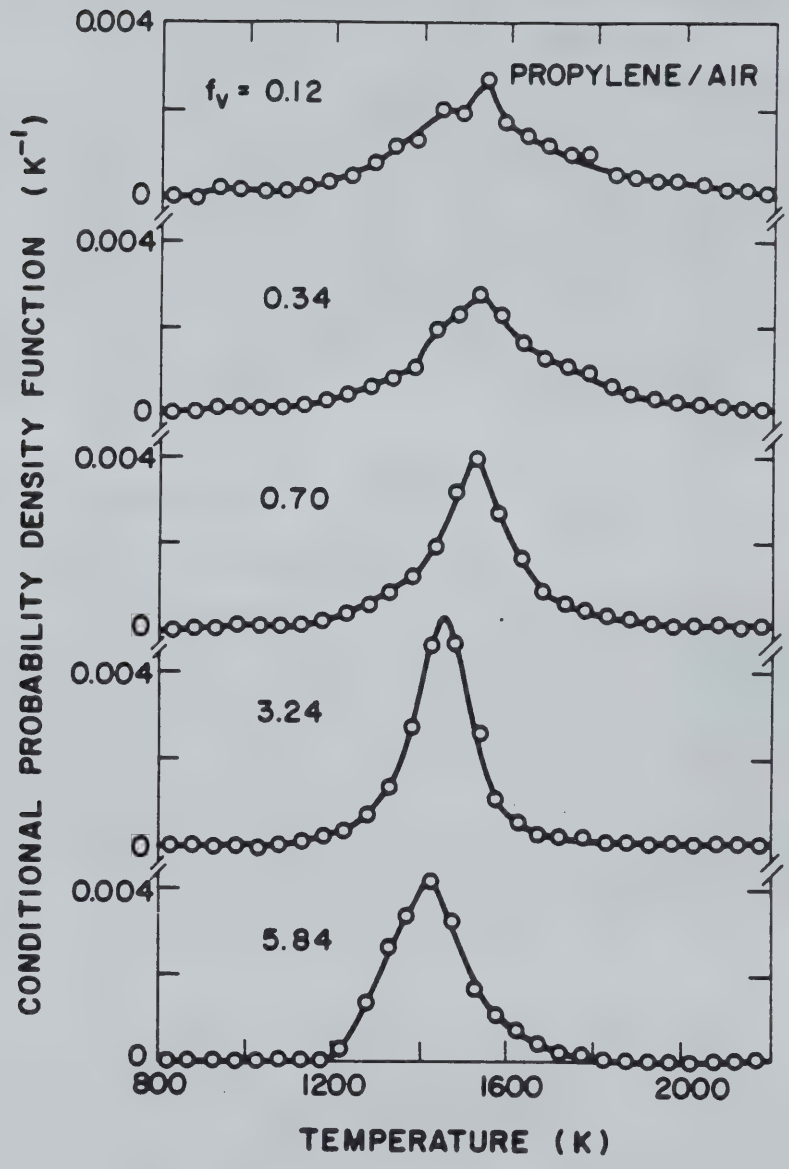

Figure 13 Conditional PDF's of temperature for turbulent propylene/air diffusion flames.

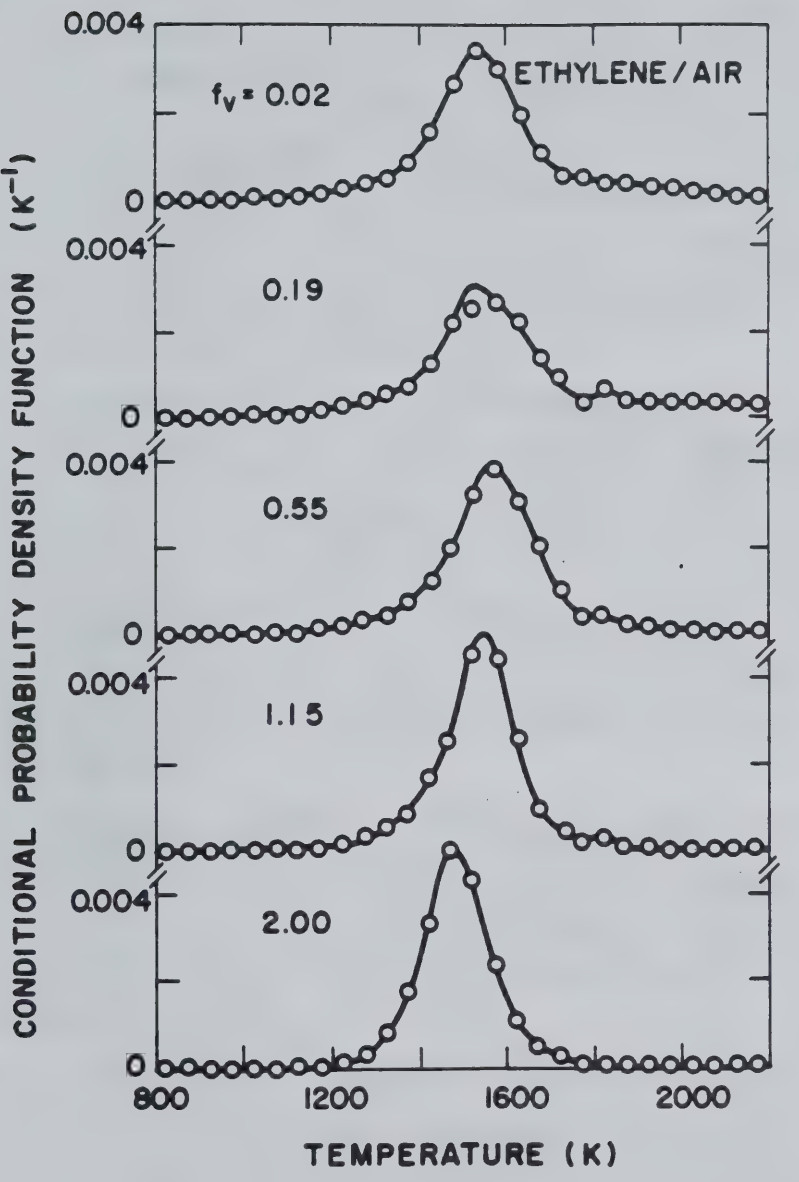

Figure 14 Conditional PDF's of temperature for turbulent ethylene/air diffusion flames.

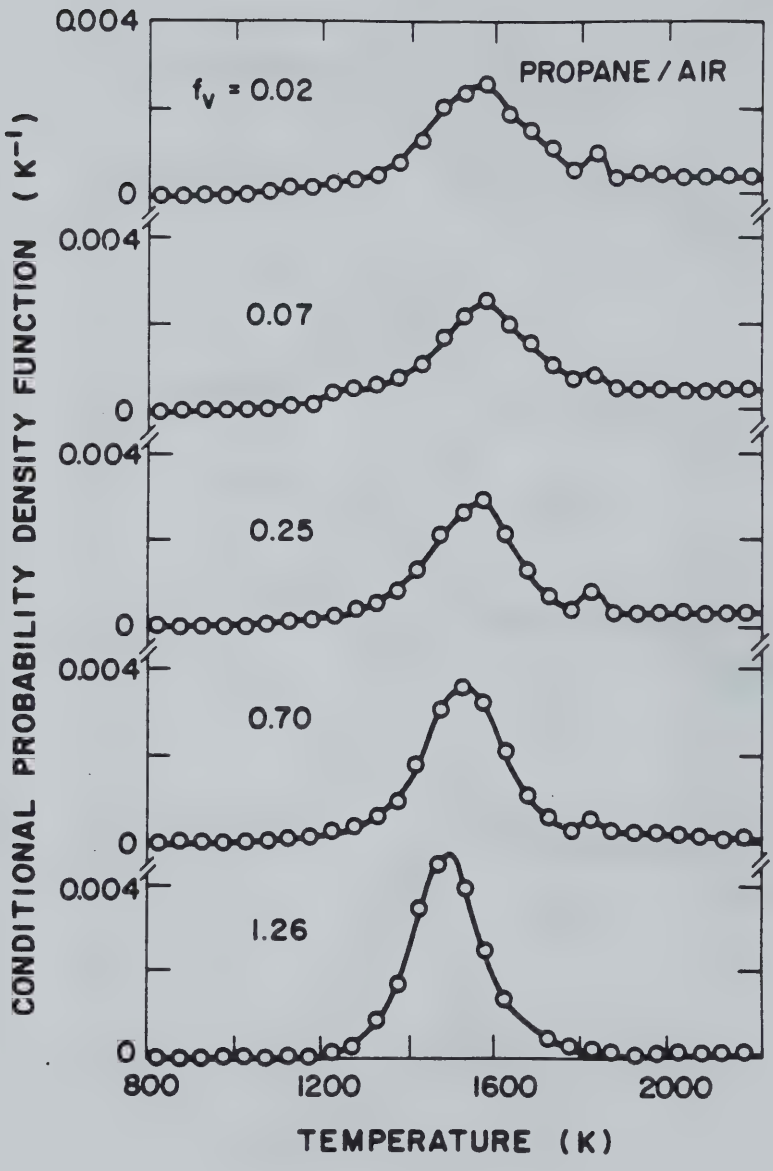

Figure 15 Conditional PDF's of temperature for turbulent propane/air diffusion flames.

temperature tend to split into two peaks, although the high-temperature peak is never very prominent and it is not observed at all for propylene. Even with the broadening, however, the temperature ranges of the conditional PDF's of temperature are relatively narrow in spite of variations of soot volume fractions in the range 10^2-10^4 for the various fuels.

Many of the features of Figs. 12-15 can be reconciled with state relationships within the soot spikes for fuel-rich conditions—typified by the results illustrated for acetylene and ethylene in Fig. 8. First of all, the maximum group-averaged soot volume fractions for acetylene and ethylene are ca. 20 and 2 ppm for both the present results and the laminar flame results illustrated in Fig. 8. Secondly, maximum soot volume fractions in the soot spike of the state relationships of Fig. 8 are associated with a relatively narrow range of temperatures; similar behavior in the turbulent flames should yield a single, relatively-sharp peak in the conditional PDF of temperature at maximum soot volume fractions, which agrees with the results of Figs. 12-15. Finally, lower values of soot volume fractions involve the two sides of the state relationships, where temperatures are somewhat different; this should yield broader peaks in the conditional PDF's of temperature, and possibly splitting into two peaks at the lowest soot volume fractions, which is also in accord with the results seen in Figs. 12-15.

Several properties of the conditional PDF's of temperature are summarized as a function of mixture fraction in Table 5, as follows: mean temperatures, temperatures of the low- and high-temperature peaks (when present), and the standard deviations of the distributions. In general, mean temperatures of the distributions for each fuel vary less than 100 K over the whole range of soot volume fractions. Mean temperatures reach a maximum at intermediate values of soot volume fractions. This reflects the fact that the maximum soot volume fraction and temperature conditions do not coincide, on the one hand, while low soot volume fractions are associated with low temperatures at the start of formation of soot on the other. Maximum mean temperatures of the distributions increase in the order acetylene, propylene, ethylene and propane. This follows the order of reduction of the radiative heat loss fraction of the fuels (see Table 4) which is expected to increase flow temperatures.

Mean temperatures in Table 5 are generally just slightly above the temperature of the low-temperature peak since the high temperature peak is not very prominent. Differences in temperature between the low and high temperature peaks also increase in the order of reduced radiative heat loss fractions. This suggests that the high-temperature peak is associated with the fuel-lean side of the soot spike, and exhibits higher temperatures as radiative heat losses are reduced, while temperatures where soot first begins to appear are likely to be similar for all the fuels.

The standard deviations of the conditional PDF's of temperature in Table 5 are approximately 100 K at the maximum soot volume fraction. This is roughly twice the uncertainty estimate of the temperature measurements at this condition, ca. 40 K, even though peak soot volume fractions should be associated with a single temperature if the soot volume fraction state relationship concept is exact. Nevertheless, this behavior is not surprising in view of potential effects of gradient broadening of measurements along a finite-length optical path and the grouping of data to find a conditional PDF of temperature. On the other hand, some variation of temperatures at peak soot volume fractions, similar to the results in the laminar soot spike of acetylene in Fig. 8, cannot be ruled out. The progressive increase of the standard deviations of the conditional PDF's of temperature with decreasing soot volume fractions is consistent with the wider range of temperatures anticipated near the base of the soot spike, as noted earlier.

Table 5 Properties of Conditional PDF's of Temperature

f_v	T_M(K)	T_L(K)	T_U(K)	σ(K)
Acetylene:				
0.068	1395	1320	1470	140
0.55	1465	1380	1470	135
4.58	1485	1420	1520	110
10.7	1425	1410	----	95
20.3	1415	1400	----	90
Propylene:				
0.12	1520	1540	----	210
0.34	1535	1520	----	200
0.70	1505	1520	----	150
3.24	1455	1450	----	120
5.84	1445	1420	----	120
Ethylene:				
0.02	1550	1520	----	175
0.19	1575	1520	1810	195
0.55	1570	1560	1810	150
1.15	1530	1540	1820	110
2.00	1490	1460	----	95
Propane:				
0.02	1580	1560	1840	195
0.07	1590	1560	1820	200
0.25	1570	1560	1810	190
0.70	1530	1520	1810	150
1.26	1490	1490	----	110

3.3.3 Temperature/Soot Volume Fraction Correlations

The correlations between instantaneous temperatures and soot volume fractions for turbulent acetylene, propylene, ethylene and propane flames are illustrated in Figs. 16-19. Results in the upper part of the figures are for the underfire region. In order to avoid excessive overlapping of symbols on the plots, each of the data points for the underfire region represents the average of the nearest 100 instantaneous determinations of soot volume fractions and temperatures. The data in the underfire region represent a range of radial positions and are identified to indicate heights above the burner and burner Reynolds numbers; however, changes of these variables did not affect the results, as noted earlier.

State relationships illustrated in Figs. 16-19 for the underfire region include results based on the measurements within laminar flames reported by Gore and Faeth (1986, 1987) for acetylene and ethylene, and correlations obtained from the present flames. The correlations of Gore and Faeth (1986, 1987) were obtained by transcribing the state relationships in the soot spikes of Fig. 8 to the soot volume fraction/temperature coordinates of Figs. 16-19. The temperatures needed for this change of variables were computed in the same manner as Gore and Faeth (1986, 1987). This involved computations of flame temperature as a function of mixture fraction using the measured concentrations of major species from the state-relationship correlations and thermochemical properties from the Gordon and McBride (1971) code. It was assumed for these computations that the flames lost a fixed fraction of their chemical energy release at each mixture fraction due to radiation, with this fraction being the same as the radiative heat loss fraction of the flame as a whole. Radiative heat loss fractions were measured for the various fuels; as noted earlier, they only depend on fuel type for strongly-buoyant flames (deRis, 1978).

The present correlations for the underfire region appearing in Figs. 16-19 were taken to be the locus of the mean temperatures of the conditional PDF's of temperature, summarized in Table 5. The standard deviations of the conditional PDF's are also marked on the plots in order to provide a quantitative measure of the span of the temperature data. The lower peaks of the conditional PDF's are relatively close to the mean temperatures; the upper peaks are roughly near the upper end of the standard deviation limits at low soot volume fractions.

Results plotted in the lower part of Figs. 16-19 involve the measurements and state relationship correlations for the fuel-lean (overfire) region of turbulent flames from Sivathanu et al. (1988) and Sivathanu and Faeth (1989a). These measurements and correlations were both transcribed from soot volume fraction/mixture fraction coordinates to the coordinates of Figs. 16-19 in the same manner as the underfire soot volume fraction state relationship correlations. The overfire data and correlations pertain to the long residence-time regime; therefore, even though a range of positions and flame operating conditions were involved, these variables are not indicated since their effect is small.

The results illustrated in Figs. 16-19 strongly suggest the presence of soot spikes in the underfire region of the turbulent flames, analogous to the soot spikes observed in the fuel-rich region of laminar flames. This can be seen by comparing the soot spike state relationships of Gore and Faeth (1986, 1987) for acetylene and ethylene, which were obtained in laminar flames, with the present measurements in turbulent flames (see Figs. 16 and 18). First of all, maximum soot volume fractions for the laminar and turbulent flames are essentially the same, as noted earlier. Similarly, the temperature ranges of the present measurements are nearly the same as the span of the laminar state relationships at low soot volume fractions. The temperature levels of the soot spike for various soot volume fractions differ somewhat for the laminar and turbulent flames, however, these differences

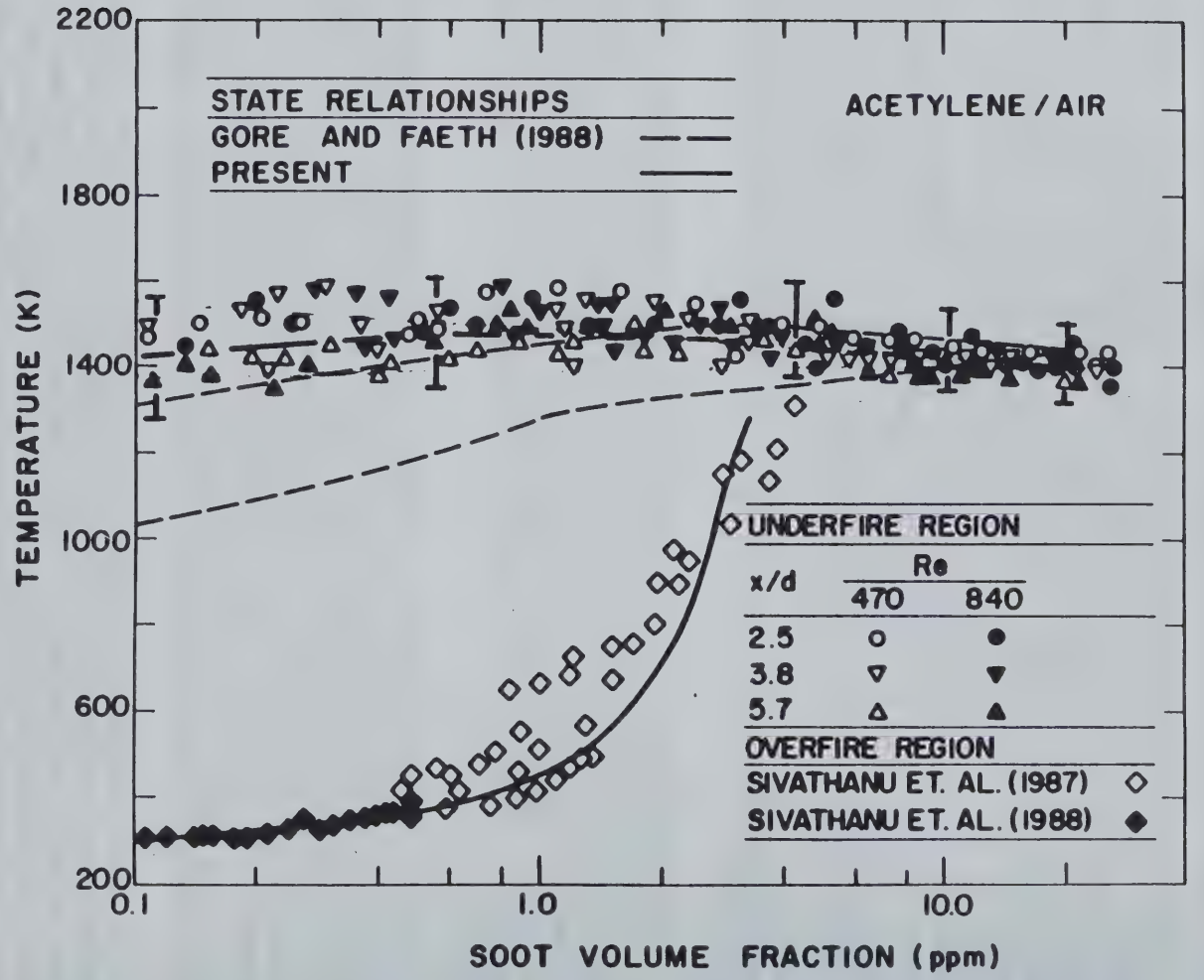

Figure 16 Correlation between soot volume fraction and temperature for turbulent acetylene/air diffusion flames.

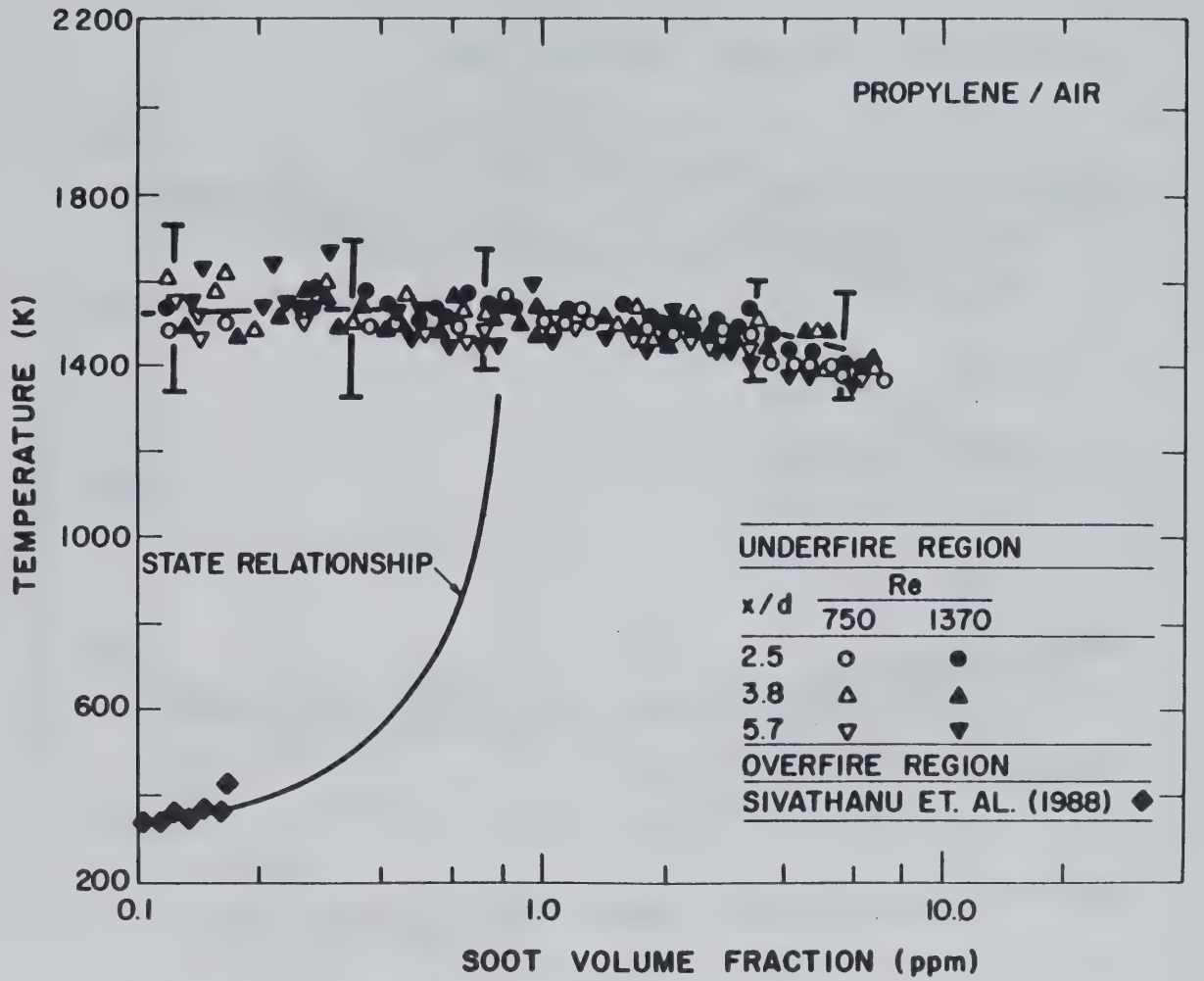

Figure 17 Correlation between soot volume fraction and temperature for turbulent propylene/air diffusion flames.

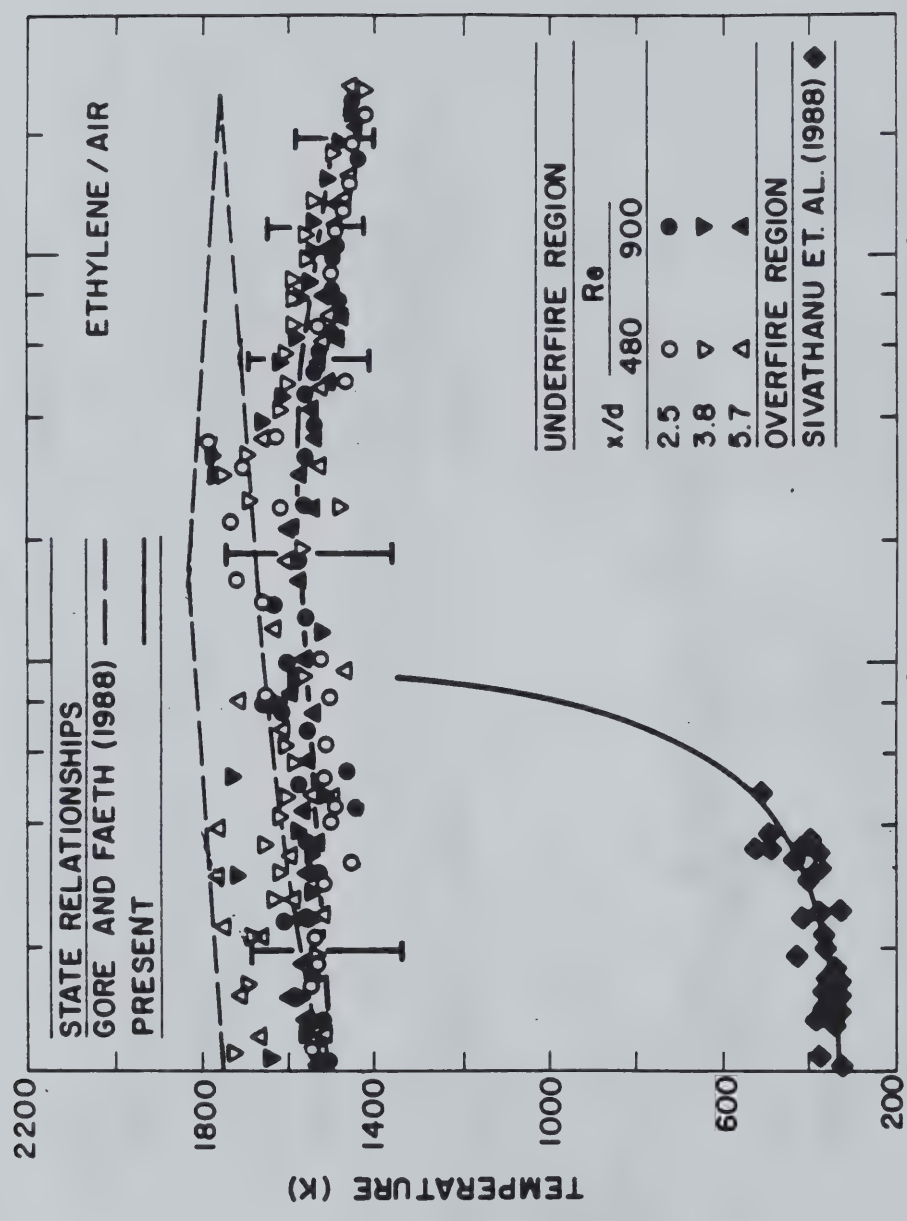

Figure 18 Correlation between soot volume fraction and temperature for turbulent ethylene/air diffusion flames.

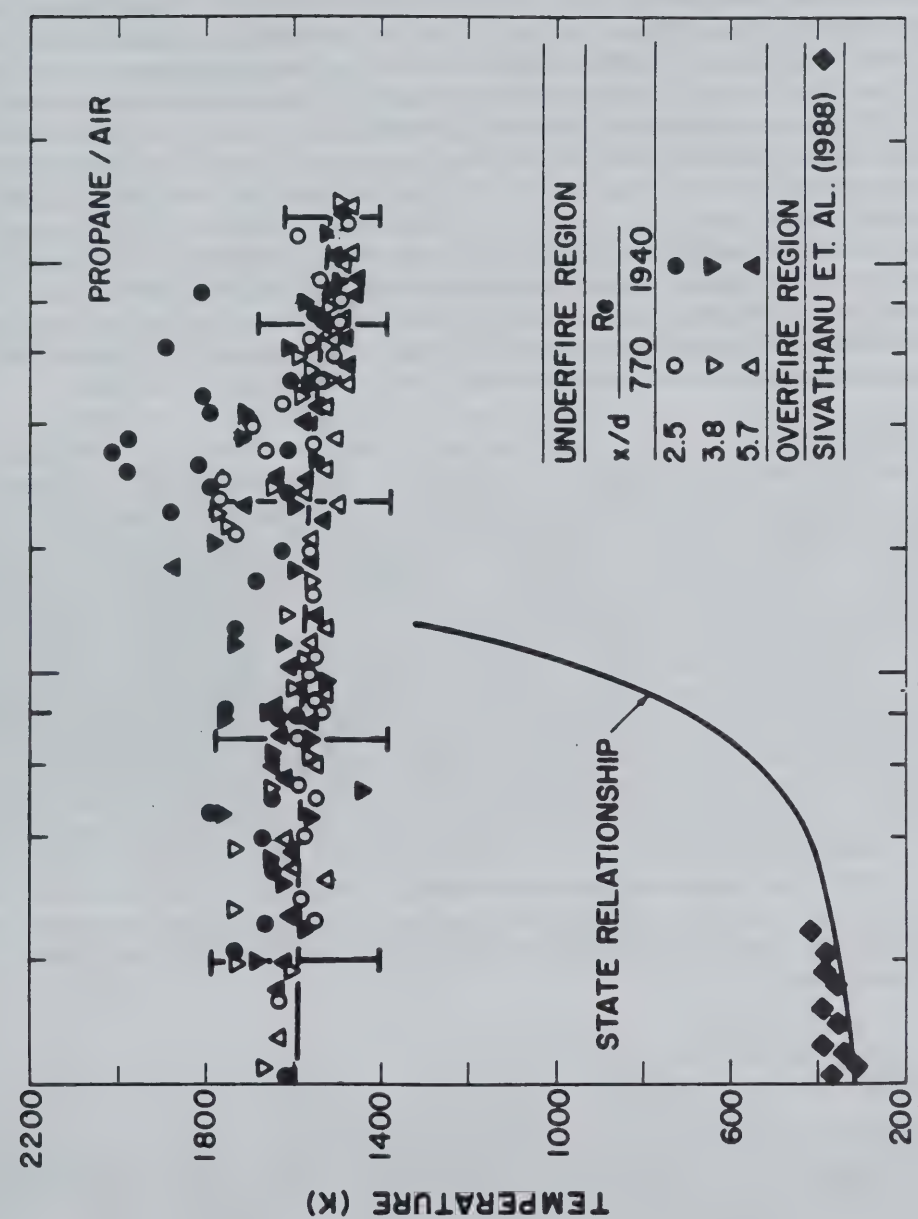

Figure 19 Correlation between soot volume fraction and temperature for turbulent propane/air diffusion flames.

can easily result from attempts to fit a state relationship to the limited and scattered measurements for laminar flames (see Fig. 8) as well as uncertainties in the estimates of state relationships for temperatures. The narrow temperature range where soot is present in the underfire region for propylene and propane (Figs. 17 and 19) also suggests a soot spike for these fuels since the mixture fraction range must be limited as well.

The narrow temperature ranges where soot is observed in the underfire region in Figs. 16-19 also tends to support past simplifications of constant-temperature soot layers for estimates of continuum radiation from flames (deRis, 1978). This approximation tends to be more appropriate for heavily sooting fuels like acetylene and propylene where large radiative heat losses reduce peak temperatures in the flames. In contrast, propane only has a radiative heat loss fraction of 25-28% (see Table 4) and exhibits a span of temperatures in excess of 400 K for relatively-high soot volume fractions; therefore, the constant-temperature soot layer approximation is clearly less satisfactory for this fuel. Large flames of even heavily-sooting fuels may also be problematical because they are more adiabatic as a whole since soot in the overfire region shields heat losses from the high-temperature regions of the flow (Gore and Faeth, 1986, 1987). However, portions of the soot layers within these flames still must be relatively cool, promoting local radiative exchange from high- to low-temperature regions of the soot layer; thus, local behavior within very large flames may not be very different from present observations. However, additional study is needed to determine whether this conjecture is true.

Extrapolation of the overfire correlation meets the soot spike abruptly in Figs. 16-19, analogous to the behavior of the soot volume fraction state relationships illustrated in Fig. 8. This occurs since there are two paths to small soot volume fractions on the lean side of the maximum soot volume fraction. One path represents approach to stoichiometric conditions along the sides of the laminar flamelets, similar to processes along the sides of laminar flames. In this case soot volume fractions become small as soot oxidation is enhanced near the stoichiometric condition while temperatures remain relatively high. These conditions are most representative of the high-temperature side of the soot spike seen in Figs. 16-19—perhaps corresponding to the high-temperature peak of the conditional PDF of temperature. The other path involves passage of the soot layer as a whole through the tip of a turbulent flamelet, analogous to processes near the tip of a sooting laminar flame. In this case, once soot oxidation ceases, additional reductions of concentrations of soot are only due to passive mixing in the overfire region, and follow the overfire correlations illustrated in Figs. 16-19. As a result, the intersection of the two correlations represent conditions when soot oxidation is quenched. Thus, the overfire and underfire correlations are relevant to two different statistical populations and are separated by a narrow oxidation zone as the soot layer passes through mixture fractions near stoichiometric conditions.

3.4 Conclusions

Instantaneous soot volume fractions and temperatures were measured in the fuel-rich (underfire) region of turbulent acetylene, propylene, ethylene and propane diffusion flames burning in still air. The test flames were relatively large with characteristic residence times greater than 250 ms, placing them in the regime where soot generation efficiencies are independent of position in the overfire region and burner operating conditions (Sivathanu and Faeth, 1989a). The test flames were also highly-buoyant pool-like fires with burner exit Richardson numbers greater than 18 so that the results are largely relevant to natural fires. The main conclusions of the study for these test conditions are as follows:

1. Instantaneous temperatures and soot volume fractions are highly correlated in the fuel-rich (underfire) region. These correlations depend on fuel type but were essentially independent of burner operating condition and position in the underfire region.

2. The correlations between temperatures and soot volume fractions in the underfire region are consistent with the properties of soot volume fraction state relationships for the soot spike region of laminar flames. In particular, maximum soot volume fractions and temperature ranges within the laminar and turbulent soot spikes were essentially the same for acetylene and ethylene flames—the only flames where this comparison could be made. This suggests that useful information concerning soot volume fraction state relationships can be obtained in laminar flames where measurements are much easier than in turbulent flames.

3. The soot spike in the underfire region of turbulent flames exhibits a relatively narrow range of temperatures—particularly for heavily-sooting fuels where radiative heat loss fractions from the flame are relatively high. This provides some justification for the use of a constant-temperature soot layer approximation for estimates of continuum radiation from flames.

While present findings support the existence of soot volume fraction state relationships in turbulent flames, for the purposes of radiation predictions, the results are only provisional. Measurements of soot volume and mixture fractions in turbulent flames are still needed to directly evaluate the soot volume fraction state relationship concept. Furthermore, additional measurements in laminar flames, along the lines of Gore and Faeth (1986, 1987), are also needed to better establish the correlation between soot volume fraction state relationships in laminar and turbulent flames. Finally, conclusions about soot volume fraction state relationships are influenced by the properties of the refractive indices of soot for long residence times in fuel-rich soot layers; therefore, existing controversies concerning the refractive indices of soot in flames (Tien and Lee, 1982; Dalzell and Sarofim, 1969; Charalampopoulos and coworkers, 1987, 1988; Batten, 1985; Habib and Vervisch, 1988) must be resolved in order to make substantive progress on this issue.

4. MIXTURE FRACTIONS IN TURBULENT FLAMES

4.1 Introduction

Results discussed thus far suggest that the laminar flamelet concept, where scalar properties satisfy state relationships that are only functions of mixture fraction, provides a useful approach for treating buoyant turbulent diffusion flames having reasonably-long characteristic flame residence times—typical of unwanted fires. We have seen that generalized state relationship correlations for the concentrations of major gas species are feasible; soot volume fractions in the overfire region can be represented by a constant soot generation efficiency, yielding a state relationship for this property; and evidence is mounting that soot volume fractions in the underfire region satisfy universal state relationships as well, at least to the extent needed for flame radiation predictions. Less information has been developed concerning the state relationship for temperature in turbulent diffusion flames, however, simplified methods for estimating this property have been proposed that yield reasonable estimates of flame radiation properties (Faeth et al.,

1988a,b; Gore and Faeth, 1986, 1987; Gore et al., 1987a,b,c; Jeng and Faeth, 1984c; Jeng et al., 1984; Kounalakis et al., 1988, 1989). In view of these findings, a better understanding of the properties of mixture fraction is needed; therefore, the objective of this phase of the investigation was to measure the statistical properties of mixture fractions in turbulent diffusion flames in still air—emphasizing properties needed for flame radiation predictions.

The main difficulty encountered when predicting radiation from turbulent diffusion flames is that turbulence/radiation interactions cause mean radiative heat fluxes to be higher (often 2-3 times higher) than estimates based on mean scalar properties (Faeth et al., 1988a,b). Recent work has shown that this can be handled by stochastic simulation of mixture fractions along radiation paths through the flame and then summing radiation predictions for a sufficient number of realizations to obtain statistically-significant radiation properties (Faeth et al., 1988 a,b; Kounalakis et al., 1988, 1989). A convenient method for simulating a realization of mixture fractions along a radiation path follows statistical time-series simulation techniques described by Box and Jenkins (1976). In general, adequate simulations can be achieved if the probability density functions (PDF's), spatial correlations and temporal correlations (when the temporal properties of radiation fluctuations are sought) of mixture fractions are satisfied (Kounalakis et al., 1988, 1989); therefore, the present investigation concentrated on these properties. Work thus far has been limited to turbulent flames in free shear flows (turbulent buoyant jet flames).

Past studies of mixture fractions in turbulent free shear flows have concentrated on mean and fluctuating mixture fractions for nearly constant density nonreacting conditions. Some typical studies along these lines include: Becker et al. (1967), Birch et al. (1978), Corrsin and Uberoi (1951) and Pitts and Kashiwagi (1984). List (1984) reviews recent work of this type. Becker et al. (1967) and Corrsin and Uberoi (1951) also measure temporal correlations and symmetric spatial correlations (correlations between two points along a diameter that are spaced equidistantly from the axis) — the last being the only available spatial correlation measurements. Existing measurements in flames have been limited to single-point measurements: the work of Stårner and Bilger (1980) yielding mixture fractions for hydrogen jet flames in coflowing air is typical. Thus, information on PDF's and spatial and temporal correlations of mixture fractions is generally not available and past simulations have been carried out using *ad hoc* approximations of these properties based on limited results for incompressible jets and other noncombusting flows.

The objective of the present portion of the investigation was to help fill this gap in the literature by measuring moments, PDF's, spatial correlations, and temporal correlations and spectra of mixture fractions in turbulent jet diffusion flames. Carbon monoxide/air flames were chosen since they offer several advantages: effects of differential diffusion are minimized; their state relationships closely follow estimates based on the assumption of local thermodynamic equilibrium (Gore et al., 1987b); their radiative heat losses are low (ca. 10%), which minimizes uncertainties of state relationships for temperature; and this reactant combination has an unusually high stoichiometric mixture fraction, which improves the accuracy of mixture fraction fluctuation measurements in the important region near stoichiometric conditions. The measurements were carried out using a two-point Mie scattering system with the data reduced to yield both mass-weighted (Favre)- and time-averaged mixture fraction properties.

In the following, experimental methods are discussed first. Results are then considered, treating moments, PDF's correlations and spectra of mixture fractions in turn.

4.2 Experimental Methods

4.2.1 Apparatus

The test apparatus was similar to earlier studies of the structure and radiation properties of nonluminous turbulent diffusion flames in this laboratory (Gore et al., 1987b,c; Kounalakis et al., 1988, 1989). A sketch of the apparatus appears in Fig. 20.

The apparatus involved turbulent round jet diffusion flames injected vertically upward within a screened enclosure to reduce effects of room disturbances. The enclosure was $1.1 \times 1.2 \times 2.7$ m high and was covered with one layer of screen (630 wires/m with a wire diameter of 0.25 mm). The enclosure had a metal hood at the top which was fitted with a 0.4 m diameter flexible exhaust duct. A blower and bypass system allowed the exhaust flows to be matched in order to minimize room disturbances. Rigidly-mounted optical instrumentation was used so that the burner was traversed for measurements at various points in the flames. The entire enclosure could be traversed using a linear bearing system and a stepping-motor driven linear positioner (positioning accuracy of 5 μm) to make radial traverses while the flow remained centered in the enclosure. Vertical traverses were carried out by moving the burner with a manual linear positioner (positioning accuracy of 0.64 mm).

The burner involved a flow straightener followed by a contraction from a 25 mm diameter feed line to a constant-diameter passage having a diameter of 7.04 mm. The constant-diameter passage was sufficiently long (40 passage diameters) so that the flow at the exit was nearly fully-developed turbulent pipe flow. The burner was cooled with a water coil made from flattened 6.35 mm diameter copper tubing which was wrapped around the outside surface of the constant-diameter passage and ended 7 mm from the exit. A small amount of hydrogen (ca. 2% on a mass basis) was added to the carbon monoxide fuel gas so that the flames stabilized at the burner exit.

Fuel gases were stored in commercial cylinders under pressure. Gas flow rates were controlled with pressure regulators and metering valves. The flow rate of carbon monoxide was measured using a Merriam laminar flow element while the hydrogen flow rate was measured with a rotometer (Matheson, model 603). Both gas flow meters were calibrated using wet-test meters.

4.2.2 Instrumentation

Mean and fluctuating mixture fractions were measured using Mie scattering from seeding particles in the fuel gas, similar to Becker et al. (1967) and Stårner and Bilger (1980), except that the arrangement provided for two-point measurements so that spatial correlations could be obtained. A sketch of the arrangement appears in Fig. 21.

The particle scattering signal was provided by the beam from an unfocussed argon-ion laser (Coherent, Innova 90-4) operating with 500 mW of optical power at 488 nm (beam diameter to the e^{-2} points of 1.5 mm). The laser beam was passed horizontally through the flame axis. Light scattered from the laser beam is proportional to the number of seeding particles in the measuring volume, and thus the product of density and mixture fraction of the flow, since flame Reynolds numbers were high ($\geq$ 7400) and effects of laminar transport were small. The light scattered from the laser beam was measured using two detectors: one mounted rigidly and the other traversible along the laser beam. Since the burner could be traversed horizontally and vertically, all points in the flames could be accessed for two-point measurements. The scattered light signals were observed at right

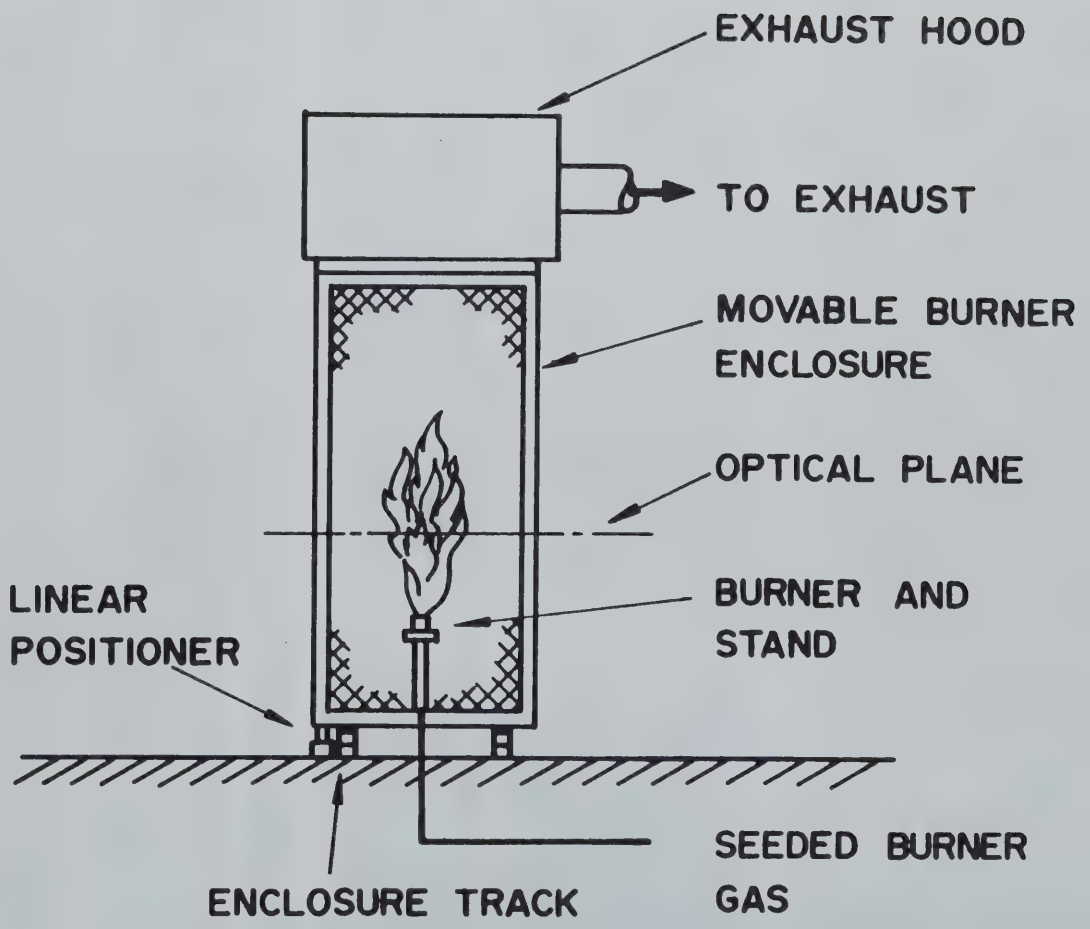

Figure 20 Sketch of nonluminous flame apparatus.

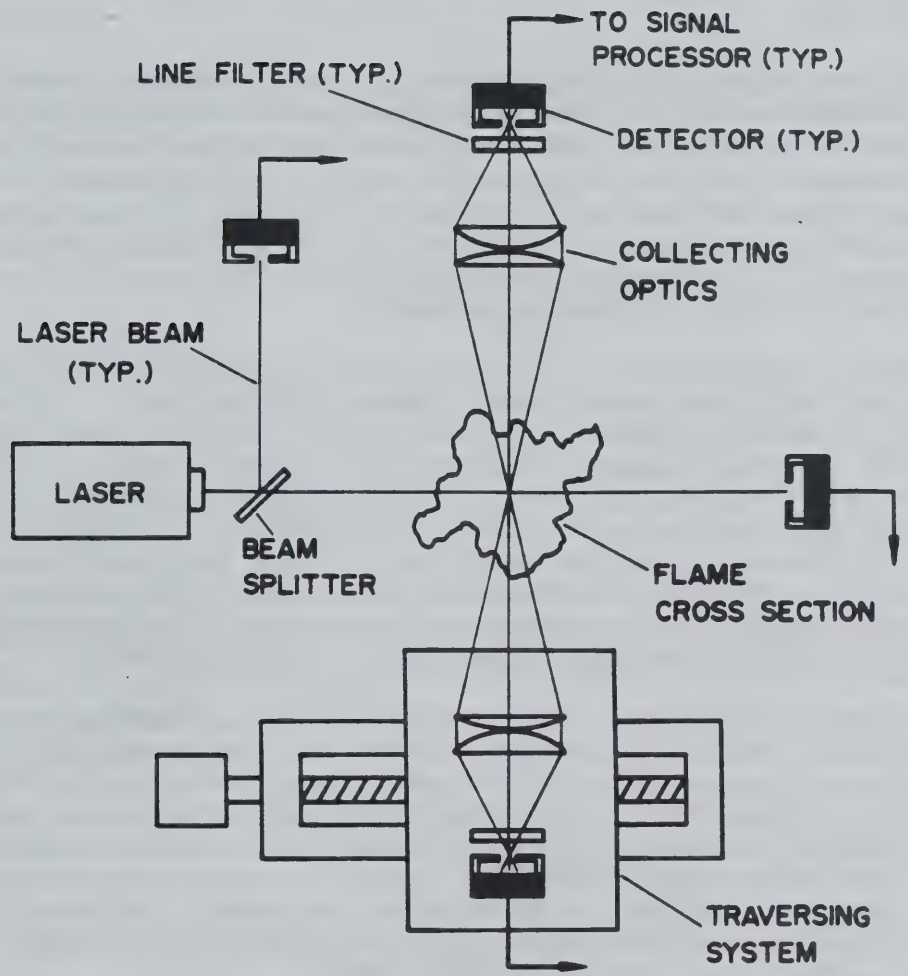

Figure 21 Sketch of two-point Mie-scattering system.

angles to the laser beam with collecting lens systems having diameters of 145 mm and focal lengths of 165 mm. The apertures of the detectors were selected to give a measuring volume diameter of 1 mm while the length of the measuring volume was comparable to the diameter of the laser beam (1.5 mm). The detectors were photomultipliers (Hamamatsu, Model R268) with laser line filters (10 nm bandwidth) over the apertures to minimize effects of background and flame radiation. These measurements were made with the room darkened to reduce effects of background signals as well. The operation of the laser system was monitored with two laser power meters (Newport, Model 820): one measuring laser power before crossing the flame to detect laser power variations, the other measuring laser power after passing through the flame to correct for laser extinction by scattering from the seeding particles.

Aluminum oxide particles (300 nm nominal diameter) were used to seed the fuel flow using a reverse-cyclone seeder similar to Glass and Kennedy (1977). The seeder geometry and a high jet velocity within the particle storage cylinder (ca. 70 m/s exit velocity) combined to yield a very high particle density (ca. 10^3 particles/mm^3) in the fuel flow, so that effects of shot noise were small (Becker et al., 1967). To avoid accumulation of particles in the fuel feed line, it had smooth transitions between constant area sections: a flow straightener, a 25 mm inside-diameter plastic tube to the burner inlet, a circular contraction, and the 7.04 mm diameter burner passage.

Seeding particle fluctuations as the burner exit were less than 5% but their effect was further reduced by corrections following Stårner and Bilger (1980). This involved continuously monitoring the seeding particle levels at the burner exit using a scattering system similar to the basic instrument. The monitoring system involved a 15 mW HeNe laser directed across the exit of the burner. Light scattered from the center of the passage was measured similar to the other Mie scattering measurements. This approach cannot correct for high frequency changes of seeding concentrations, due to uncertainties in the particle passage times between the burner exit and the measuring volume, however, use of a low-pass filter in the monitoring channel allows for correction of slow variations (up to 5 Hz). This reduced effective seeding fluctuation levels to roughly 3 percent.

The detector outputs were amplified and then low-pass filtered to control alias signals using Ithaco, Model 4213 electronic filters with break frequencies set at 12,500 Hz. The signals were then sampled at 25000 Hz using an a/d converter and buffer storage system (LeCroy, Models 8800, 8212A/8, 8901A). The digital output was then transferred to an IBM 9000 microcomputer for processing. Output signals were also monitored using a LeCroy Model 9400A digital oscilloscope. The final signals were corrected to allow for argon-ion laser power variations; extinction of the laser beam by particles as it passes through the flow, following Shaughnessy (1975); and effects of low-frequency seeding particle fluctuations, following Stårner and Bilger (1980).

The instantaneous detector output is proportional to ρf, where ρ is density and f is mixture fraction. This is converted into mixture fraction using the state relationships for the present fuel/air reactant combination where the fuel consists of a mixture of carbon monoxide and hydrogen — the latter being used to stabilize the flame at the burner exit. Past measurements for both carbon monoxide/air and hydrogen/air flames show that their state relationships closely approximate local thermodynamic equilibrium (Gore et al., 1987b,c). It was assumed that the mixture would approximate thermodynamic equilibrium as well so that the state relationships were found using the Gordon and McBride (1971) computer code. Calculations were performed for both adiabatic flames and those losing 10% of their chemical energy release to the surroundings, the latter being representative of radiative heat losses from the test flames.

The computed state relationships for the present flames are illustrated in Fig. 22. The plots involve temperature, density, $\rho f/\rho_f$ (where ρ_f is the initial density of the fuel gas), and the mole fractions of major gas species as a function of mixture fraction. Results are presented for radiative heat losses of 0 and 10%, although radiative heat losses in this range have little effect on mole fraction distributions. The effect of radiative heat losses in this range for all properties is not very large, with the value of f for a particular value of $\rho f/\rho_f$ varying less than 5% as the radiative heat loss varies in the range 0-10%. Present measurements used the state relationship for 10% radiative heat loss; therefore, given ρf as a function of time, the results plotted in Fig. 22 allow ρ and f to be computed as a function of time as well.

The data processing system actually generated a time series, containing N = 260,000 elements (each) of density and mixture fraction, ρ_i and f_i. The time-averaged density, mixture fraction and mixture fraction fluctuations were then computed in the conventional manner, as follows:

$$\bar{\rho} = \frac{1}{N} \sum_{i=1}^{N} \rho_i \tag{17}$$

$$\bar{f} = \frac{1}{N} \sum_{i=1}^{N} f_i \tag{18}$$

$$\overline{f'^2} = \frac{1}{N} \sum_{i=1}^{N} f_i^2 - \bar{f}^2 \tag{19}$$

The analogous Favre-averaged mean and fluctuating mixture fractions are defined as $\tilde{f} = \overline{\rho f}/\bar{\rho}$ and $\widetilde{f''} = \overline{\rho(f-\tilde{f})^2}/\bar{\rho}$ (Bilger, 1976). Thus, these quantities were computed from the time series, as follows:

$$\tilde{f} = \frac{1}{\bar{\rho} N} \sum_{i=1}^{N} (\rho f)_i \tag{20}$$

$$\widetilde{f''^2} = \frac{1}{\bar{\rho} N} \sum_{i=1}^{N} (\rho f^2)_i - \tilde{f}^2 \tag{21}$$

The time-averaged probability density function (PDF) of mixture fraction was found by finding the number, n_j, of mixture fraction measurements in the range $r_j \pm \Delta f/2$, yielding

$$\bar{P}(f_j) = n_j/(N\Delta f) \tag{22}$$

where f=0 and 1 were handled as half intervals. Present evaluations of equation (22) were undertaken with $\Delta f = 0.01$. Since $\rho = \rho(\phi)$, the Favre-averaged PDF of mixture fraction then becomes

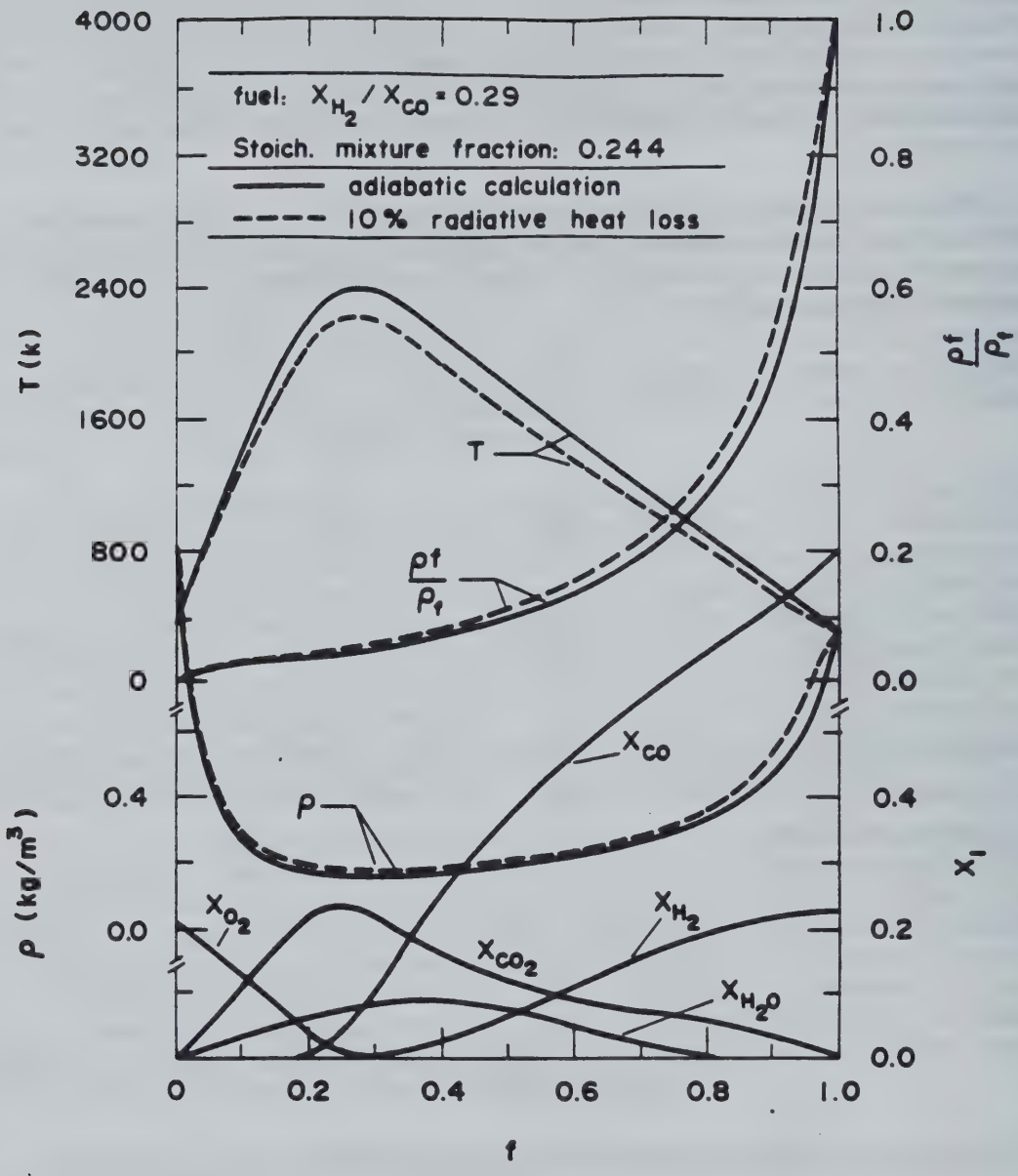

Figure 22 State relationships for carbon monoxide/air diffusion flames.

$$\tilde{P}(f) = \rho(f)\bar{P}(f)/\bar{\rho} \qquad (23)$$

Stochastic simulations of mixture fraction for radiation predictions only require time-averaged temporal correlations, spectra and spatial correlations. These were evaluated from the time series of f in the usual manner.

Experimental uncertainties of time- and Favre-averaged quantities are comparable. They are estimated (95% confidence) to be less than 8% for mean quantities and less than 16% for fluctuating quantities and correlations. These uncertainties were dominated by finite sampling times, with seeding level fluctuations and uncertainties of the state relationships being contributing factors. Measurements were repeatable within these limits over the period of testing.

4.2.3 Test Conditions

Test conditions are summarized in Table 6. Two flames were considered, having burner exit Reynolds numbers of 7400 and 12700. Since the flow at the exit of the burner passage was fully developed turbulent pipe flow, the flames were turbulent throughout. Burner exit Richardson numbers were small, ca. 10^{-4}, and carbon monoxide/air flames are relatively short due to their relatively high stoichiometric mixture fraction; therefore, the flames were nearly buoyant jet flames with small effects of buoyancy except near the edge of the flow since the surroundings were still. Thus, flame lengths (based on reaching the time-averaged stoichiometric mixture fraction along the axis) were nearly the same for the two burner exit Reynolds numbers, x/d = 40-45, where x is the distance from the burner exit and d is the burner exit diameter. Nearly constant flame length in terms of x/d as the burner Reynolds number is varied is characteristic of turbulent jet flames with relatively small effects of buoyancy.

4.3 Results and Discussion

4.3.1 Mixture Fraction Structure

Measurements are still in progress but have been completed for the flame having a burner exit Reynolds number of 7400; therefore, results considered in the following will be limited to this flame. The features of the higher Reynolds number flame are very similar. In the following probability density functions,moments, and correlations and spectra of mixture fractions will be taken up in turn.

Mean and fluctuating mixture fractions along the axis are plotted in Fig. 23. Both time- and Favre-averaged properties are shown on the plot. Mean mixture fractions begin to decrease from unity near x/d = 10. Since the flow is fully developed turbulent pipe flow at the burner exit, this is somewhat farther downstream than might be expected, e.g., mean velocities for comparable conditions begin to decrease near x/d = 4 (Chuech et al., 1989). Two factors are primarily responsible for this behavior, as follows: (1) mixture fractions are uniform across the exit, unlike velocities, so that there is a potential core-like region for mixture fractions which defers its reduction from burner exit conditions in comparison to velocities, and (2) the central region of the flow is surrounded by a low density flame region which reduces the rate of entrainment into the central region and slows its mixing with the surroundings.

Table 6 Test Conditions for Nonluminous Turbulent Diffusion Flames[a]

Reynolds Number ($u_m d/\nu_o$)	7400	12700
Richardson Number (ad/u_o^2)	1.72×10^{-4}	5.75×10^{-5}
u_o (m/s)	20.05	34.66
Flow Rates (mg/s):		
Carbon Monoxide	691	1195
Hydrogen	14.3	24.8

[a]Flow directed vertically upward from a 7.04 mm diameter burner in still air at NTP. Initial mixture density of 0.905 kg/m^3 and viscosity of 1.738×10^{-5} kg/ms. Constant area burner passage, 40 diameters long, yielding nearly fully-developed turbulent pipe flow at the exit. Stoichiometric mixture fraction of the combined flow of carbon monoxide and hydrogen is 0.244.

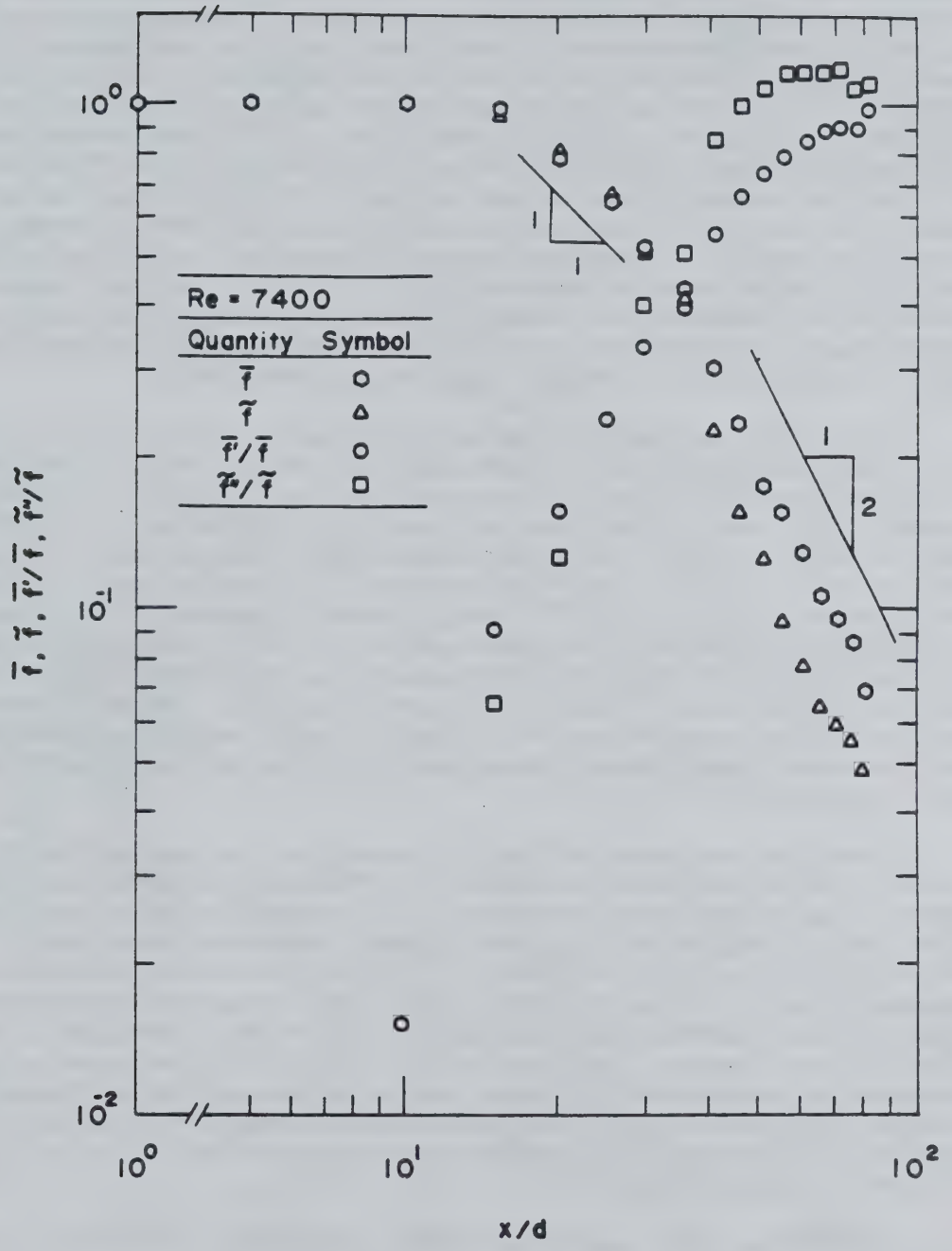

Figure 23 Favre- and time-averaged mean and fluctuating mixture fractions along the axis of a turbulent carbon monoxide/air diffusion flame: Re = 7400.

The tip of the flame is in the region x/d = 40-45, based on a mean stoichiometric mixture fraction long the axis of ca. 0.24 (which is the value representative of the combined carbon monoxide and hydrogen mixture at the burner exit). Before this region $\bar{f}$ and $\tilde{f} \sim x^{-1}$ but after this region $\bar{f} \sim x^{-2}$ with $\tilde{f}$ decreasing at a somewhat faster rate than $\bar{f}$. This behavior results from combined effects of buoyancy and the presence of large density variations in the flame. In the near burner region, effects of buoyancy are relatively small and the flow should scale similar to mixing from a forced jet: this implies $\bar{f} \sim x^{-1}$ as observed. Far from the burner exit the flow should approximate a weakly-buoyant plume where $\bar{f} \sim x^{-5/3}$: this is very close to the rate of decay observed for the recent flows beyond the flame tip with the somewhat higher rate of decay for the flame environment being attributable to effects of density variations in strongly-buoyant plumes. Near the burner exit, $\tilde{f}$ and $\bar{f}$ are essentially the same since the density of the flow is nearly constant in this region. In the region of the flame and beyond, however, $\tilde{f}$ is 30-50% lower than $\bar{f}$. The reason for this behavior is that density increases monotonically with decreasing mixture fraction in this region so that the higher values of mixture fraction are weighted downward when the density-weighted Favre average is computed. Naturally, $\bar{f} \approx \tilde{f}$ in the weakly-buoyant plume region far from the burner exit, however, present measurements were limited to $x/d \leq 80$ so that this far-field region could not be reached.

Mixture fraction fluctuation intensities are small near the burner exit, less than 1.5%. This is due to two factors: (1) reasonably good performance of the particle seeder and its compensation for slowly-varying seeding levels; and (2) the relatively weak sensitivity of f to variations of ρf near f=1, see Fig. 22. Beyond x/d = 10, however, the intensities of mixture fraction fluctuations increase rapidly, reaching values on the order of 100% near x/d = 80. $\tilde{f}''/\tilde{f}$ is up to 40% lower than $\bar{f}'/\bar{f}$ before the flame tip but behavior reverses beyond the flame tip with $\tilde{f}''/\tilde{f}$ being up to 40% larger than $\bar{f}'/\bar{f}$. The reason for this behavior is that $\tilde{f} \approx \bar{f}$ while Favre-averaged mixture fraction fluctuations are weighted downward due to lower densities near stoichiometric conditions before the tip of the flame. After the tip of the flame, $\tilde{f}''$ and $\bar{f}'$ are not very different so that the Favre-averaged intensity is greater largely because $\tilde{f} < \bar{f}$. Naturally, in the weakly-buoyant region, both intensities would be nearly the same but present measurements did not extend far enough to reach these conditions.

Radial profiles of mean and fluctuating mixture fractions are plotted in Fig. 24 as a function of r/x, the radial similarity variable for turbulent jets and plumes. Both time- and Favre-averaged properties are shown for x/d = 30, 40 and 50 which represent positions before, near and after the tip of the flame. The radial variations of mean mixture fractions are Gaussian in shape with flow widths of r/x = 0.18-0.20 which is typical of the flame-containing region of buoyant jet flames. Flow widths are somewhat wider in the flame region than in the overfire region which is also similar to past observations of turbulent diffusion flames (Jeng et al., 1982; Jeng and Faeth, 1984a). Flow widths are narrower for Favre-averaged than time-averaged mean mixture fractions since the low densities within the flame region tend to weight the mixture fractions downward. For example, r/x = 0.06 and 0.08 for the Favre- and time-averaged mixture fraction half widths for the range of test conditions illustrated in Fig. 24.

Mixture fraction fluctuations, normalized by the mean mixture fraction at the axis, exhibit greater variability with x/d than the normalized mean mixture fractions (see Fig. 24). Below the flame tip, at x/d = 30, mixture fraction fluctuations decrease near the axis due to reduced production in this region. Beyond the flame tip, however, mixture fraction fluctuations are highest at the axis due to enhanced instabilities, i.e., in this region, densities increase with increasing height above the burner which is a convectively unstable condition. The increasing levels of mixture fraction fluctuations with x/d parallel increases in radiation fluctuation intensities seen in the same region (Kounalakis et al., 1989), and are

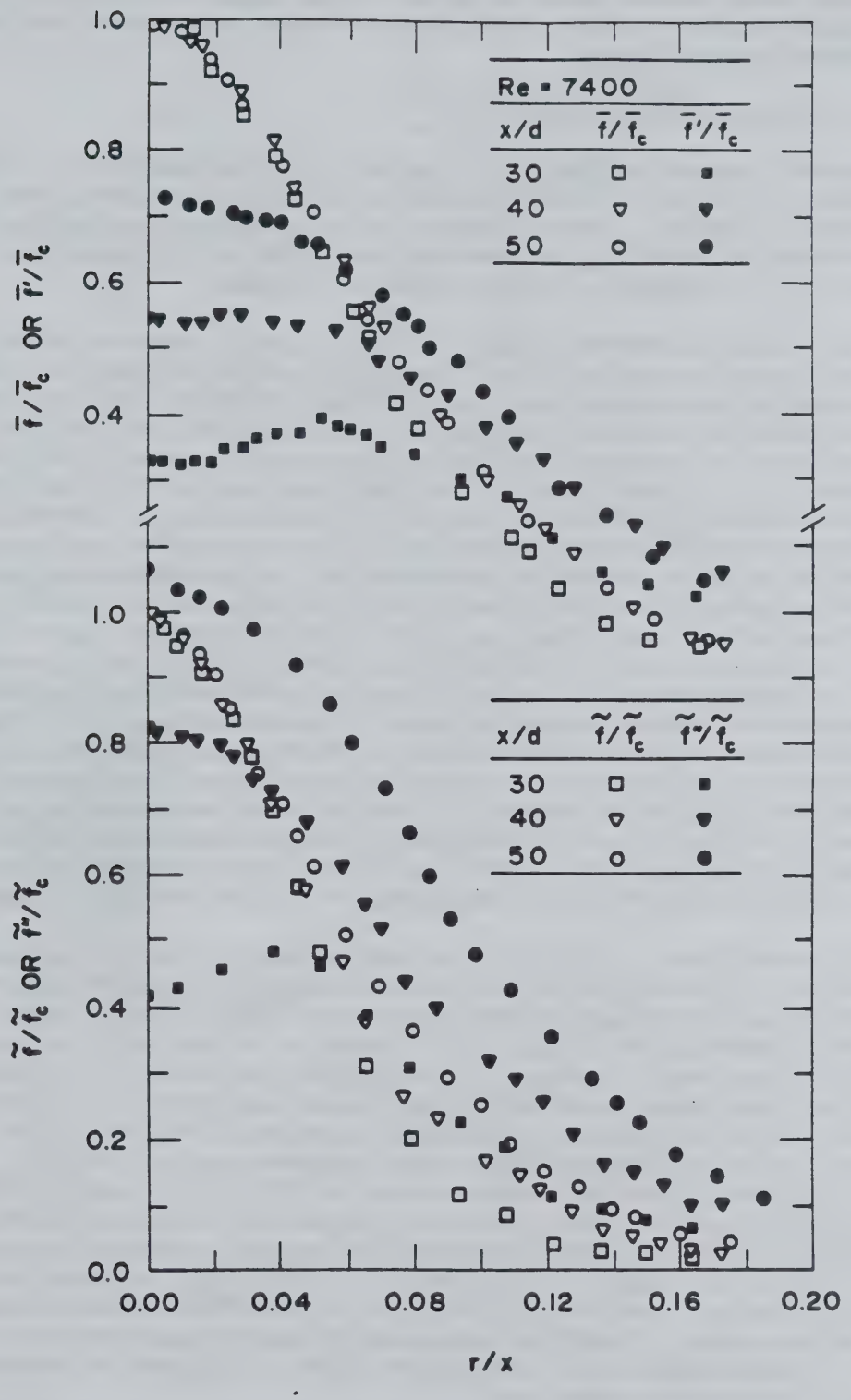

Figure 24 Radial profiles of Favre- and time-averaged mean and fluctuating mixture fractions for a turbulent carbon monoxide/air flame: Re = 7400.

probably largely responsible for them. Favre-averaged normalized mixture fraction fluctuations are larger than the corresponding time-averaged quantities throughout the flow field: the reasons for this behavior have already been discussed in connection with mixture fraction fluctuations along the axis.

4.3.2 PDF's of Mixture Fraction

Probability density functions of mixture fraction are illustrated in Figs. 25-27 for x/d = 30, 40 and 50. Both time- and Favre-averaged PDF's are plotted for various values of r/x at each axial position. Clipped-Gaussian distributions having mean and fluctuating values corresponding to the measurements are also plotted on the figures so that the capabilities of this PDF expression to fit the data can be evaluated.

None of the measurements of Figs. 25-27 exhibit a pure fuel spike at f=1, but all of them have air intermittency spikes at f=0. The magnitudes of the air spikes increase with increasing radial and streamwise distances, however, even the flow at x/d = 30 and r/x = 0 has an appreciable concentration of unmixed air. As f increases from zero, the PDF's decay at first in a region corresponding to the mixing superlayer, i.e., the region separating mixed turbulent fluid and pure ambient air. At positions far from the axis, this is the only region that is seen and the PDF decays monotonically with increasing f. Toward the axis, however, the PDF's exhibit a second peak at $f > 0$ which represents the local mixed fluid level corresponding to the degree of air entrainment into the mixture: this corresponds to regions where adjacent layers of fuel-rich and ambient air-rich gas are being mixed by fine-scale turbulence and molecular diffusion so that no region involves totally pure air or fuel. Naturally, near the burner exit this second peak would move toward f=1 and eventually merge into a fuel intermittency spike having a corresponding fuel-rich superlayer, however, present measurements were too far from the burner exit to observe this behavior. The main difference between the time- and Favre-averaged PDF's in the region of the present measurements is that the air intermittency spikes are higher for the Favre-averaged PDF's due to density weighting of the ambient air in comparison to lower densities within the stoichiometric region (the present carbon monoxide hydrogen flames have a stoichiometric mixture fraction of 0.244, as noted earlier). Additionally, the second peak shifts toward f=0 for the Favre-averaged PDF's if this peak occurs at $f < 0.244$, for the same reasons.

The clipped-Gaussian PDF's yield a fair correlation of both the measured time- and Favre-averaged PDF's in Figs. 25-27. In general, discrepancies between measured and correlated PDF's are comparable to earlier observations of PDF's in nearly constant density adiabatic wall plumes (Lai and Faeth, 1987). Thus effects of large density variations do not appear to be particularly important. The clipped-Gaussian function also provides for the air and fuel intermittency spikes and the intermediate peak in the PDF's, in a relatively natural way. However, the form of the clipped-Gaussian PDF cannot represent the decaying region in the mixing superlayer near the air intermittency spike. This is potentially troublesome because underestimation of PDF's in the superlayer implies overestimation of the PDF elsewhere since the integral of the function must be unity. These combined effects tend to focus the greatest discrepancies between the measured and correlated PDF's in the region $0 < f \leq 0.4$ which also corresponds to the stoichiometric region of most fuels and can have a significant influence on flame radiation properties. Thus earlier assessment of the relative insensitivity of flame structure predictions to the properties of mixture fraction PDF (Lockwood and Naguib, 1975) may not be pertinent to predictions of flame radiation properties.

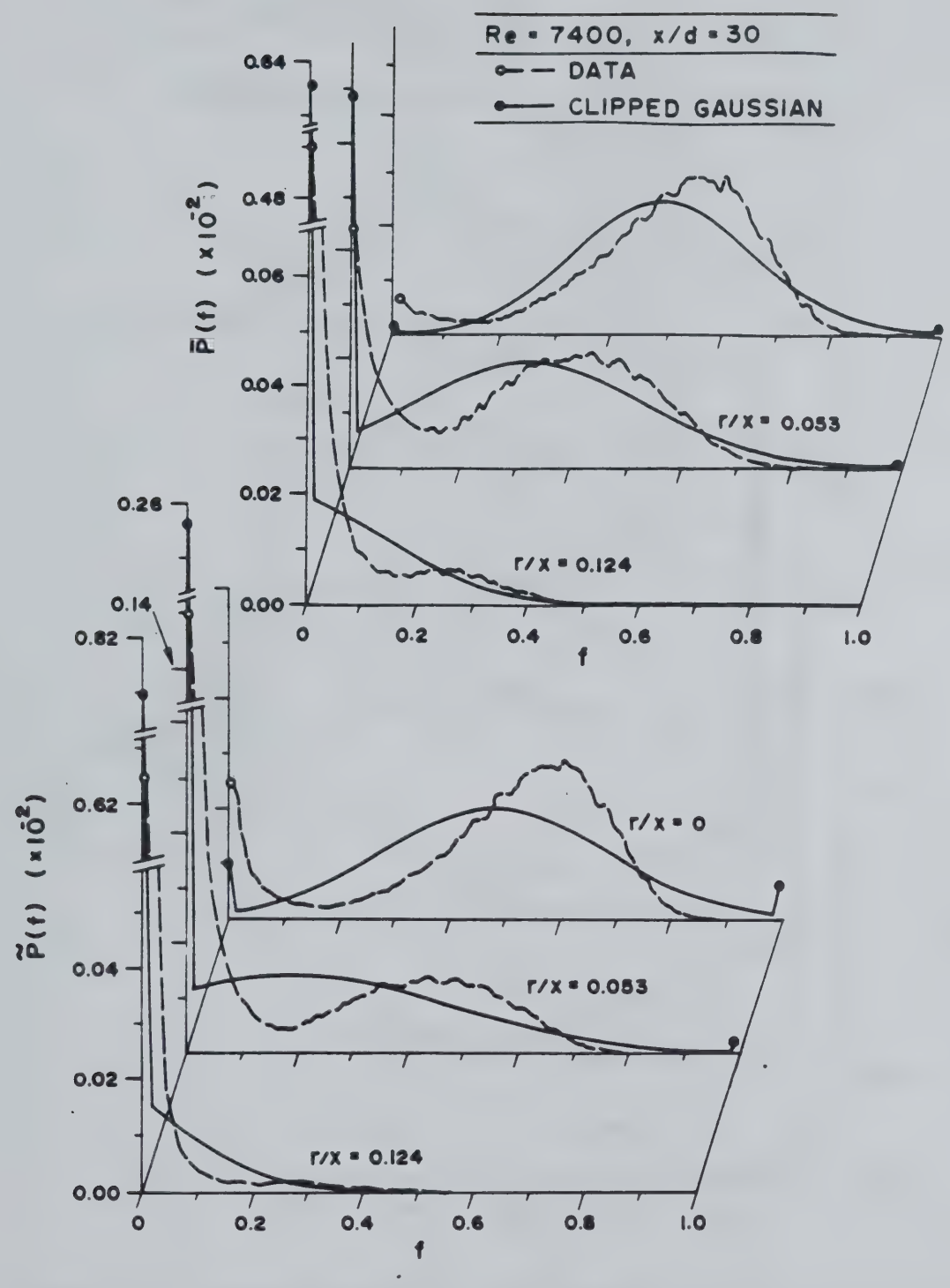

Figure 25 Favre- and time-averaged PDF's of mixture fraction in a turbulent carbon monoxide/air diffusion flame: Re = 7400, x/d = 30.

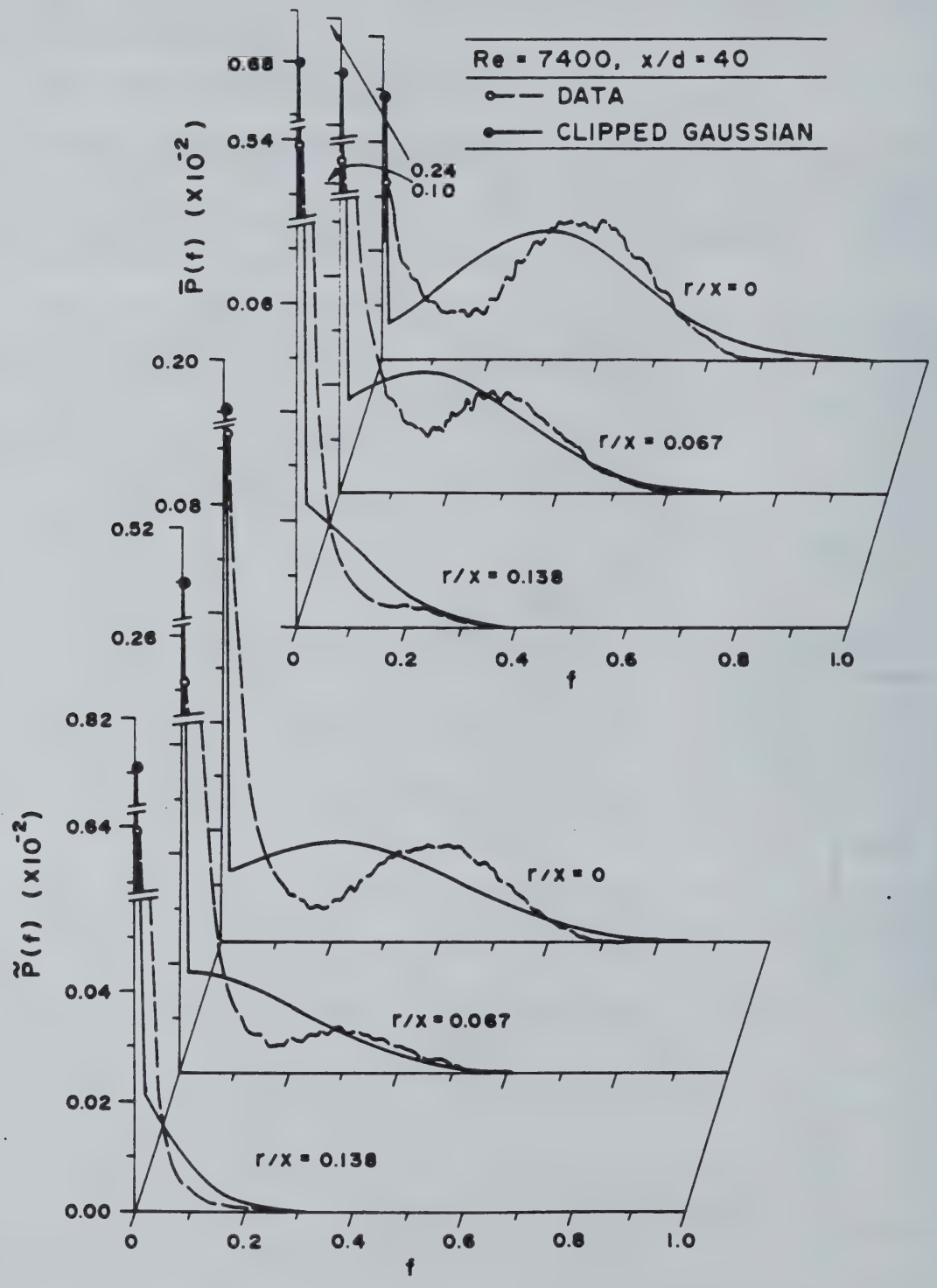

Figure 26 Favre- and time-averaged PDF's of mixture fraction in a turbulent carbon monoxide/air diffusion flame: Re = 7400, x/d = 40.

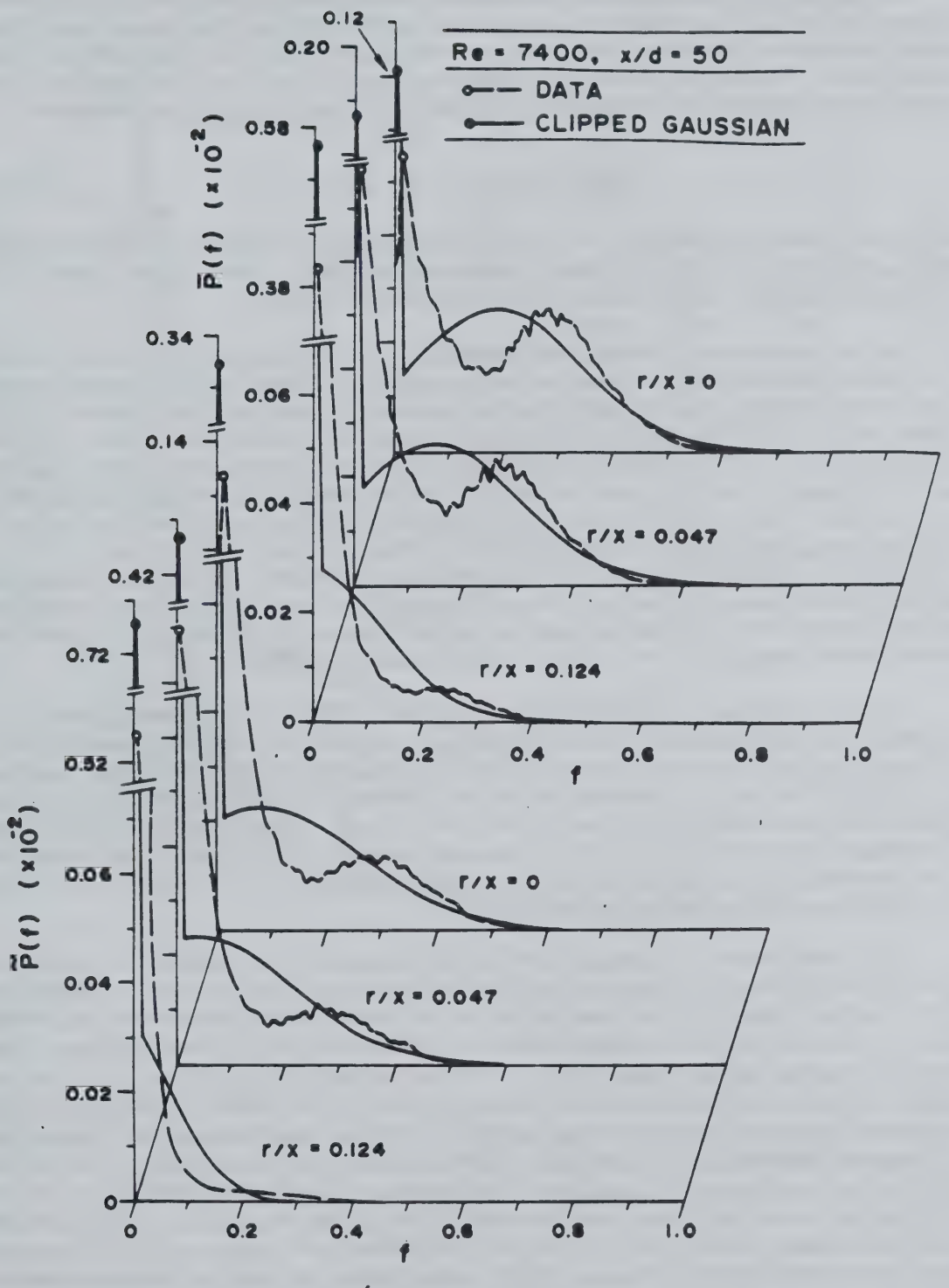

Figure 27 Favre- and time-averaged PDF's of mixture fraction in a turbulent carbon monoxide/air diffusion flame: Re = 7400, x/d = 50.

4.3.3 Correlations and Spectra of Mixture Fractions

Measured time-averaged temporal correlations of mixture fraction fluctuations are illustrated in Fig. 28. The results are plotted as a function of delay time normalized by the integral time scale of the correlations (values of the integral time scales themselves will be taken up later). Results are shown for various values of r/x at x/d = 30, 40 and 50. As a baseline, exponential fits of the correlations are shown for each height above the burner

$$\overline{f'(t)f'(t+\tau)} / \overline{f}'^2 = \exp(-\tau / \tau_I) \qquad (24)$$

This type of correlation yielded a reasonably good fit of the measurements of Becker et al. (1967) and Birch et al. (1978) for nearly constant density jets. Naturally, the shape of the correlation of equation (24) is identical at all values of x/d in Fig. 28.

All of the measured correlations illustrated in Fig. 28 decay monotonically to zero as τ increases. Remarkably, the correlations are relatively independent of r/x at each height above the burner exit. Recognizing that the exponential expression of equation (24) is independent of x/d shows that the correlations progressively become sharper near $\tau / \tau_I = 0$ as x/d increases. The behavior is probably due to the fact that we are able to resolve the fine-scale features of the flow better as length scales increase with increasing height above the burner exit. These features cause the correlation to decrease rapidly near $\tau=0$ so that a simple exponential decay provides a poorer correlation of the measurements. This is awkward since the exponential form vastly simplifies computations during time-dependent stochastic simulations of flow properties (Kounalakis et al., 1989). Fortunately, the resulting errors of the simulation are confined to high frequencies which generally contain a relatively small proportion of the signal energy of radiation fluctuations.

A more convenient picture of the low frequency effects that are most important for computations of turbulence/radiation interactions can be obtained from the temporal spectra of mixture fraction fluctuations plotted in Fig. 29. These results are for positions along the axis at x/d = 30, 40 and 50, however, the results illustrated in Fig. 28 show that findings at the axis are representative for all radial positions as well. The properties of Fig. 29 are time-averaged quantities that have been normalized using $\overline{f}'$ and τ_I. The Fourier transform of the exponentially decaying temporal correlation, equation (24), is also plotted on the figure for comparison with the measurements.

The measurements illustrated in Fig. 29 are essentially independent of x/d except at high frequencies where the spectra decay more rapidly as x/d decreases. As discussed earlier, this behavior is felt to be an artifact of the measurements where the small-scale features of the flow are resolved better farther from the burner exit. The measurements also display an inertial regime where $E(n) \sim n^{-5/3}$, within the inertial regime results for the various axial stations are correlated unusually well. The Fourier transform of the exponential correlation provides a reasonable fit of the measurements at low frequencies and the break frequency of the spectrum. However, the fit of the decaying portion of the spectra is less satisfactory. In particular, the exponential correlation yields $E(n) \sim n^{-2}$ in this region which differs from proper behavior in the inertial region and cannot represent cutoff of the spectra as the smallest scales of the turbulence are approached. This behavior at high frequencies probably accounts for the overestimation of radiation fluctuation spectra at high frequencies, based on the use of an exponentially decaying correlation, for hydrogen/air and carbon monoxide/air flames during earlier work in this laboratory (Kounalakis et al., 1988, 1989).

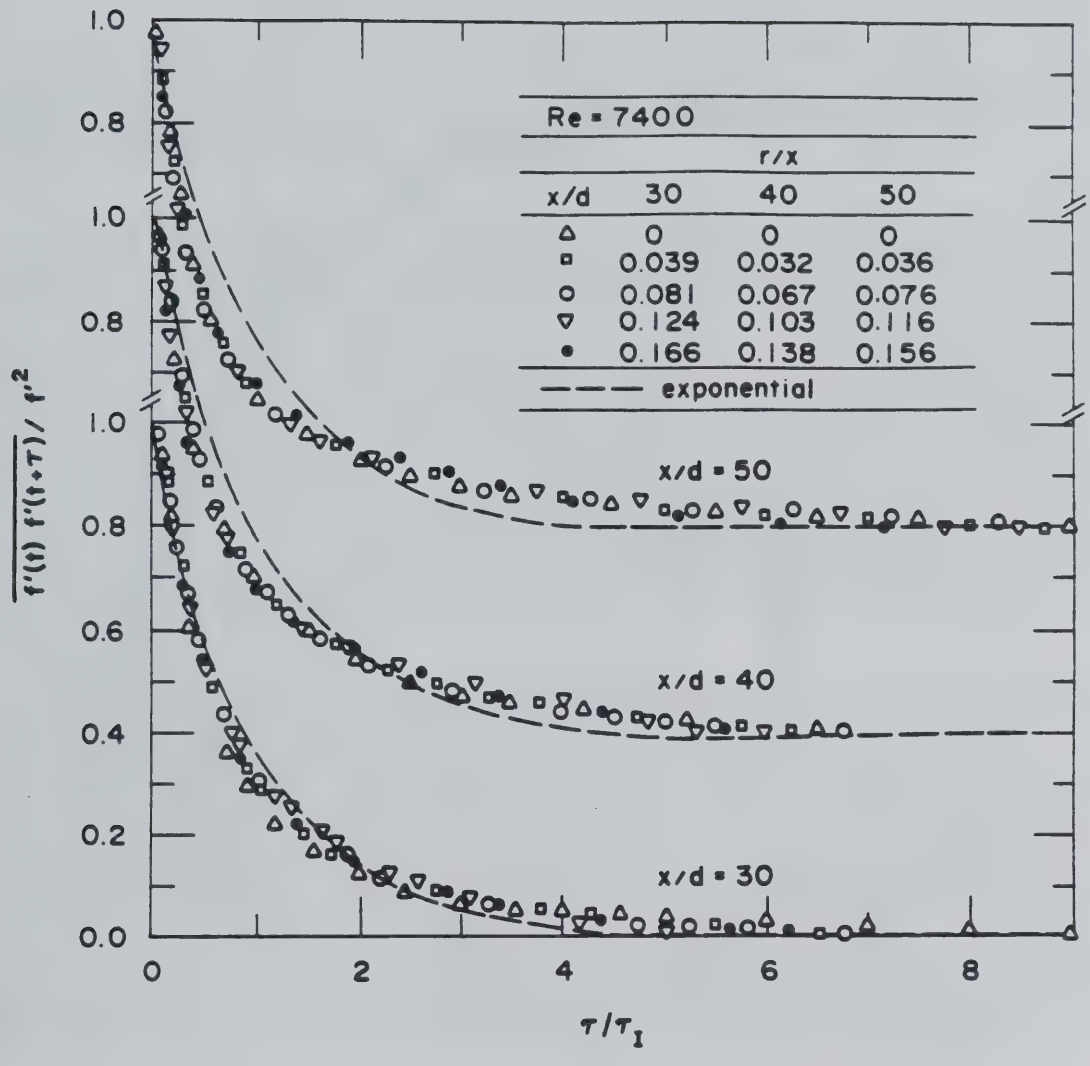

Figure 28 Time-averaged temporal correlations of mixture fraction fluctuations in a turbulent carbon monoxide/air diffusion flame: Re = 7400.

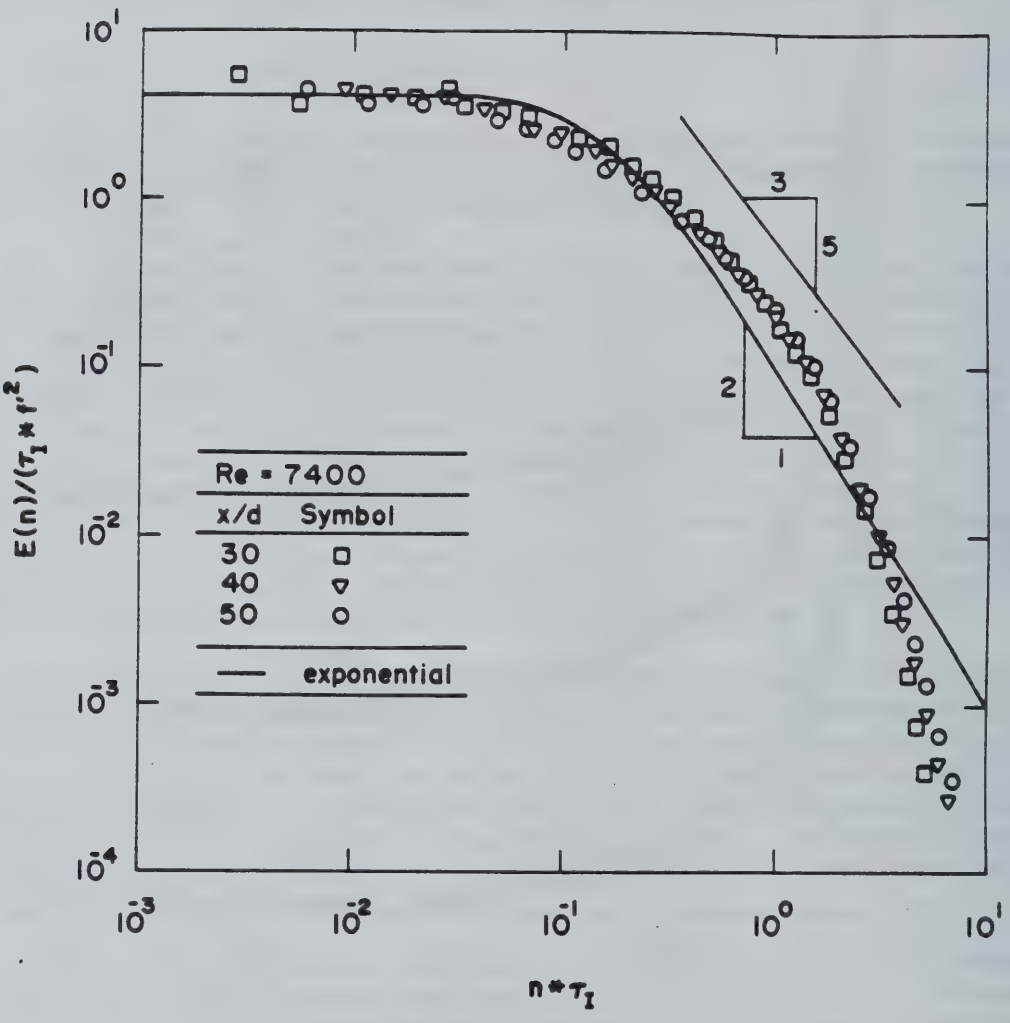

Figure 29 Time-averaged power spectral densities of mixture fraction fluctuations along the axis of a turbulent carbon monoxide diffusion flame: Re = 7400.

The time-averaged, two-point spatial correlations of mixture fraction fluctuations for horizontal radial paths through the axis, $\overline{f'(r)f'(r+\Delta r)} / \overline{f'(r)\ f'(r+\Delta r)}$, are plotted as a function of $\Delta r/\Lambda_r$, where Λ_r is the spatial radial integral scale and Δr is the distance between points, in Fig. 30. Results for various radial positions are plotted for x/d = 30, 40 and 50. The correlations are compared with an exponential fit, as follows:

$$\overline{f'(r)f'(r+\Delta r)} / \overline{f'(r)\ f'(r+\Delta r)} = \exp(-\Delta r/\Lambda_r) \qquad (25)$$

As noted earlier, this type of correlation is particularly useful for numerical simulations of mixture fraction variations along a radial path since the number of points that must be retained is vastly reduced for exponential correlations.

The spatial correlations illustrated in Fig. 30 exhibit remarkably little variation with radial position at a particular value of x/d, in spite of increased effects of intermittency near the edge of the flow. Recognizing that the exponential approximation is invariant when plotted in the coordinates of Fig. 30, it is also clear that the correlations are relatively independent of x/d as well. Additionally, the exponential fit of equation (25) provides a reasonably good correlation of the measurements at all positions. Some exceptions can be seen at the highest position, x/d = 50, where the correlation decreases more rapidly than the exponential decay near $\Delta r = 0$. As before, this behavior is an artifact of the measurements due to improved spatial resolution with increasing x/d. In fact, the exponential decay is always somewhat in error since it cannot represent the cutoff at the smallest scales of the flow and only provides a good fit at very large Reynolds numbers or when the measurements cannot resolve the smallest scales. Nevertheless, the exponential expression provides a good representation of the largest scales which have the greatest influence on turbulence/radiation interactions.

One matter for concern about the results illustrated in Fig. 30 is that the present two-point spatial correlations do not exhibit the Frenkiel function shape observed by Corrsin and Uberoi (1951) and Becker et al. (1967) for symmetric spatial correlations in nearly constant density jets (The Frenkiel function involves the correlation becoming negative for a time, reaching values on the order of -0.1 and then decaying to zero from the negative side). Only a slight tendency for this behavior was observed near the axis, r/x = 0.0 and 0.042, at x/d = 30, where the correlations reached values on the order of -0.05. This region is dominated by forced jet properties and small density changes; therefore, it is closest to the properties of the flows considered by Corrsin and Uberoi (1951) and Becker et al. (1967). Thus, effects of buoyancy and variable properties may explain the differences between the present results for flames and the earlier results for constant density jets but more measurements will be needed in buoyant flows to resolve the issue.

The temporal and spatial integral scales of the jet diffusion flame are plotted as a function of r/x in Fig. 31 for x/d = 30, 40 and 50. The scales are normalized as $\tau_i\ u_m/(x-x_o)$, where u_m is the averaged velocity at the burner exit and x_o is a virtual origin, and Λ_r/x. The virtual origin for the temporal integral scales was found to be $x_o/d = 13$. When correlated in this manner, the measurements tend to collapse into single curves in spite of the range of flame positions and vastly different values of scalar properties at various points in the present flows.

Within experimental uncertainties, spatial integral scales are proportional to the distance from the burner exit and relatively independent of radial position in the flames. A reasonable correlation of the measurements of Fig. 31 is

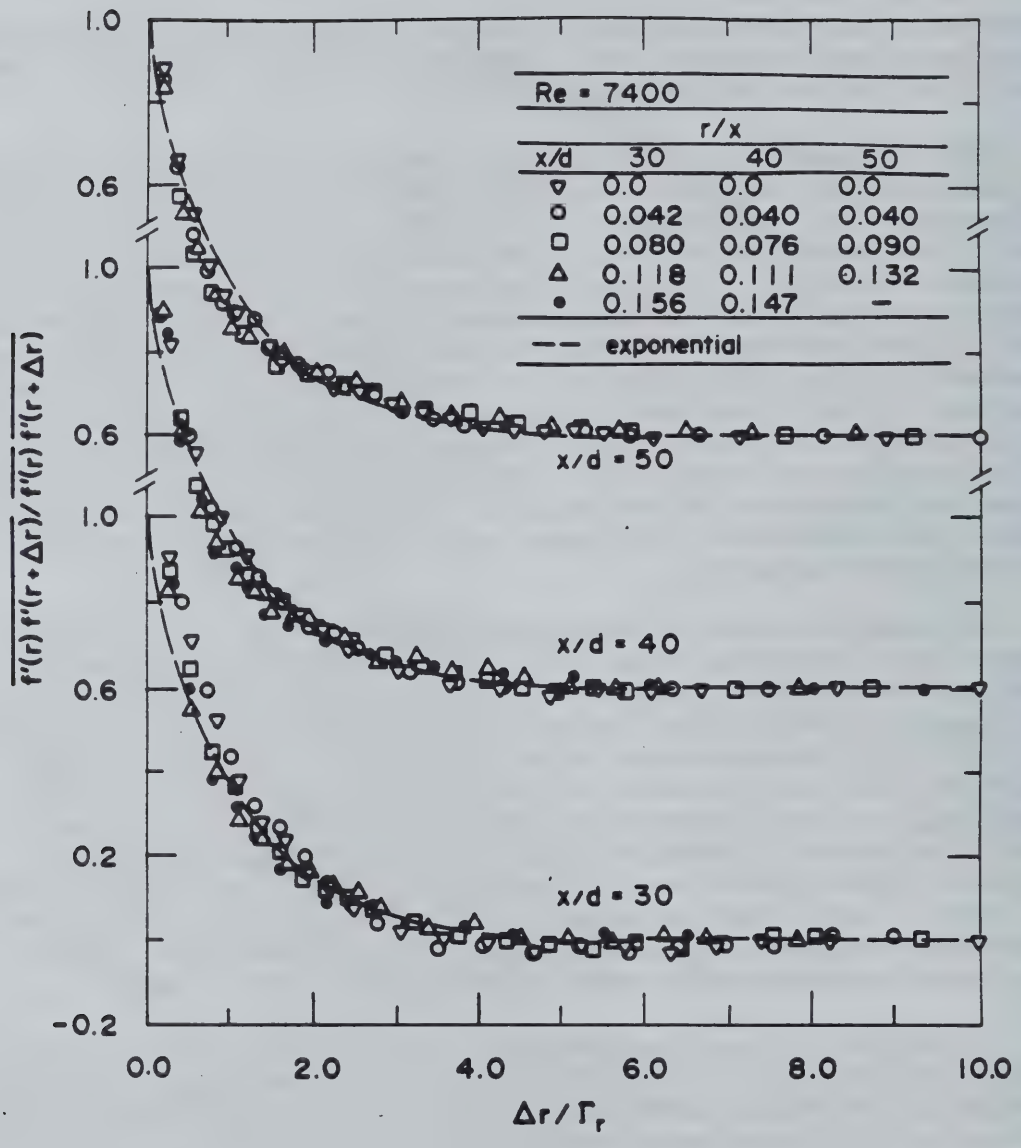

Figure 30 Time-averaged spatial correlations of mixture fraction fluctuations in a turbulent carbon monoxide/air diffusion flame: Re = 7400.

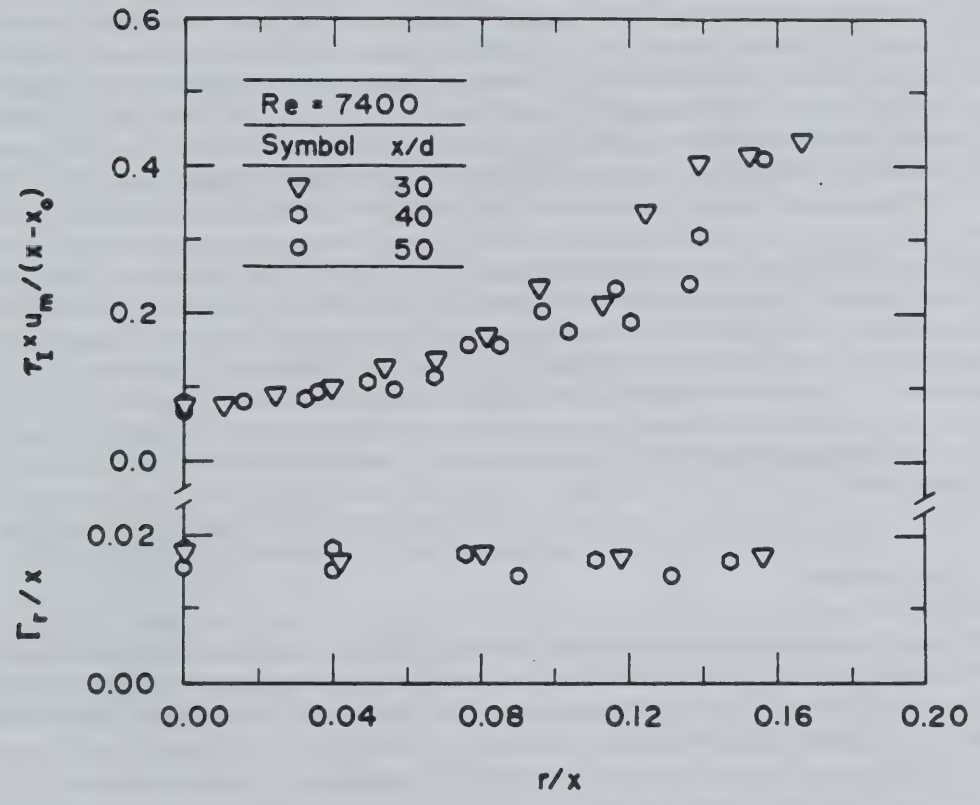

Figure 31 Temporal and spatial integral scales in a turbulent carbon monoxide/air diffusion flame: Re = 7400.

$$\Lambda_r/x = 0.017 \qquad (26)$$

For comparison, Becker et al. (1967) find the streamwise integral scale of mixture fraction fluctuations at the axis to be $\Lambda_r/x = 0.044$ while their radial integral scale is much smaller due to the Frenkiel function shape of the crosstream spatial correlations, perhaps $\Lambda_r/x \approx 0.01$ (crudely estimated from their plots). Thus, the present correlation of equation (26) is roughly twice that of Becker et al. (1967)—largely due to the exponential rather than Frenkiel function shape of the correlation observed during the present measurements.

The temporal integral scale correlation of Fig. 31 shows that τ_I is smallest at the axis. This behavior is a manifestation of Taylor's hypothesis; namely length scales are relatively uniform across the flow, mean velocities are highest at the axis, and $\tau_I \sim \Lambda_r/\overline{u}$ from Taylor's hypothesis assuming that the streamwise and crosstream spatial integral scales are proportional to one another. The correlation of τ_I is relatively independent of x/d near the axis, even for positions before, near and after the flame tip. However, the correlation becomes more scattered near the edge of the flow with results for x/d = 30 differing somewhat from x/d = 40 and 50 which are similar to each other. This effect may be due to buoyancy in the presence of a flame. Near the axis, the flow is primarily dominated by jet momentum and apparently density variations due to the flame have a relatively small effect at these conditions. In contrast, properties off-axis are more dominated by buoyancy so that the only streamwise position where the flame is present off the axis, x/d = 30, yields results which are different from the rest. In general terms, however, the variations of temporal integral scale with radial distance are similar to observations in constant-density jets (Birch et al., 1978; Pitts and Kashiwagi, 1984). Quantitative assessment of streamwise spatial scales and effects of buoyancy will require additional measurements at different Reynolds numbers as well as measurements of velocities.

4.4 Conclusions

Instantaneous mixture fractions, at single points as well as two points along radial paths through the axis, were measured in turbulent carbon monoxide diffusion flames burning in still air. Burner Reynolds numbers were 7400 and 12700 with burner exit Richardson numbers of ca. 10^{-4} and flame lengths (based on mean stoichiometric mixture fractions along the axis) of 40-45 burner exit diameters. Thus, the test flames were primarily turbulent jet flames with effects of buoyancy near the edge of the flames since the surroundings were still. Measurements and interpretation of the results are still in progress: present results focussed on findings for the flame having a burner exit Reynolds number of 7400. The main conclusions of the study, thus far, are as follows:

1. There are significant differences (up to 50% near the flame tip) between time- and Favre-averaged mean mixture fractions and intensities of mixture fraction fluctuations. In general, time-averaged mean mixture fractions are greater than Favre-averaged mean mixture fractions since the latter are weighted downward due to low densities in the region of flame.

2. Both time- and Favre-averaged PDF's of mixture fractions correlated reasonably well as clipped-Gaussian functions, except for the mixture fraction superlayer near the air intermittency spike where measured probability densities were generally greater than predicted. This deficiency is potentially problematical for stochastic simulation of mixture fraction

distributions since this region includes the stoichiometric mixture fractions where contributions to flame radiation are largest.

3. Temporal correlations of mixture fraction fluctuations were approximated reasonably well as decaying exponential functions in terms of time normalized by the integral time scale. This simplified form, however, is largely due to the inability of present measurements to resolve the smallest scales of the flow and departures from the correlation were observed at large x/d where experimental spatial resolution was improved. Nevertheless, stochastic simulations of mixture fractions for radiation predictions are most sensitive to large-scale effects that can be represented by the exponential approximation.

4. Spatial correlations of mixture fraction fluctuations also approximated decaying exponential functions of separation distance divided by the spatial integral scale, subject to deficiencies at small scales similar to the temporal correlations. This behavior is rather remarkable in view of expected effects of intermittency near the edge of the flow.

5. Radial spatial integral scales were also independent of radial position and could be correlated as $\Lambda_r/x = 0.017$. In view of the absence of theories to describe two-point properties of this type in high Reynolds number turbulent flows, the simplicity of this expression within flames will be helpful for near-term estimates of turbulence/radiation interactions.

6. Temporal integral scales also exhibited relatively simple correlations in the flames, with behavior generally as expected based on Taylor's hypothesis. Rational correlation of temporal integral scales, however, must await additional information on the velocity structure of the present test flames.

This is a report of work in progress. Current experiments are examining the effect of burner exit Reynolds numbers on mixture fraction structure while future measurements of the mean and fluctuating radiation properties and velocity structure, as well as computations of flame properties using methods developed earlier in this laboratory, are planned. With the completion of this work, many outstanding issues concerning turbulence/radiation interactions can be addressed.

5. RADIATION FROM LUMINOUS TURBULENT FLAMES

5.1 Introduction

Similar to other properties of turbulent diffusion flames, radiation emitted from the flame varies with time even when mean properties are statistically stationary. This is a direct manifestation of turbulence/radiation interactions. There are many effects of turbulence/radiation interactions but perhaps the most important is that they cause mean radiation levels from turbulent flames to be biased upward from estimates based on mean scalar properties in the flames. Flame radiation fluctuations are a direct manifestation of the nonlinearities that cause mean radiation levels to be biased in this manner; therefore, studying radiation fluctuations provides information needed to better understand turbulence/radiation interactions, similar to the information provided by velocity and scalar property fluctuations when a better understanding of turbulent mixing is sought. Motivated by these observations, this phase of the investigation is examining radiation fluctuations from luminous turbulent diffusion flames—both theoretically and experimentally. This is a

progress report and only measurements of mean and fluctuating continuum radiation properties from soot have been completed thus far; therefore, the following discussion will be limited to these findings.

Turbulence/radiation interactions in nonpremixed turbulent flames have attracted attention in the past. Cox (1977) and Kabashnikov and Kmit (1979) used simplified models to show that turbulent fluctuations increase mean radiation levels from estimates based on mean scalar properties. Grosshandler and Vantelon (1985) developed an approximate model to compute effects of turbulent fluctuations on mean radiation properties, recently applied to ethanol pool fires by Fisher et al. (1987), drawing similar conclusions. Portscht (1974) reported early measurements of power spectral densities of the output of several flame radiation detectors that were viewing buoyant turbulent diffusion flames: the results showed the presence of large radiation fluctuations in comparison to mean radiation levels (large radiation fluctuation intensities), experimentally demonstrating the importance of turbulence/radiation interactions. Later, Markstein (1981) used a scanning radiometer to measure fluctuations in PMMA pool fires and reported a number of turbulent radiation properties analogous to other turbulence properties, e.g., intermittency, fluctuation intensities, kurtosis and spatial correlations.

The radiation properties of nonluminous and luminous turbulent diffusion flames have also been studied in this laboratory. The experiments involved buoyant jet diffusion flames burning in still air, considering the following fuels: hydrogen (Gore et al., 1987c; Sivathanu et al., 1987), carbon monoxide (Gore et al., 1987b), methane (Jeng et al., 1984; Jeng and Faeth, 1984a), natural gas (Gore et al., 1987a), ethylene (Gore and Faeth, 1986) and acetylene (Gore and Faeth, 1987). A time-independent stochastic method for treating turbulence/radiation interactions was developed which yielded encouraging agreement with measurements of mean spectral radiation intensities and radiative heat fluxes. It was found that turbulence/radiation interactions generally caused significant (more than 100 percent) increases of mean radiation levels above estimates based on mean scalar properties, although this effect was small for some nonluminous flame systems, e.g., carbon monoxide, methane and natural gas/air flames.

The initial phases of the present investigation considered mean and fluctuating spectral radiation intensities from nonluminous turbulent hydrogen and carbon monoxide diffusion flames burning in still air (Kounalakis et al., 1988, 1989). Measurements were made of mean and fluctuating values, probability density functions and temporal power spectral densities of spectral radiation intensities for horizontal chord-like paths through the axis of flames having various initial Reynolds numbers. Flame properties were predicted based on stochastic simulation of mixture fraction properties along the radiation path following Box and Jenkins (1976), use of the laminar flamelet concept to find all other scalar properties along the path from state relationships, and a narrow-band radiation model (Ludwig et al., 1973; Grosshandler, 1980) to compute spectral radiation intensities for each realization of scalar properties along the radiation path. Encouraging agreement was found between predicted and measured mean and fluctuating spectral radiation intensities, in spite of the significant uncertainties concerning the statistical properties of mixture fraction fluctuations that were discussed in Section 4 of the present report. Radiation fluctuation intensities in the range 20-110% were observed, providing additional direct evidence of effects of turbulence/radiation interactions in nonluminous turbulent diffusion flames.

The objective of the present investigation was to extend the work of Kounalakis et al. (1988, 1989) from nonluminous flames to continuum radiation from soot in luminous flames. The overall goal is to carry out numerical simulations of continuum radiation properties and to evaluate predictions with measurements. However, work thus far has been limited to measurements and the present report will be confined to these findings. The

new measurements involved mean and fluctuating spectral radiation intensities in the continuum for horizontal paths through the axis of turbulent acetylene and propylene diffusion flames burning in still air. The flame configurations involved highly-buoyant pool-like fires.

The report of this phase of the study begins with a description of experimental methods. Results are then considered, treating moments, probability density functions and temporal power spectral densities of spectral radiation intensities, in turn. This section of the report closes with the conclusions that can be drawn from the findings thus far.

5.2 Experimental Methods

5.2.1 Apparatus

The test apparatus was identical to the arrangement used for measurements of correlations between temperatures and soot volume fractions, described in Section 3 of this report. This involves vertically upward injection of fuel within an enclosure ($2.4 \times 2.4 \times 3.6$ m high) constructed of plastic strips and having a metal hood and adjustable exhaust system at the top to remove the combustion products (see Fig. 9). A smaller screened enclosure ($1 \times 1 \times 2$ m high) was positioned directly around the burner to further reduce effects of room disturbances. Instrumentation was mounted rigidly; therefore, the burner was traversed to access various points within the flame.

A sketch of the burner appears in Fig. 10. The burner was water-cooled with the fuel flow directed vertically upward. The burner exit was 50 mm in diameter. The flames attached naturally at the exit of the burner.

5.2.2 Instrumentation

Structure measurements for these flames will include the statistical properties of soot volume fractions and spectral radiation intensities along horizontal radial paths through the flames. Additionally, correlations between soot volume fractions and temperatures are known from Sivathanu and Faeth (1989a,b). Measurements completed thus far, however, have been limited to spectral radiation intensities and the following description will be limited to this system.

Spectral radiation intensities were measured for horizontal radial paths through the flames at various heights above the burner exit. Three fields of view were used, having diameters of 5, 10 and 20 mm at the flame axis and field angles of 0.6, 1.2 and 2.4 degrees. The three optical path diameters were used to estimate effects of spatial broadening since the integral scales of the test flames will not be known until the statistical properties of soot volume fractions have been measured.

A 125 mm low resolution monochromator (Oriel Model 7240) and a PbS detector (New England Photomultiplier, Series E2) operating at room temperature, were used for the measurements. Signal-to-noise ratios were improved using a chopper operating at 900 Hz with the detector output bandwidth limited by a second-order low-pass filter having a break frequency of 400 Hz. A combination of order-sorting filters and gratings yielded observations in the 1200-6000 nm wavelength range. The monochromator/detector system was calibrated at several temperatures, to assure system linearity, using a blackbody source (Infrared Industries, Model 463). Wavelength readings were calibrated using a narrow line filter and the black-body source. Experimental uncertainties (95 percent confidence) of these measurements were less than 20 percent, and were repeatable within this range.

Measurements of spectral radiation intensity fluctuations were limited to 1000 and 2300 nm (with a resolution of 40 nm at half-peak transmission). Acetylene/air and propylene/air flames were considered during the experiments, neither of which have significant gas band radiation at these wavelengths; therefore, the measurements yielded only the continuum radiation properties of soot. Assuming that soot acts like a blackbody implies that the maximum in the spectral distribution of radiation intensity is at λ_{max}, where $\lambda_{max}T = 2898$ μm K, from Wien's displacement law (Incropera and DeWitt, 1981). Maximum flame temperatures for these fuels are in the range 1500-1800 K which implies λ_{max} in the range 1600-1900 nm; therefore, the two test wavelengths are on the rising and falling portions of the Planck distribution with increasing wavelengths but sufficiently near the peak to yield strong radiation signals and good signal-to-noise ratios (on the order of 10^3).

5.2.3 Test Conditions

Test conditions were also identical to the flames considered for the temperature/soot volume fraction correlation study. This included acetylene/air flames having burner exit Reynolds numbers of 470 and 840; and propylene/air flames having burner exit Reynolds numbers of 750 and 1370. The properties of these flames are summarized in Table 4. The flames corresponded to pool-like fires with flame heights in the range 8-14.4 and burner exit Richardson numbers in the range 40-62. Flame residence times were in the range 257-600 ms, which are sufficiently long to be in the long residence-time regime where soot generation efficiencies are independent of burner operating conditions.

5.3 Results and Discussion

5.3.1 Mean and Fluctuating Spectral Radiation Intensities

Measured mean and fluctuating spectral radiation intensities for horizontal radiation paths through the axis of turbulent acetylene and propylene flames burning in still air are summarized in Table 7. Results are presented for x/d = 3.4, 4.7 and 6.7 which is in the flaming portion of the flow (flame heights were at x/d = 8-11 for the acetylene/air flames and x/d = 10.8-14.4 for the propylene/air flames). Results include both wavelengths, 1000 and 2300 nm, generally for an optical path diameter of 10 mm; however, optical path diameters of 5 and 20 mm are also considered for acetylene at a wavelength of 2300 nm.

Mean spectral radiation intensities are higher at 2300 nm than 1000 nm. This behavior is expected since underfire soot within the luminous region of the flames generally has temperatures in the range 1300-1800 K for present test conditions (Sivathanu et al., 1989b) which implies maximum spectral radiation intensities in the range 1600-2200 nm, i.e., nearer to the 2300 nm wavelength. Mean spectral radiation intensities decrease monotonically with increasing optical path diameter. This simply reflects gradient broadening since mean radiation levels decrease with increasing radial distance. Richardson extrapolation of the results, however, suggests that mean spectral radiation intensities for an infinitely-small diameter path through the axis would differ from the values for 5-10 mm diameter paths by only 2-5%. Mean spectral radiation intensities are higher for acetylene than propylene since acetylene has a higher radiative heat loss fraction due to its higher soot concentrations (see Table 4). The variation of mean spectral radiation intensities with streamwise distance is relatively complex, sometimes increasing and sometimes decreasing: this reflects the mixing properties of the flames which is not a major issue for the present investigation (see Gore and Faeth, 1986, 1987 for consideration of the

Table 7 Mean and Fluctuating Spectral Radiation Intensities in the Continuum

Re	x/d	λ (nm)	d_{opt} (mm)	$\bar{i}_\lambda$ (kW/m^{2}sr μm)	$\bar{i}_\lambda'/\bar{i}_\lambda$ (%)
Acetylene/Air Diffusion Flames:					
470	3.4	1000	10	1.67	96
	4.7		10	1.59	87
	6.7		10	0.64	145
840	3.4	1000	10	2.74	51
	4.7		10	2.68	59
	6.7		10	1.48	91
470	3.4	2300	10	4.39	71
	4.7		10	3.78	85
	6.7		5	2.00	126
	6.7		10	1.91	119
	6.7		20	1.51	129
840	3.4	2300	10	5.62	54
	4.7		10	6.33	59
	6.7		5	5.06	75
	6.7		10	5.11	66
	6.7		20	4.33	83
Propylene/Air Diffusion Flames:					
750	3.4	1000	10	1.35	67
	4.7			1.39	72
	6.7			1.17	85
1370	3.4	1000	10	1.46	129
	4.7			1.58	62
	6.7			1.73	61
750	3.4	2300	10	2.41	66
	4.7			2.72	70
	6.7			2.03	94
1370	3.4	2300	10	2.87	52
	4.7			3.56	49
	6.7			3.75	57

variation of spectral radiation intensities with height above the burner for luminous buoyant jet diffusion flames).

Radiation fluctuation intensities in Table 7 vary in the range 54-145% and generally increase with increasing height above the burner. These magnitudes and trends are generally similar to earlier findings for nonluminous flames (Kounalakis et al., 1988, 1989); however, radiation fluctuations are generally higher for the luminous flames. The results clearly indicate that effects of turbulence/radiation interactions are important for luminous flames, i.e., with radiation fluctuations of this magnitude it is unlikely that some simple averaging procedure can account for a nonlinear process like radiation.

5.3.2 PDF's of Spectral Radiation Intensities

The effect of optical path diameter on the PDF's of spectral radiation intensities can be seen from the results plotted in Fig. 32. This plot involves PDF's of spectral radiation intensities at a wavelength of 2300 nm for optical path diameters of 5, 10 and 20 mm. The results were obtained in the two acetylene/air flames at x/d = 6.7; however, findings for other conditions were similar. The PDF's exhibit a spike at the minimum radiation level, reminiscent of radiation intermittency, with a Gaussian-like shape for spectral radiation intensities greater than the mean. Similar to the moments of spectral radiation, discussed in connection with Table 7, results for the 5 and 10 mm diameter optical paths are nearly the same. However, results for the 20 mm diameter optical path exhibit a significantly greater spike than the rest, indicative of excessive effects of gradient broadening.

Some representative PDF's of spectral radiation intensities for various positions in both acetylene and propylene flames are illustrated in Figs. 33 and 34. These results are for optical path diameters of 10 mm, which are reasonably representative of infinitely small path diameters, based on the results of Fig. 32. One of the most interesting features of these results is the large spike that appears at low radiation levels. In general, the magnitude of the spike increases with increasing height above the burner; it is more prominent at 1000 nm than 2300 nm (this can be seen for acetylene by comparing Figs. 32 and 33), and it is more prominent for acetylene than propylene (cf. Figs. 32 and 34). The spike cannot be due to conventional radiation intermittency that has been seen near the edge of nonluminous flames (Kounalakis et al., 1988, 1989), which is due to the presence of only ambient air in the radiation path as an effect of intermittency, since the present radiation paths always passed through the flame sheets. Rather, an explanation that fits most of the observations is that the low radiation levels are due to blockage from puffs of overfire soot passing between the luminous region of the flame and the monochromator. First of all, the region containing overfire soot increases in length with increasing height above the burner, which should increase the probability of overfire soot being in the radiation path, as observed. Secondly, extinction by cool soot should increase with decreasing wavelength while radiant emission is higher at a wavelength of 2300 nm than 1000 nm, which explains the more prominent spike at 1000 nm. Finally, acetylene has higher soot volume fractions in the overfire region, in comparison to soot volume fractions in the underfire soot spike, than propylene: this also helps to explain the larger radiation spike for acetylene. Thus the radiation spike seen in Figs. 32-34 is simply a manifestation of the familiar soot blockage effect of flame radiation which explains why a similar spike is not seen in nonluminous flames (Kounalakis et al., 1988, 1989). The effect is clearly quite wavelength-selective which presents significant difficulties for the use of gray soot particle approximations for luminous flames.

Another feature of the results of Figs. 32-34 is that the PDF's are always skewed with most probable values generally below mean values. This behavior is also similar to effects of radiation intermittency seen in nonluminous flames (Kounalakis et al., 1988,

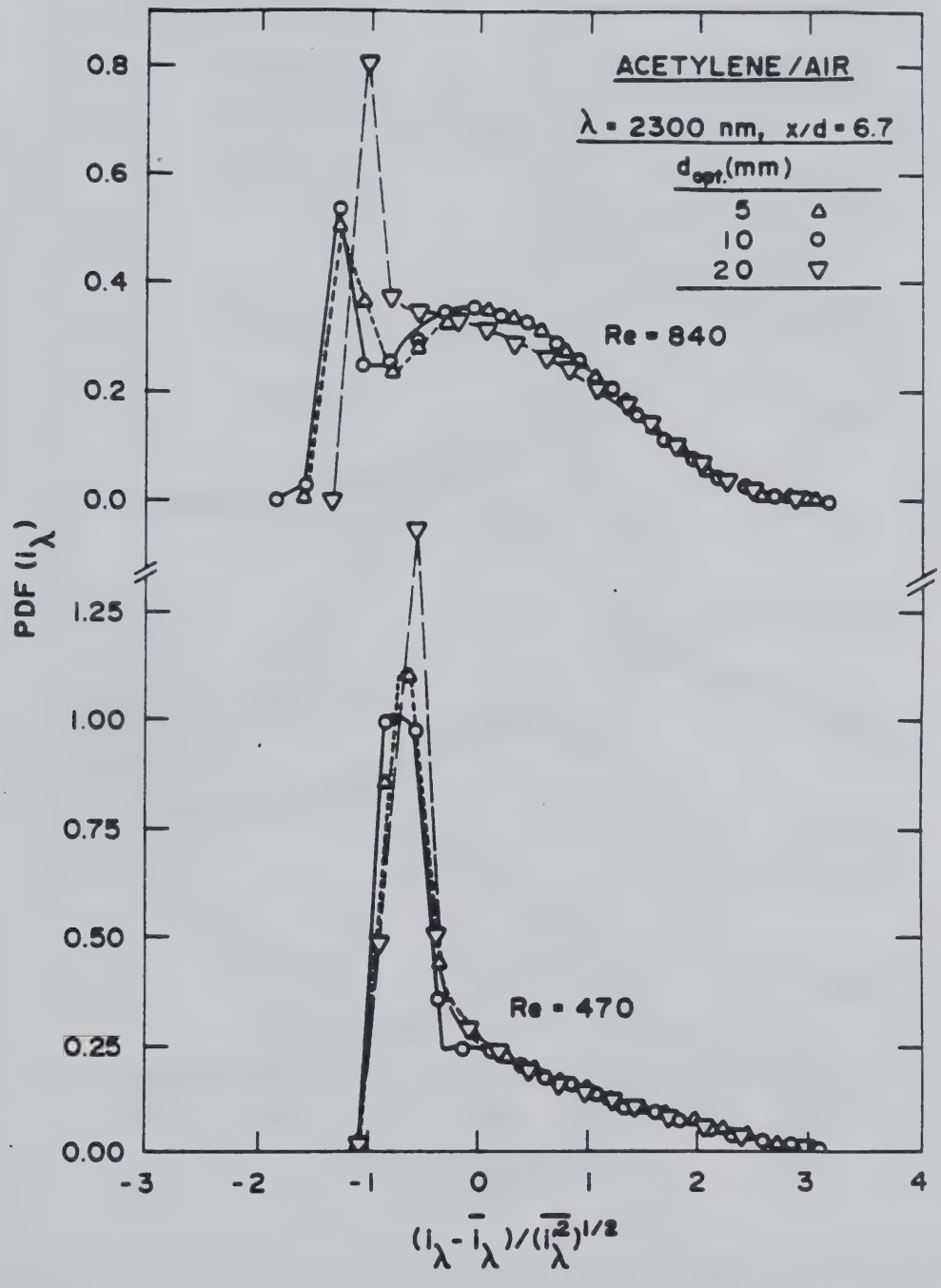

Figure 32 Effect of optical path diameter on PDF's of spectral radiation intensities for turbulent acetylene/air flames.

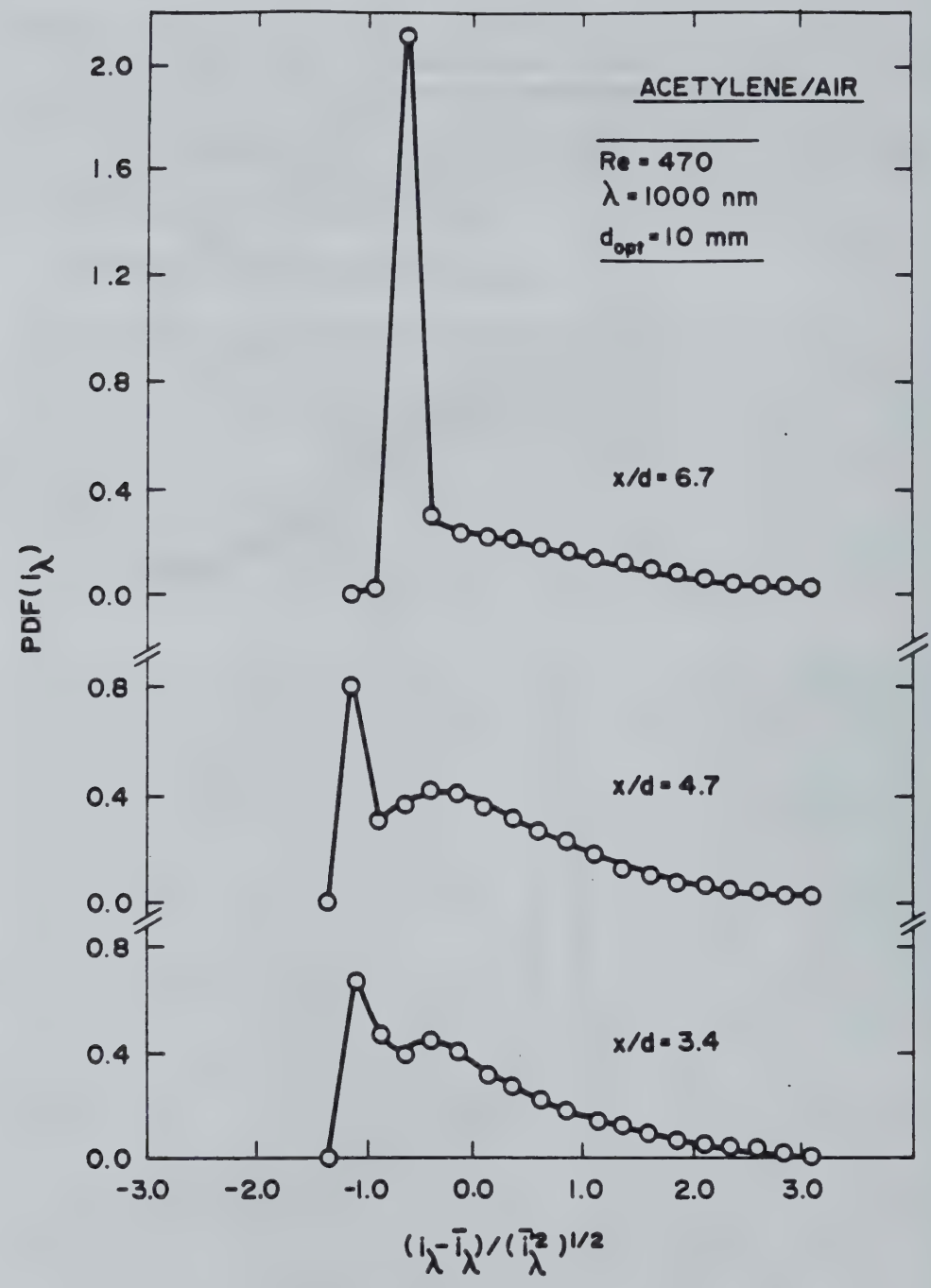

Figure 33 PDF's of spectral radiation intensities at 1000 nm for a turbulent acetylene/air diffusion flame: Re = 470.

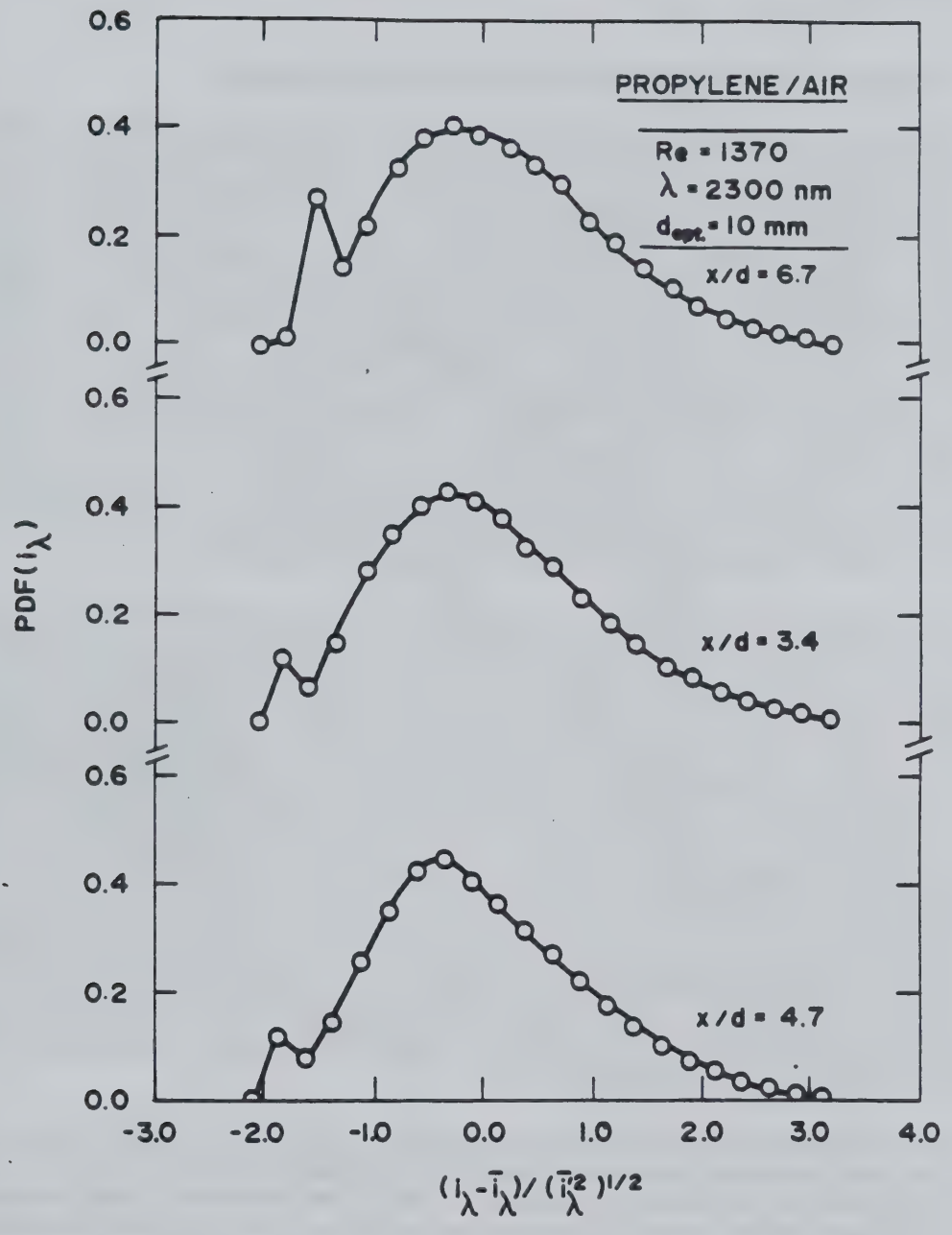

Figure 34 PDF's of spectral radiation intensities at 2300 nm for a turbulent propylene/air diffusion flame: Re = 1370.

1989). Basically, it comes about since the spectral radiation intensity can never be lower than zero and this finite limit forces the PDF to be skewed. Proper representation of these features using the stochastic time-series method should provide a good test of the theory: this will be undertaken during the next phase of the work after soot volume fraction statistics are known.

5.3.3 Power Spectral Densities of Spectral Radiation Intensities

The effect of optical path diameter on the power spectral densities of spectral radiation intensities can be seen from the results plotted in Fig. 35. This plot involves power spectral densities of spectral radiation intensities at a wavelength of 2300 nm for optical path diameters of 5, 10 and 20 mm. The results were obtained for the two acetylene/air flames at x/d = 6.7; however, findings for other conditions were similar. Results at low frequencies (< 50 Hz) are independent of optical path diameter within experimental uncertainties. However, for frequencies greater than 50 Hz, results for the larger path diameters decay more rapidly as the frequency increases. This is a direct effect of spatial averaging over a larger path diameter where the small scale features, and their associated radiation fluctuations, are filtered out. Fortunately, this region does not contain much signal energy so that its effect on moments, PDF's and spectral response at low frequencies is small. In order to maintain good signal-to-noise ratios for the remaining conditions, measurements were made with an optical path diameter of 10 mm. However, it should be recognized that this reduces the spectral intensities by about a factor of 2 from a 5 mm diameter path at the highest frequencies that are plotted.

Some representative power spectral densities of spectral radiation intensities for other positions in both acetylene and propylene flames are illustrated in Figs. 36 and 37. All the results, including those shown in Fig. 35, exhibit a bulge or spike at low frequencies. This behavior is very similar to past observations for low Reynolds number nonluminous flames (Kounalakis et al., 1988, 1989). Thus, it is likely that this spike is caused by pulsations of the entire flame structure which is a typical feature of highly-buoyant pool-like flames. For acetylene (Fig. 36), the spiked structure is quite rich, with harmonics appearing near the burner exit. However, the spikes become much less prominent with increasing height above the burner exit which is similar to observations in nonluminous flames (Kounalakis et al., 1988, 1989). This behavior follows from increasing randomness of the flow as the Reynolds number increases with increasing height above the burner. In contrast, the magnitude of the low-frequency spike actually increases with increasing height above the burner for the propylene/air flames (Fig. 37). This behavior could be due to the greater length of these flames, where the region considered for propylene in Fig. 37 represents a smaller fraction of the flame height than the region considered for acetylene in Fig. 36.

The break frequencies, where the spectra begin to decay with increasing frequency, are relatively independent of streamwise position for the results illustrated in Figs. 36 and 37. This behavior is probably characteristic of the lower portions of highly-buoyant flames, where streamwise velocities are relatively constant along the axis (McCaffrey, 1979) while the reaction zone is relatively near the edge of the flow. Additional assessment of these properties must await measurements of soot-volume-fraction statistics along the radiation path.

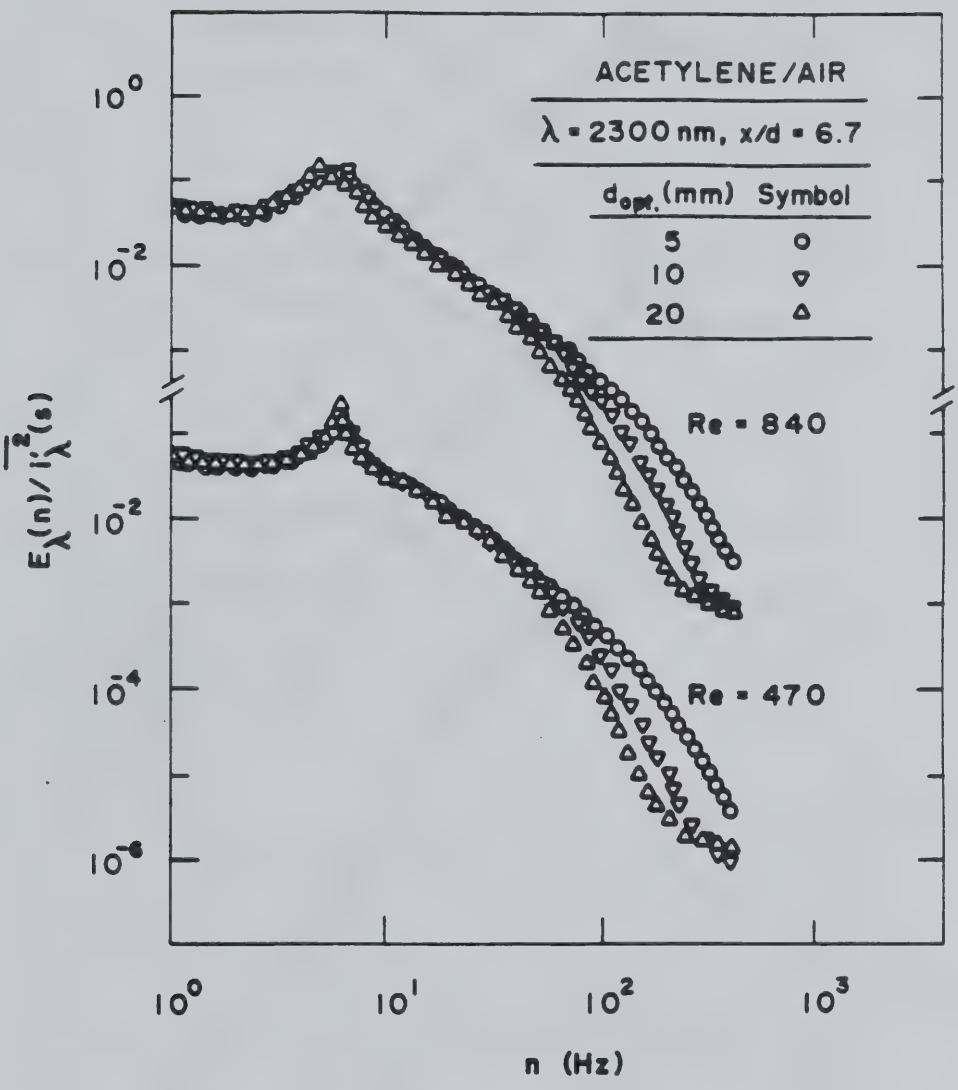

Figure 35 Effect of optical path diameter on power spectral densities of spectral radiation intensities for turbulent acetylene/air diffusion flames.

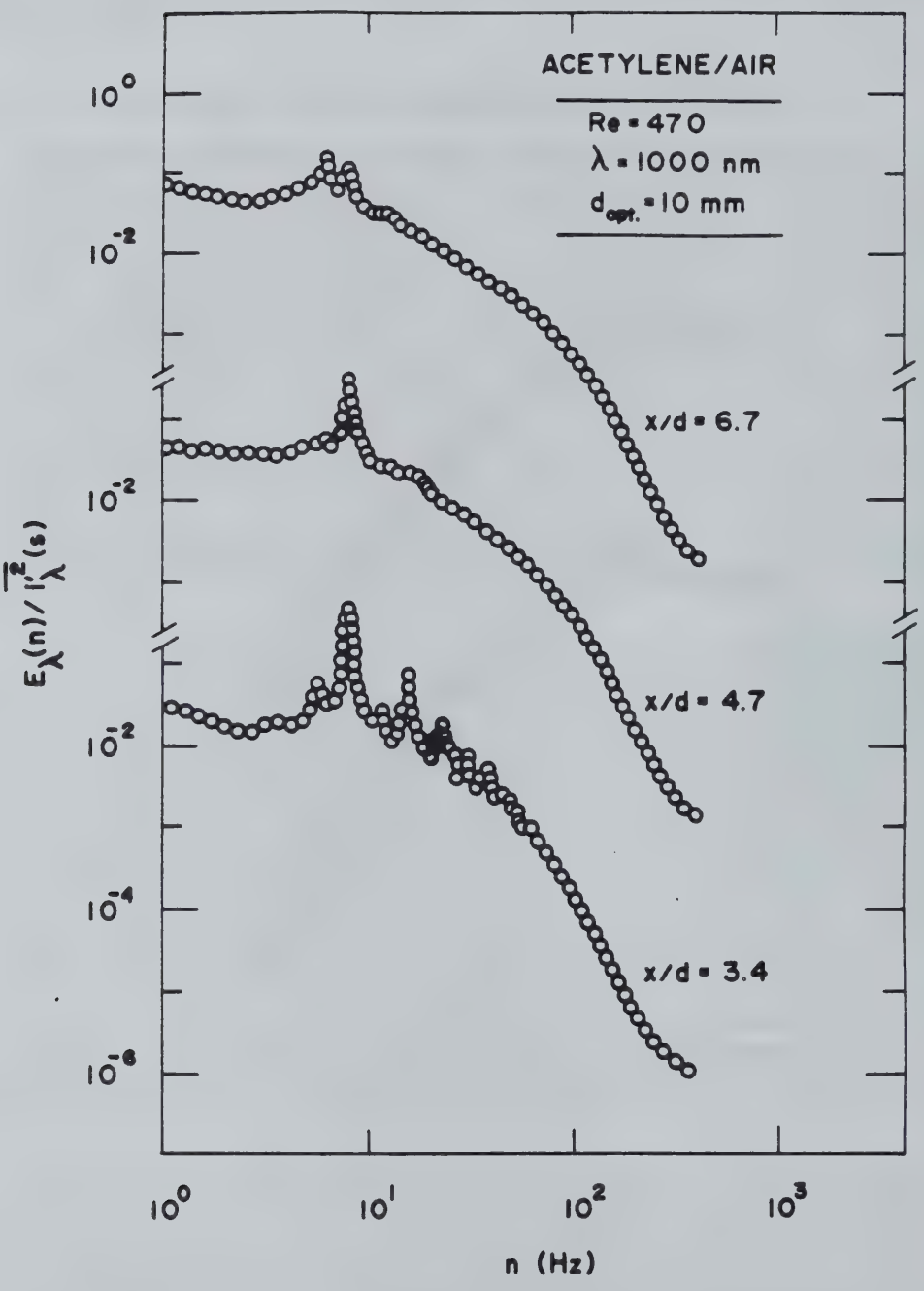

Figure 36 Power spectral densities of spectral radiation intensities at 1000 nm for a turbulent acetylene/air diffusion flame: Re = 470.

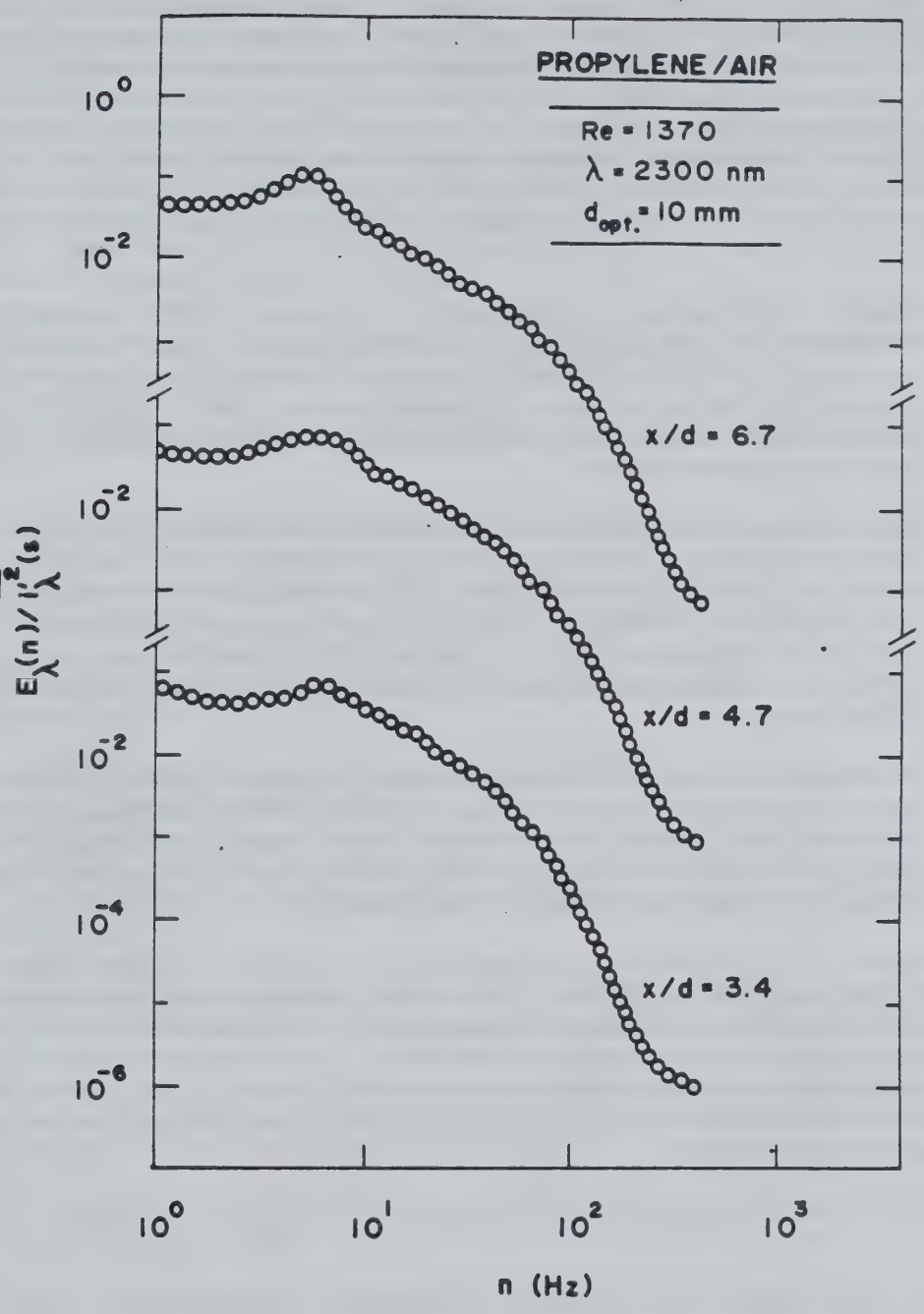

Figure 37 Power spectral densities of spectral radiation intensities at 2300 nm for a turbulent propylene/air diffusion flame: Re = 1370..

5.4 Conclusions

Mean and fluctuating values, probability density functions and temporal power spectral densities of spectral radiation intensities were measured for horizontal radial paths through the axis of luminous turbulent diffusion flames. Wavelengths were 1000 and 2300 nm, which are in the continuum portion of the spectrum due to radiation from soot. The region of the measurements was below the flame tip of highly-buoyant pool-like acetylene and propylene diffusion flames burning in still air. Flame residence times were long so that operation was in the plateau region where soot generation efficiencies are relatively independent of burner operating conditions. The main conclusions of the study are as follows:

1. Radiation fluctuation intensities were in the range 54-145%, tending to increase with increasing height above the burner: these values are considerably higher than values observed in the flaming region of nonluminous diffusion flames (Kounalakis et al., 1988, 1989). This clearly indicates that turbulence/radiation interactions are important for luminous turbulent flames.

2. PDF's of spectral radiation intensities exhibited a radiation spike at low spectral radiation intensities that was not observed for PDF's of spectral radiation intensities from nonluminous flames. Evidence concerning the effect of position, wavelength and fuel type on the properties of the spikes support the hypothesis that it is due to puffs of overfire soot passing through the radiation path and blocking radiation from the luminous portion of the flame.

3. Power spectral densities of spectral radiation intensities exhibited spikes at low frequencies which were similar to spikes observed in the temporal spectra of low Reynolds number nonluminous flames (Kounalakis et al., 1988, 1989). These spikes are probably due to the pulsations of the flame that are typically observed for pool-like flames.

Work on this phase of the investigation is still in progress. Current efforts involve measuring the statistical properties of soot volume fractions along the radiation paths: moments, PDF's, spatial correlations, and temporal correlations and spectra as well as conditional properties of overfire and underfire soot. This information will be combined with the temperature/soot-volume-fraction correlations discussed in Section 3 of this report to predict the spectral radiation properties of the flames for comparison with the measurements reported here.

REFERENCES

Abdel-Khalik, S.I., Tamaru, T. and El-Wakil, M.M. (1974) A chromatographic and interferometric study of the diffusion flame around a simulated drop. Fifteenth Symposium (International) on Combustion, The Combustion Institute, Pittsburgh, 389-399.

Batten, C.E. (1985) Spectral optical constants of soots from polarized angular reflectance measurements. Applied Optics 24, 1193-1199.

Becker, H.A. and Liang, D. (1978) Visible length of vertical free turbulent diffusion flames. Combust. Flame 32, 115-137.

Becker, H.A., Hottel, H.C. and Williams, G.C. (1967) The nozzle-fluid concentration field of the round, turbulent, free jet. J. Fluid Mech. 30, 285-303.

Bilger, R.W. (1976) Turbulent jet diffusion flames. Prog. Energy Combust. Sci. 1, 87-109.

Bilger, R.W. (1977) Reaction rates in diffusion flames. Combust. Flame 30, 277-284.

Birch, A.D., Brown, D.R., Dodson, M.G. and Thomas, J.R. (1978) The turbulent concentration field of a methane jet. J. Fluid Mech. 88, 431-449.

Box, G.E.P. and Jenkins, G.M. (1976) Time Series Analysis, Holden-Day, San Francisco, 51-66.

Cashdollar, K.L. (1979) Three-wavelength pyrometer for measuring flame temperatures. Applied Optics 18, 2595-2597.

Charalampopoulos, T.T. and Chang, H. (1988) In situ optical properties of soot particles in the wavelength range from 340 nm to 600 nm. Combust. Sci. Tech. 59, 401-421.

Charalampopoulos, T.T. and Felske, J.D. (1987) Refractive indices of soot particles deduced from in-situ laser light scattering measurements. Combust. Flame 68, 283-294.

Chuech, S.G., Lai, M.-C. and Faeth, G.M. (1989) Structure of turbulent sonic underexpanded free jets. AIAA J. 27, 549-559.

Corrsin, S. and Uberoi, M.S. (1951) Spectra and diffusion in a round turbulent jet. NACA Report No. 1040.

Cox, G. (1977) On radiant heat transfer from turbulent flames. Combust. Sci. Tech. 17, 75-78.

Dalzell, W.H. and Sarofim, A.F. (1969) Optical constants of soot and their application to heat-flux calculations. J. Heat Trans. 91, 100-104.

deRis, J. (1978) Fire radiation - a review. Seventeenth Symposium (International) on Combustion, The Combustion Institute, Pittsburgh, 1003-1016.

Faeth, G.M. (1988) Heat transfer in fires and combustion systems. ASME Proceedings of the 1988 National Heat Transfer Conference (H.R. Jacobs, ed.), HTD-Vol. 96, Vol. 1, 1-25.

Faeth, G.M. and Samuelson, G.S. (1986) Fast-reaction nonpremixed combustion. Prog. Energy Combust. Sci. 12, 305-372.

Faeth, G.M., Gore, J.P., Chuech, S.G. and Jeng, S.-M. (1988a) Radiation from turbulent diffusion flames. Annual Review of Numerical Fluid Mechanics and Heat Transfer, Vol. 2, Hemisphere Publishing Corp., Washington, 1-38.

Faeth, G.M., Gore, J.P., Sivathanu, Y.R. (1988b) Radiation from soot-containing flames. Combustion and Fuels in Gas Turbine Engines, AGARD Conference Proceedings No. 422, NATO, Paris, 17-1 — 17-12.

Fischer, S.J., Hardouin-DuParc, B. and Grosshandler, W.L. (1987) The structure and radiation of an ethanol pool fire. Combust. Flame 70, 291-306.

Flower, W.L. (1988) An investigation of soot formation in axisymmetric turbulent diffusion flames at elevated pressure. Twenty-Second Symposium (International) on Combustion, The Combustion Institute, Pittsburgh, 425-435.

Flower, W.L. and Bowman, C.T. (1986) Soot production in axisymmetric laminar diffusion flames at pressures from one to ten atmospheres. Twenty-First Symposium (International) on Combustion, The Combustion Institute, Pittsburgh, 1115-1124.

Glass, M. and Kennedy, I.M. (1977) An improved seeding method for high temperature laser Doppler velocimetry. Combust. Flame 29, 333-335.

Gordon, S. and McBride, B.J. (1971) Computer program for calculation of complex chemical equilibrium compositions, rocket performance, incident and reflected shocks, and Chapman-Jouguet detonations. NASA SP-273.

Gore, J.P. (1986) A theoretical and experimental study of turbulent flame radiation. Ph.D. Thesis, The Pennsylvania State University, University Park, PA.

Gore, J.P. and Faeth, G.M. (1986) Structure and spectral radiation properties of turbulent ethylene/air diffusion flames. Twenty-First Symposium (International) on Combustion, The Combustion Institute, Pittsburgh, 1521-1531.

Gore, J.P. and Faeth, G.M. (1987) Structure and radiation properties of luminous turbulent acetylene/air diffusion flames. J. Heat Trans. 110, 173-181.

Gore, J.P. and Faeth, G.M., Evans, D. and Pfenning, D. (1987a) Structure and radiation properties of large-scale natural gas/air diffusion flames. Fire and Materials, 10, 161-169.

Gore, J.P., Jeng, S.-M. and Faeth, G.M. (1987b) Spectral and total radiation properties of turbulent carbon monoxide/air diffusion flames. AIAA J. 25, 339-345.

Gore, J.P., Jeng, S.-M. and Faeth, G.M. (1987c) Spectral and total radiation properties of turbulent hydrogen/air diffusion flames. J. Heat Trans. 109, 165-171.

Grosshandler, W.L. (1980) Radiative heat transfer in nonhomogeneous gases: a simplified approach. Int. J. Heat Mass Transfer 23, 1447-1457.

Grosshandler, W.L. and Vantelon, J.P. (1985) Predicting soot radiation in laminar diffusion flames. Combust. Sci. Tech. 44, 125-141.

Habib, Z.G. and Vervisch, P. (1988) On the refractive index of soot at flame temperature. Combust. Sci. Tech. 59, 261-274.

Incropera, F. and DeWitt, D.P. (1981) Fundamentals of Heat Transfer, John Wiley & Sons, New York, 558-561.

Jeng, S.-M. and Faeth, G.M. (1984a) Species concentrations and turbulence properties in buoyant methane diffusion flames. J. Heat Trans., 106, 721-727.

Jeng, S.-M. and Faeth, G.M. (1984b) Predictions of mean scalar properties in turbulent propane diffusion flames. J. Heat Trans. 106, 891-893.

Jeng, S.-M. and Faeth, G.M. (1984c) Radiative heat fluxes near turbulent buoyant methane diffusion flames. J. Heat Trans. 106, 886-888.

Jeng, S.M., Chen, L.-D. and Faeth, G.M. (1982) The structure of buoyant methane and propane diffusion flames. Nineteenth Symposium (International) on Combustion, The Combustion Institute, Pittsburgh, 949-958.

Jeng, S.-M., Lai, M.-C. and Faeth, G.M. (1984) Nonluminous radiation in turbulent buoyant axisymmetric flames. Combust. Sci. Tech. 40, 41-52.

Kabashnikov, V.P. and Kmit, G.I. (1979) Influence of turbulent fluctuations on thermal radiation. J. Appl. Spect. 31, 963-967.

Kent, J.H. (1987) Turbulent diffusion flames sooting-relationship to smoke-point tests. Combust. Flame 67, 223-233.

Kent, J.H. and Bastin, S.J. (1984) Parametric effects on sooting in turbulent acetylene diffusion flames. Combust. Flame 56, 29-42.

Kent, J.H. and Honnery, D. (1987) Soot and mixture fraction in turbulent diffusion flames. Combust. Flame 54, 383-397.

Klingenberg, G. (1985) Invasive spectroscopic technique for measuring temperature in highly pressurized combustion chambers. Optical Engineering 24, 692-696.

Kounalakis, M.E., Gore, J.P. and Faeth, G.M. (1988) Turbulence/radiation interactions in nonpremixed hydrogen/air flames. Twenty-Second Symposium (International) on Combustion, The Combustion Institute, Pittsburgh, 1281-1290.

Kounalakis, M.E., Gore, J.P. and Faeth, G.M. (1989) Mean and fluctuating radiation properties of nonpremixed turbulent carbon monoxide flames. J. Heat Trans., in press.

Lai, M.-C. and Faeth, G.M. (1987) Turbulence structure of vertical adiabatic wall plumes. J. Heat Trans. 109, 663-670.

Liew, S.K., Bray, K.N.C. and Moss, J.B. (1981) A flamelet model of turbulent non-premixed combustion. Combust. Sci. Tech. 27, 69-73.

Liew, S.K., Bray, K.N.C. and Moss, J.B. (1984) A stretched laminar flamelet model of turbulent nonpremixed combustion. Combust. Flame 56, 199-214.

List, E.J. (1984) Turbulent jets and plumes. Ann. Rev. Fluid Mech. 14, 189-212.

Lockwood, F.C. and Naguib, A.S. (1975) The prediction of the fluctuations in the properties of free, round-jet, turbulent diffusion flames. Combust. Flame 24, 109-124.

Ludwig, C.B., Malkmus, W., Reardon, J.E. and Thomson, J.A. (1973) Handbook of Infrared Radiation from Combustion Gases, NASA SP-3080.

Markstein, G.H. (1981) Scanning radiometer measurements of the radiance distribution in PMMA pool fires. Eighteenth Symposium (International) on Combustion, The Combustion Institute, Pittsburgh, 537-547.

McCaffrey, B.J. (1979) Purely buoyant diffusion flames: some experimental results. NBSIR79-1910, National Bureau of Standards, Washington, DC.

Megaridis, C.M. and Dobbins, R.A. (1988) Soot aerosol dynamics in a laminar ethylene diffusion flame. Twenty-Second Symposium (International) on Combustion, The Combustion Institute, Pittsburgh, 353-362.

Mitchell, R.E., Sarofim, A.F. and Clomberg, L.A. (1980a) Partial equilibrium in the reaction zone of methane-air diffusion flames. Combust. Flame 37, 201-206.

Mitchell, R.E., Sarofin, A.F. and Clomberg, L.A. (1980b) Experimental and numerical investigation of confined laminar diffusion flames. Combust. Flame 37, 227-244.

Moore, J.G. and Moore, J. (1976) The distribution of temperature and major species in laminar diffusion flames. Sixteenth Symposium (International) on Combustion, The Combustion Institute, Pittsburgh, 1123-1132.

Newman, J.S. and Steciak, J. (1987) Characterization of particulates from diffusion flames. Combust. Flame 67, 55-64.

Pitts, W.M. and Kashiwagi, T. (1984) The application of laser-induced Rayleigh light scattering to the study of turbulent mixing. J. Fluid Mech. 141, 391-429.

Portscht, R. (1974) Studies on characteristic fluctuations of flame radiation emitted by fires. Combust. Sci. Tech. 10, 73-84.

Saito, K., Williams, F.A. and Gordon, A.S. (1986) Structure of laminar coflow methane-air diffusion flames. J. Heat Trans. 108, 640-648.

Santoro, R.J., Semerjian, H.B. and Dobbins, R.A. (1983) Soot particle measurements in diffusion flames. Combust. Flame 51, 203-218.

Santoro, R.J., Dobbins, R.A. and Semerjian, H.G. (1984) Interpretation of optical measurements of soot in flames. Prog. Astro. and Aero. 92, 343-382.

Schug, K.P., Manheimer-Timnat, Y., Yaccarino, P. and Glassman, I. (1980) Sooting behavior of gaseous hydrocarbon diffusion flames and the influence of additives. Combust. Sci. Tech. 22, 235-250.

Shaughnessy, E.J. (1975) "Measurements of particle diffusion in the turbulent jet by laser light scattering," Ph.D. Thesis, University of Virginia.

Sivathanu, Y.R. and Faeth, G.M. (1989a) Soot volume fractions in the overfire region of turbulent diffusion flames. Combust. Flame, in press.

Sivathanu, Y.R. and Faeth, G.M. (1989b) Temperature/soot volume fraction correlations in the fuel rich region of buoyant turbulent diffusion flames. Combust. Flame, in press.

Sivathanu, Y.R. and Faeth, G.M. (1989c) State relationships for major gas species in nonpremixed hydrocarbon/air flames. Combust. Flame, submitted.

Sivathanu, Y.R., Kounalakis, M.E., Gore, J.P. and Faeth, G.M. (1987) Radiation from turbulent nonluminous and luminous diffusion flames. Annual Report for NBS Grant No. 60NANB5D0576, Department of Aerospace Engineering, The University of Michigan, Ann Arbor, MI.

Sivathanu, Y.R., Gore, J.P. and Faeth, G.M. (1988) Scalar properties in the overfire region of sooting turbulent diffusion flames. Combust. Flame 73, 315-329.

Smyth, K.C., Miller, J.H., Dorfman, R.C., Mallard, W.G. and Santoro, R.J. (1985) Soot inception in a methane/air diffusion flame as characterized by detailed species profiles. Combust. Flame 62, 157-181.

Stårner, S.H. and Bilger, R.W. (1980) Measurements of scalar-velocity correlations in a turbulent diffusion flame. Eighteenth Symposium (International) on Combustion, The Combustion Institute, Pittsburgh, 921-930.

Tien, C.L. and Lee, S.C. (1982) Flame radiation. Prog. Energy Combust. Sci. 8, 41-59.

Tsuji, H. and Yamaoka, I. (1968) The structure of counterflow diffusion flames in the forward stagnation region of a porous cylinder. Twelfth Symposium (International) on Combustion, The Combustion Institute, Pittsburgh, 997-1005.

Tsuji, H. and Yamaoka, I. (1970) Structure analysis of counterflow diffusion flames in the forward stagnation region of a porous cylinder. Thirteenth Symposium (International) on Combustion, The Combustion Institute, Pittsburgh, 723-731.

NIST-114A
(REV. 3-89)

U.S. DEPARTMENT OF COMMERCE
NATIONAL INSTITUTE OF STANDARDS AND TECHNOLOGY

BIBLIOGRAPHIC DATA SHEET

1. PUBLICATION OR REPORT NUMBER
NIST-GCR-90/570

2. PERFORMING ORGANIZATION REPORT NUMBER

3. PUBLICATION DATE
February 1990

4. TITLE AND SUBTITLE

Structure and Radiation Properties of Turbulent Diffusion Flames

5. AUTHOR(S)

Y.R. Sivathanu, M.E. Kounalakis and G.M. Faeth

6. PERFORMING ORGANIZATION (IF JOINT OR OTHER THAN NIST, SEE INSTRUCTIONS)

The University of Michigan
Department of Aerospace Engineering
Ann Arbor, MI

7. CONTRACT/GRANT NUMBER
60NANB8D0833

8. TYPE OF REPORT AND PERIOD COVERED
Annual Report

9. SPONSORING ORGANIZATION NAME AND COMPLETE ADDRESS (STREET, CITY, STATE, ZIP)

U.S. Department of Commerce
National Institute of Standards and Technology
Gaithersburg, MD 20899

10. SUPPLEMENTARY NOTES

[ ] DOCUMENT DESCRIBES A COMPUTER PROGRAM; SF-185, FIPS SOFTWARE SUMMARY, IS ATTACHED.

11. ABSTRACT (A 200-WORD OR LESS FACTUAL SUMMARY OF MOST SIGNIFICANT INFORMATION. IF DOCUMENT INCLUDES A SIGNIFICANT BIBLIOGRAPHY OR LITERATURE SURVEY, MENTION IT HERE.)

A theoretical and experimental study of the structure and radiation properties of turbulent diffusion flames is described. Generalized state-relationship correlations, giving the mass fractions of major gas species (N_2, O_2, fuel, CO_2, H_2O, CO and H_2) as functions of local fuel-equivalence ratios, were developed for hydrocarbon/air diffusion flames. Instantaneous soot volume fractions and temperatures were measured in the fuel-rich (underfire) region of turbulent nonpremixed acetylene, propylene, ethylene and propane flames burning in still air. Mixture fraction properties in turbulent carbon monoxide/air diffusion flames were measured in order to provide information needed to exploit the laminar flamelet concept for radiation predictions. A two-point Mie scattering system was developed to yield Favre-and time-averaged mean and fluctuating values, probability density functions, temporal spectra and correlations, and spatial correlations of mixture fractions. The continuum radiation properties of the underfire region of luminous acetylene and propylene flames burning in still air were studied. Instantaneous radiation intensities at 1000 and 2300 nm, where gas-band radiation is absent, were measured for paths passing through the axis of the flames; and reduced to yield mean and fluctuating values, probability density functions and power spectral densities of spectral radiation intensities.

12. KEY WORDS (6 TO 12 ENTRIES; ALPHABETICAL ORDER; CAPITALIZE ONLY PROPER NAMES; AND SEPARATE KEY WORDS BY SEMICOLONS)

correlation , flames, mixtures, radiation, soot, turbulence

13. AVAILABILITY

[X] UNLIMITED

[ ] FOR OFFICIAL DISTRIBUTION. DO NOT RELEASE TO NATIONAL TECHNICAL INFORMATION SERVICE (NTIS).

[ ] ORDER FROM SUPERINTENDENT OF DOCUMENTS, U.S. GOVERNMENT PRINTING OFFICE, WASHINGTON, DC 20402.

[X] ORDER FROM NATIONAL TECHNICAL INFORMATION SERVICE (NTIS), SPRINGFIELD, VA 22161.

14. NUMBER OF PRINTED PAGES
104

15. PRICE
A06

ELECTRONIC FORM